3D NUMERICAL SIMULATION OF TURBULENT OPEN-CHANNEL FLOW THROUGH VEGETATION

A Thesis
Presented to
The Academic Faculty

by

Su Jin Kim

In Partial Fulfillment
of the Requirements for the Degree
Doctor of Philosophy in the
School of Civil and Environmental Engineering

Georgia Institute of Technology
December 2011

3D NUMERICAL SIMULATION OF TURBULENT OPEN-CHANNEL FLOW THROUGH VEGETATION

Approved by:

Dr. Thorsten Stoesser, Advisor
School of Civil and Environmental Engineering
Georgia Institute of Technology

Dr. Donald R. Webster
School of Civil and Environmental Engineering
Georgia Institute of Technology

Dr. Terry W. Sturm
School of Civil and Environmental Engineering
Georgia Institute of Technology

Dr. Minami Yoda
George W. Woodruff School of Mechanical Engineering
Georgia Institute of Technology

Dr. Philip J. Roberts
School of Civil and Environmental Engineering
Georgia Institute of Technology

Date Approved: 4 November 2011

To my beloved family, Kyuman Kim, Oknam Hwang, Suyun Kim, and Jinhwan Kim

ACKNOWLEDGEMENTS

I would like to show my gratitude to my advisor, Dr. Thorsten Stoesser who was abundantly helpful and offered invaluable support, encouragement and friendship throughout my study at Georgia Tech. Deepest gratitude are also due to my committee members, Professor Terry W. Sturm, Professor Philip J. Roberts, Professor Donald R. Webster, and Professor Minami Yoda; without whose patience, knowledge, and assistance, this study would not have been successful. My appreciation is also given to Sina Wunder for the cowork of the part of my research.

I would like to thank my current and previous lab mates, Dongjin, Svetlana, Todor, Sandeep, Sibel, Mustafa, Zhuo, Mehtap, and Zing for their great help and friendship. I owe my sincere gratitude to my friends at Georgia Tech, especially to Seungho, Eunhyea, Eunjeong, Boyeon, and Haeyeon. I also wish to express my gratitude to my former advisor in Hanyang University, Dr. Yong-Sik Cho and senior researcher at KICT, Dr. Kwang-Seok Yoon for their great advices and support.

I would like to give my deepest appreciation to my parents, sister, and brother for their unconditional love and endless support which enabled me to complete my Ph.D. work successfully.

TABLE OF CONTENTS

LIST OF TABLES

LIST OF FIGURES

LIST OF SYMBOLS OR ABBREVIATIONS

A	area occupied by the plant.
A_P	projected area of plants.
B	channel width.
C_D, c_D	drag coefficient.
CFD	Computational Fluid Dynamics.
CFL	Courant Friedrichs Lewy.
C_p	time-averaged pressure coefficient.
C_s	Smagorinsky constant.
D	cylinder diameter.
Δ	anisotropic characteristic filter size.
Δx	characteristic filter width in x direction.
Δy	characteristic filter width in y direction.
Δz	characteristic filter width in z direction.
δ_{ij}	Kroneker delta.
DNS	Direct Numerical Simulation.
dp/dx	pressure gradient.
f	frequency.
F_D	drag force.
f_D	drag force per unit mass exerted by vegetation.
$F_{D,total}$	total forces exerted on the vegetation.
F_g	total shear stress exerted on the flow region.
f_i	external forces per unit mass.
Fr	Froude number.
g	acceleration due to gravity, 9.81 m/s^2.
h	plant height.

H, h	water depth.
I	hydraulic gradient.
${\tau_{ij}}^a$	anisotropic stress tensor.
k	turbulent kinetic energy.
κ	von Karman's constant (=0.4187).
k_r	residual kinetic energy.
k_s	roughness variable.
k_{st}	Stricklers number.
LAI	Leaf Area Index.
LAI_M	mean leaf area of the plant.
$\langle p \rangle$	time-averaged pressure.
LDA	Laser Doppler Anemometry.
LES	Large Eddy Simulations.
M	Manning-Strickler number.
M	total number of individual vegetation in flow region.
m	number of cylinders per unit horizontal area.
m	number of individual stem in each cell.
N	the number of leaves.
n	porosity.
n_f	effective porosity of the plants.
ν	kinematic viscosity of the working fluid.
ν_t	subgrid scale eddy viscosity.
p	filtered pressure.
p'	pressure perturbation.
PDF	Probability Density Functions.
PDS	Power Density Spectra.
π	mathematical constant approximately equal to 3.14159.

ψ	width fraction factor.
Q	discharge through the channel.
R^2	squared correlation coefficient in regression analysis.
RANS	Reynolds Averaged Navier Stokes.
Re	Reynolds number based on the water depth.
Re_D	Reynolds number based on the cylinder diameter.
ρ	working fluid density.
RMS	Root Mean Square.
$\|S\|$	characteristic filtered strain rate.
s	distance between two cylinders in a same direction.
S_0	bottom slope of channel.
SGS	Sub Grid Scale.
S_{ij}	filtered strain-rate tensor.
S_t	Strouhal number.
t	time.
τ_0	global shear stress.
τ_b	bed shear stress.
τ_{ij}	stress tensor.
τ_w	wall shear stress.
t_e	eddy turn-over time.
U	time-averaged flow velocity.
U_∞	free stream velocity.
U_*	shear velocity.
u	instantaneous velocity component in x direction.
u'	velocity fluctuation.
u_0	free stream velocity.
u_{bulk}	fluid velocity in the direction of the mean flow.

u_{cell}	calculated velocity by fluid volume fraction.
u_i	initial velocity of each cell.
u_i, u_j	instantaneous velocity vector.
URANS	Unsteady Reynolds Averaged Navier Stokes.
v	instantaneous velocity component in y direction.
φ, ϕ	vegetation density; cylinder volume fraction.
V_f	fluid volume fraction.
Vol	total volume of a fluid domain.
w	instantaneous velocity component in z direction.
x	spatial position in x direction.
x_i	spatial position vector.
y	spatial position in y direction.
y^+	boundary condition evaluation factor.
z	spatial postion in z direction.

SUMMARY

A comprehensive understanding of the hydrodynamics in vegetated open-channels and flow-vegetation interaction is of high interest to researchers and practitioners alike for instance in the content of river and coastal restoration schemes. The focus of this study was to investigate the effect of the presence of vegetation on flow resistance, turbulence statistics, and the instantaneous flow in open channels by performing three-dimensional computational-fluid-dynamics (CFD) simulations.

Firstly, fully developed turbulent flow in fully-vegetated channel was analyzed by employing the method of high-resolution Large-Eddy Simulation (LES). Flow through a staggered array of rigid, emergent cylinders was simulated and the LES was validated through experiments. After validation, numerical simulations were performed at an extended parameter range of two different cylinder Reynolds numbers (Re_D = 500 and 1340) and three different vegetation densities (ϕ = 0.016, 0.063, and 0.251). Flow structures and statistics were analyzed on the instantaneous flow and the effect of the vegetation density and cylinder Reynolds number was assessed. Moreover, drag forces exerted on the cylinders were calculated explicitly, and the effect of both Re_D and ϕ on the drag coefficient was quantified.

Secondly, two new alternative simulation strategies, a RANS based strategy with a vegetative closure model and a low-resolution Large-Eddy Simulation, were devised. They were evaluated by simulating several experimental cases with diverse conditions of the cylinder arrangement (i.e., staggered vs. random distribution), vegetation densities (ϕ = 0.016, 0.022, 0.063, 0.087, 0.091, 0.150, and 0.251), and cylinder Reynolds number ($Re_D = 170-1700$). For the RANS based strategy, the importance of *a-priori* knowledge was assessed, and for the low-resolution LES, the efficiency and accuracy

was demonstrated.

Finally, a numerical strategy based on a porosity approach was developed and applied to open-channel flow through a natural plant. The simulated velocities were compared with experimentally acquired ones and results showed reasonable agreement.

The results obtained in this research contribute to the understanding of fundamental mechanism of flow-vegetation interaction in vegetated open-channels, resolving turbulent flow-vegetation interaction explicitly. In addition, the new numerical strategies developed as part of this research are expected to allow describing the behavior of turbulent flow through artificial and natural vegetation with high efficiency and accuracy.

CHAPTER I

INTRODUCTION

1.1 Background and Motivation

1.1.1 Effect of Vegetation in Open-Channel Flow

Aquatic and riparian vegetation in open-channel flow interrupts the flow through additional drag, and it causes a noticeable alteration of the turbulent flow compared to that in non-vegetated zones. The main influences of vegetation in open-channel flow are (1) horizontal and vertical distributions of mean and instantaneous velocity, (2) turbulence quantities and Reynolds stresses, and (3) transport of sediments and solutes. Moreover, the flow through a vegetated channel, especially in a compound channel, has significant velocity gradients and strong secondary currents (laterally, longitudinally and vertically) resulting in shear layer formation between the canopy flow and the flow outside the vegetation. Therefore, a full comprehension of the flow through emergent and/or submerged vegetation has become significant for river and coastal restorations and the design of flood retention storage. Detailed knowledge about the effects of vegetation on flow will also improve the prediction of sediment transport in vegetated areas. Recent research has focused on deliberately utilizing vegetation on banks and floodplains for attenuating floods, filtering contaminants, promoting water self-purification, sheltering aquatic life, and even changing channel shape [1, 54].

To better understand the hydraulics in a natural open-channel, the following are essential: (1) fundamental understanding of flow-vegetation interaction, (2) a robust approach to quantify the effects of vegetation, and (3) simulation tools for engineering

practice. For the fundamental knowledge of hydrodynamics between vegetation and turbulent flow, flow resistance, flow structure, and flow statistics need to be analyzed.

Researchers have tried to understand such properties of vegetation by experimentally investigating the turbulent flow through vegetation. Petryk and Bosmajian [36] introduced a force-equilibrium approach and postulated that the gravity force is equal to the boundary shear stress and the drag forces induced by the emergent vegetation. The drag force of vegetation can be simply calculated using the formula for a single circular cylinder by assuming that vegetation can be idealized as a rigid circular cylinder. A number of experimental studies were carried out under varying conditions such as cylinder form (shape), dimensions (size), rigidity (or flexibility), density, spatial distribution, and the degree of submergence, which influence the drag force and flow structures [1, 19, 34, 46, 55, 57, 58, 59, 60, 65, 66].

The drag coefficient in the drag force formula in a natural channel may differ from that of an isolated cylinder due to the vegetation density. Hence, recent studies have focused on evaluating the drag force as a function of vegetation density and Reynolds number [58]; however, their experiments were conducted for cylinder Reynolds numbers of $Re_D = 30 - 700$. Although some researchers have experimentally investigated the flow field at higher cylinder Reynolds numbers [28, 55], a relationship between the drag forces and Reynolds number is still subject of ongoing research.

On the other hand, some studies have observed that the spatially- and time-averaged velocity profile within an emergent or submerged vegetated layer (irrespective of whether the vegetation is rigid or flexible) no longer follows the universal logarithmic law [5, 28, 34, 46]. Furthermore, not only the spatially-averaged velocity profile is altered considerably, but also the vertical distribution of turbulence intensities, Reynolds stresses and kinetic energy exhibit large differences from those of unobstructed channel flow [22, 28]. In a recent study Liu et al. [20] provided quantitative evidence that the local flow around single vegetation elements is spatially

heterogeneous by evaluating turbulence statistics of flow through emergent and submerged vegetation along six different verticals around one vegetation element within an array of elements.

1.1.2 Three-Dimensional Computational Fluid Dynamics models

To provide accurate flow predictions, Computational Fluid Dynamics (CFD) models have been developed in 3D such as RANS (Reynolds-averaged-Navier-Stokes) and LES (Large Eddy Simulation). In general, RANS shows high efficiency with respect to simulation time and grid generation and is used in engineering practice while LES can accurately predict turbulence and coherent structures, which makes it a good tool for researching turbulent flows.

Various RANS models have been developed for flow through vegetation, employing different turbulence models. RANS models are operated on coarser grids and vegetation drag is accounted for through additional sub-grid forces that are added to the momentum and turbulence transport equations, so that this should be referred to as a vegetation closure model. Such RANS models can offer reasonable accuracy for the prediction of the time-averaged flow field [2, 9, 25, 26, 46], but agreement with measured turbulence quantities is sometimes poor [4, 27]. This is due to the fact that turbulence is not explicitly generated because of the absence of local velocity gradients in the vicinity of the (non-resolved) vegetation; hence RANS models require modified turbulence closure models featuring drag-related sink terms in the turbulent transport equations to be able to predict reasonably well the turbulence quantities within the vegetation layer. However, source terms of both the momentum and transport equations require *a-priori* knowledge of the drag coefficient and additional empirical constants.

RANS studies report good match between prediction and results, however, even

though predicted velocities profiles matched observed profiles fairly well, several studies reported deviations for the energy gradient, i.e., the total head in the channel. The reason is that RANS models have adopted "universal" drag coefficients C_D for the momentum equations and further constants in the turbulent transport equations without consideration of their variance in different flows [4]. For instance, vegetation drag is computed through the formula for drag on a single circular cylinder assuming that vegetation can be idealized as a rigid circular cylinder and with the drag coefficient to be about $C_D = 1.0$ irrespective of the Re_D number. However, the drag coefficient in the drag force formula in a natural channel may differ from that of an isolated cylinder due to the vegetation density. In a recent study the drag coefficient was determined as a function of vegetation density and Reynolds number [58] and large deviations from unity were found.

Recently, large-eddy simulation (LES) has become a popular research tool to investigate flows in which turbulence structures dominate the flow statistics. LES provides an almost complete description of the instantaneous unsteady 3D turbulent flow field, resolving large-scale unsteadiness and asymmetries (large eddies) resulting from flow instabilities. First LES results of channel flow through vegetation were presented by Cui and Neary [3], Stoesser et al. [51], Palau et al. [33] and provided evidence that LES is able to elucidate large-scale coherent structures, their role in vegetative flow resistance, and their contribution to Reynolds stresses and turbulence quantities.

Even though the LES has such advantages, especially, accuracy, the treatment and computation of it is very demanding. Hence, LES is limited to relatively simple (vegetation) geometries and relatively low stem Reynolds numbers due to its need for very fine grids.

The final goal of CFD is definately the numerical modeling of the effect of real vegetation on the flow. One challenge is to account for the nature of the vegetation,

including its biomechanics, in a physically realistic way, for which no universal relationships exist. Another challenge is to acquire relevant input parameters from the field or from laboratory experiments, which are then fed into the numerical models.

1.2 Research Objectives

This work is a study investigating the physical mechanism involved in the flow through vegetation in open-channels. Numerical simulations were employed as a main method of investigation and their results were compared to experimental results.

The objective of the research is to provide a better understanding of acting forces, hydrodynamics, and turbulence of flow through vegetation. The following major milestones were proposed in order to achieve the overall goal:

i) Analyzing flow structures and statistics in fully-vegetated channel flow by employing high-resolution Large-Eddy Simulation

ii) Assessing the effect of vegetation density and cylinder Reynolds number on the turbulence statistics and the instantaneous flow field

iii) Calculating drag forces exerted on vegetation emulated by arrays of rigid cylinders at various densities in a fully developed flow

iv) Assessing the importance of *a-priori* knowledge of the empirical drag coefficient when using RANS with a vegetation closure model

v) Developing a low-resolution LES strategy, that is able to simulate vegetation drag directly without empirical parameters (more accurate than RANS), and that is computationally cheaper than a fully resolved LES (more efficient than the high-resolution LES)

vi) Evaluating and validating the low-resolution LES with data of different numerical and physical experiments of uniform flow through diverse arrays of emergent vegetation at varying vegetation density and stem Reynolds numbers

vii) Devising a new strategy that is based on a porosity approach instead of the cylinder analogy to simulate flow through natural vegetation with validation of its compatibility by comparing with laboratory experiments

1.3 Organization of Thesis

Chapter 1 introduces the effect of vegetation in open-channel flow and the importance of studying the behavior of turbulent flow through vegetation. The chapter also discusses some issues related to three-dimensional numerical techniques for improved simulation results in investigation of the physical mechanism between vegetation and open-channel flow. The objectives of this research and thesis outline are also included in this chapter as well.

Chapter 2 presents results of several large-eddy simulations (LES) of turbulent flow in an open channel through staggered arrays of rigid, emergent cylinders, which can be regarded as idealized vegetation.[1] In this chapter, two cylinder Reynolds numbers, $Re_D = 1340$ and $Re_D = 500$, and three vegetation densities are considered. The LES of the lowest density and at $Re_D = 1340$ corresponds to a recently completed laboratory experiment, the data of which is utilized to validate the simulations. Fairly good agreement between calculated and measured first and second order statistics along measurement profiles is found confirming the accuracy of the simulations. The high resolution of the simulations enables an explicit calculation of drag forces, decomposed into pressure and friction drag, that are exerted on the cylinders. The effect

[1] This chapter is [50] with minor modifications. The authors thank the three anonymous reviewers and the editor for their comments on the manuscript.

of the cylinder Reynolds number and the cylinder density on the drag and hence on the flow resistance is quantified and in agreement with previous experimental studies. Turbulence structures are visualized through instantaneous pressure fluctuations, isosurfaces of the Q-criterion and contours of vertical vorticity in horizontal planes. Analysis of velocity time signals and distributions of drag and lift forces over time reveals that flow and turbulence are more influenced by the vegetation density than by the cylinder Reynolds number.

Chapter 3 presents numerical simulations of flow through emergent vegetation.[2] Two simulation strategies are evaluated; (1) Reynolds Averaged Navier Stokes (RANS) based simulations employing a vegetation closure model and (2) low-resolution large-eddy simulation (LES). RANS based models offer efficiency in terms of computational resources, however it is demonstrated herein that the accuracy of RANS models depends strongly on empirical parameters of the corresponding vegetation closure model. The method of low-resolution LES is an efficient alternative to a fully resolved LES, simulates vegetation drag directly, and does not require empirical parameter input. Predictions of the vegetative flow resistance of emergent vegetation using low-resolution LES are in fairly good agreement with measurements, in particular for low and moderate vegetation densities. This is because prevailing stream- and spanwise-velocity gradients, vertical velocity profiles and recirculation zones are calculated with reasonable accuracy.

Chapter 4 provides a new strategy that is based on a porosity approach which reproduces the flow through a natural plant with leaves.[3] In order to validate the method, data from laboratory experiments of flow through a submerged natural plant

[2]This chapter is [16] with minor modifications. Su Jin Kim was supported by Georgia Water Resources Institute 104B grant No.2009GA197B. GT undergraduate students Ingrid Duque and Emma Reuter helped with collecting laboratory data. The authors also thank three unknown reviewers and the associate editor for their valuable comments on the manuscript.

[3]This chapter is a part of a manuscript with modifications. The manuscript is preparing to be submitted to the Advances in Water Resources. The manuscript presents collaborated works: experimental investigation by Sina Wunder and numerical investigation by Su Jin Kim.

are used. Flow velocities were measured at a high spatial resolution for two different conditions. After calibration and validation by comparing experimental and numerical results, a porosity approach is also determined as a formula in relation to a drag approach. The result of both porosity and drag approaches are compared with experimental data. In addition, the qualitative ability of the porosity approach is assessed with the mean flow and turbulent structures.

Finally, Chapter 5 gives the conclusions and recommendations for practical application and future research.

CHAPTER II

HIGH RESOLUTION LARGE EDDY SIMULATIONS FOR STAGGERED ARRAYS OF EMERGENT CYLINDERS

2.1 Introduction

The presence of vegetation in the aquatic environment considerably alters the turbulent flow in streams, rivers and floodplains. The additional drag exerted by plants largely influences the horizontal and vertical distributions of mean and instantaneous velocity, turbulence quantities and Reynolds stresses as well as transport of sediments and solutes. Furthermore, the flow through partially-vegetated channels or emergent and submerged vegetation is characterized by significant velocity gradients (laterally, longitudinally and vertically) resulting in shear layer formation between the canopy flow and the flow outside the vegetation. Recent research has focused on deliberately utilizing vegetation on banks and floodplains for attenuating floods, filtering contaminants, promoting water self-purification, sheltering aquatic life, and even changing channel shape [1].

In order to quantify the effects of vegetation in terms of flow resistance, Petryk and Bosmajian [36] introduced a force-equilibrium approach and postulated that the gravity force is equal to the boundary shear stress and the drag forces induced by the emergent vegetation. The drag force of vegetation can be simplistically calculated using the formula for a single circular cylinder by assuming that vegetation can be idealized as a rigid circular cylinder. A number of experimental studies further refined this approach for different flow conditions [1, 19, 34, 55, 57, 59, 65, 66]. In a recent experimental study Tanino and Nepf [58] evaluated the drag force and the drag coefficient as a function of vegetation density for various, relatively low, cylinder

Reynolds numbers ($Re_D = 30 - 700$). A number of experimental studies have focused on detailed examination of the flow field and turbulence structure within a plant canopy. These studies have involved modeling vegetation as an array of rigid cylinders of the same height and diameter at regular spacing [5, 28, 34, 46, 60] and have observed that the spatially- and time-averaged velocity profile within an emergent or submerged vegetated layer (irrespective of whether the vegetation is rigid or flexible) no longer follows the universal logarithmic law. Furthermore, not only the spatially-averaged velocity profile is altered considerably but also the vertical distribution of turbulence intensities, Reynolds stresses and kinetic energy exhibit large differences from those of unobstructed channel flow [22, 28]. In a recent study Liu et al. [20] provided quantitative evidence that the local flow around single vegetation elements is spatially heterogeneous by evaluating turbulence statistics of flow through emergent and submerged vegetation along six different verticals around one vegetation element within an array of elements.

A more complete three-dimensional picture of the flow can be obtained from Computational Fluid Dynamics (CFD) models. The majority of CFD models solve the 3D steady or unsteady Reynolds-averaged-Navier-Stokes (RANS) equations and are capable of accurately predicting the time-averaged flow field. Usually RANS models are operated on coarser grids and vegetation drag is accounted for through additional source terms that are added to the momentum and turbulence transport equations. These models are the most practical approaches offering reasonable accuracy for the prediction of the time-averaged flow field [2, 9, 25, 26, 46]. In addition to RANS models require modified turbulence closure models featuring drag-related sink terms in the turbulent transport equations to be able to predict reasonably well the turbulence quantities within the vegetation layer. The source terms of both the momentum and transport equations require a-priori knowledge of the drag coefficient and additional empirical constants. The strength of RANS or unsteady RANS (URANS) models

lies in their computational efficiency and their portability to field scale flows. Hence, RANS or URANS models have not been applied to simulate the flow through vegetation with individual plants/cylinders resolved by the numerical grid. This is probably due the fact that standard RANS/URANS models were less successful in predicting the flow and turbulence around single cylinders [23, 40] or the flow in tube bundles [11, 42]. Both flows are very similar to the flow through an idealized vegetation layer.

Recently, large-eddy simulation (LES) has become a popular research tool to investigate flows in which turbulence structures dominate the flow statistics. LES provides an almost complete description of the instantaneous unsteady 3D turbulent flow field, resolving large-scale unsteadiness and asymmetries (large eddies) resulting from flow instabilities. First LES results of channel flow through vegetation were presented by Cui and Neary [3], Stoesser et al. [51], Palau et al. [33] and provided evidence that LES is able to elucidate large-scale coherent structures, their role in vegetative flow resistance, and their contribution to Reynolds stresses and turbulence quantities.

In this paper we present large-eddy simulations of turbulent channel flow through a matrix of surface protruding circular cylinders, which can be regarded as idealized emergent vegetation. Each cylinder is explicitly resolved through a high resolution bodyfitted grid with the first grid point well within the viscous sublayer of the cylinder. This allows for the direct calculation of acting drag and lift forces. To validate the LES, time-averaged velocities and turbulence intensities are compared with laboratory data at selected profiles. The effects of vegetation density and cylinder Reynolds number on the turbulence statistics and the instantaneous flow field are discussed and analyzed.

2.2 Numerical Framework

The large-eddy simulation code (Hydro3D-GT) used in this study is based on the finite volume method on a curvilinear grid with collocated variable arrangement [48]. The Hydro3D-GT code solves the filtered Navier-Stokes equations for incompressible fluid flow [37]:

$$\frac{\partial u_i}{\partial x_i} = 0 \tag{1}$$

$$\frac{\partial u_i}{\partial t} + \frac{\partial u_i u_j}{\partial x_j} = -\frac{\partial p}{\partial x_j} + \frac{\partial \left(2\nu S_{ij}\right)}{\partial x_j} - \frac{\partial \tau_{ij}}{\partial x_j} \tag{2}$$

where u_i and u_j (i or j = 1, 2, or 3) are the resolved velocity vectors (i.e., $u_1 = u$, $u_2 = v$, and $u_3 = w$ denoting the velocity components in x, y and z axis direction, respectively) and p is the resolved pressure divided by the density. These quantities are filtered in space. Similarly, x_i and x_j represent the spatial location vectors in x, y, and z axis direction, respectively, ν is the kinematic viscosity, and S_{ij} is the filtered strain-rate tensor, defined as $S_{ij} = 1/2\left[(\partial u_i/\partial x_j) + (\partial u_j/\partial x_i)\right]$. The term τ_{ij} results from the unresolved sub-grid scale fluctuations and needs to be modeled by a sub-grid scale (SGS) model. The dynamic version of the original Smagorinsky [47] sub-grid scale (SGS) model [10] is employed to approximate the anisotropic part of τ_{ij}, i.e., ${\tau_{ij}}^a$, as ${\tau_{ij}}^a = \tau_{ij} - (2/3)\delta_{ij}k_r (= -2\nu_t S_{ij})$, where δ_{ij} =the Kronecker delta and k_r =the residual kinetic energy. Then, an anisotropic filter $\left(\Delta = (\Delta x \Delta y \Delta z)^{1/3}\right)$ together with the characteristic filtered rate of strain $\left(|S| = (2S_{ij}S_{ij})^{1/2}\right)$ are used to compute the sub-grid scale eddy viscosity ν_t as $\nu_t = (C_s\Delta)^2|S|$. The Smagorinsky constant C_s is calculated locally by making use of the flow information available from the smallest resolved scales. A double filtering procedure leads to a closed expression, commonly referred to as Germano's identity, relating filter stresses at different filter

levels to each other. This additional information is then used to determine the model parameter C_s through local averaging.

The convection and diffusion terms in the Navier-Stokes equations are approximated by central differences ensuring second-order accuracy in space. An explicit Adams-Bashforth scheme is used to discretize the equations in time providing second-order accuracy in time.

2.3 Simulation Setup

The setup for the first simulation of this study is chosen to match the experiments carried out by Liu et al. [20] the data of which is used to validate the LES. Liu et al. [20] placed a matrix of rigid cylinders in a staggered arrangement into a rectangular flume and carried out detailed LDA measurements at the six verticals within the flow as indicated in Figure 1 (a). In Figure 1, s, is defined as the distance between two-cylinders in the streamwise direction and in Liu et al.'s experiment $s = 10D$. The vegetation density ϕ, here defined as the volume that is occupied by the cylinders over the total volume, is $\phi = 0.0157$. The cylinder Reynolds number based on the bulk velocity, u_{bulk} and the cylinder diameter D is $Re_D = 1340$. In addition to the $10D$ case of Liu et al. [20], numerical experiments are carried out for two additional vegetation densities, i.e., $s = 5D$ and $s = 2.5D$, or $\phi = 0.0628$ and $\phi = 0.2513$, respectively and at one additional (lower) flow rate which yields $Re_D = 500$. In total, six different numerical experiments are performed, details for which are found in Table 1. The computational flow domain chosen is the same for all cases and spans $20D$ in streamwise, $10D$ in spanwise and $10.22D$ (corresponding to the water depth) in the vertical direction, respectively.

A block-structured grid composed of Cartesian H-grid and curvilinear O-grid blocks is employed and is depicted in Figure 2. While the Cartesian grid is uniform in the horizontal plane the grid of the O-grid block is stretched towards the cylinder. In the wall-normal direction the grid is stretched from the channel bed to the free surface. The details of each grid of the six numerical experiments are summarized in Table 2.

Table 1: Physical parameters of the simulations

	$10D$ case	$5D$ case	$2.5D$ case
Number of cylinders in the domain	4	16	64
Cylinder volume fraction, ϕ	0.0157	0.0628	0.2513
Width fraction factor, ψ	1.11	1.25	1.67

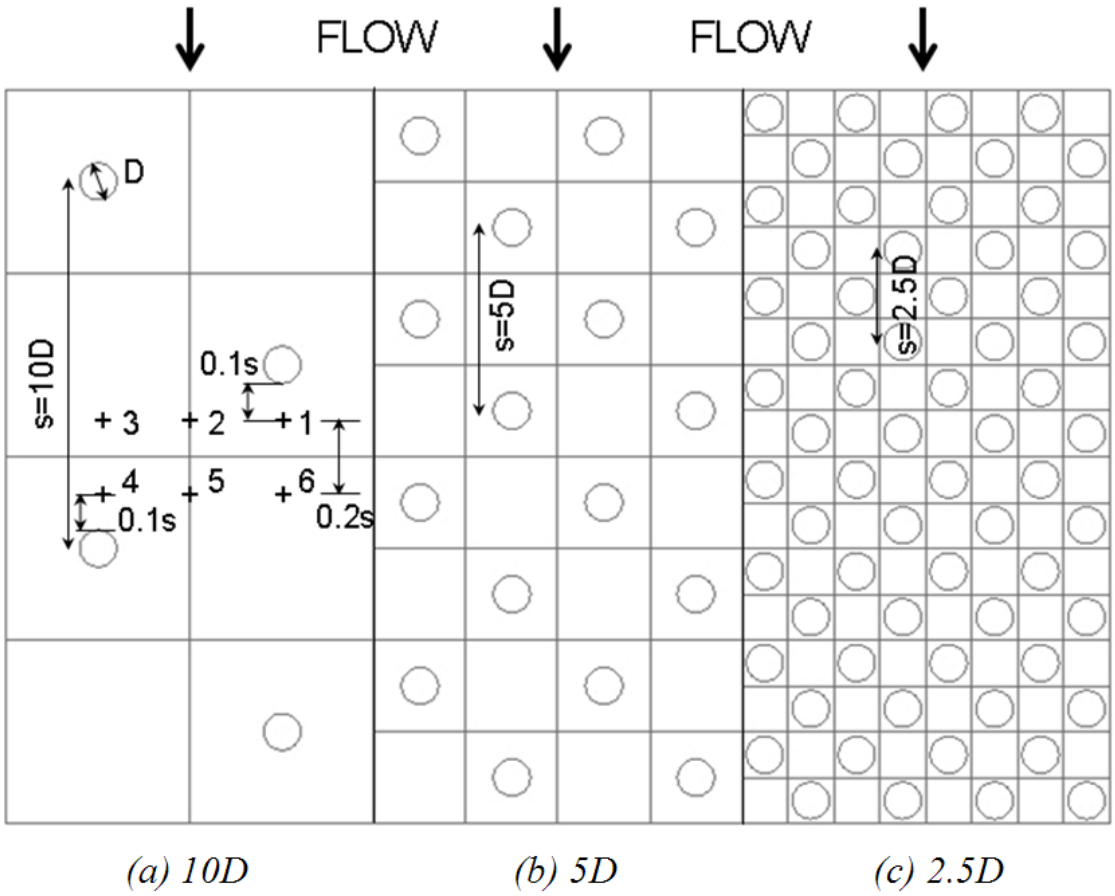

Figure 1: Flow domain and cylinder arrangement for the three different setups. The measurement locations in the experiment are also depicted.

Table 2: Numerical parameters of the simulations

Re_D	Spacing s	Gridpoints in H-grid $n_x \times n_y \times n_z \times n_{set}$	Gridpoins in O-grid $n_\theta \times n_r \times n_z \times n_{set}$	Total number of gridpoints
1,340	$10D$	$82 \times 82 \times 122 \times 4$	$(82 \times 4) \times 52 \times 122 \times 4$	11,604,640
	$5D$	$62 \times 62 \times 122 \times 16$	$(62 \times 4) \times 32 \times 122 \times 16$	22,994,560
	$2.5D$	$42 \times 42 \times 122 \times 64$	$(42 \times 4) \times 12 \times 122 \times 64$	29,514,240
500	$10D$	$62 \times 62 \times 122 \times 4$	$(62 \times 4) \times 47 \times 122 \times 4$	7,564,000
	$5D$	$42 \times 42 \times 122 \times 16$	$(42 \times 4) \times 27 \times 122 \times 16$	12,297,600
	$2.5D$	$22 \times 22 \times 122 \times 64$	$(22 \times 4) \times 9 \times 122 \times 64$	9,963,008

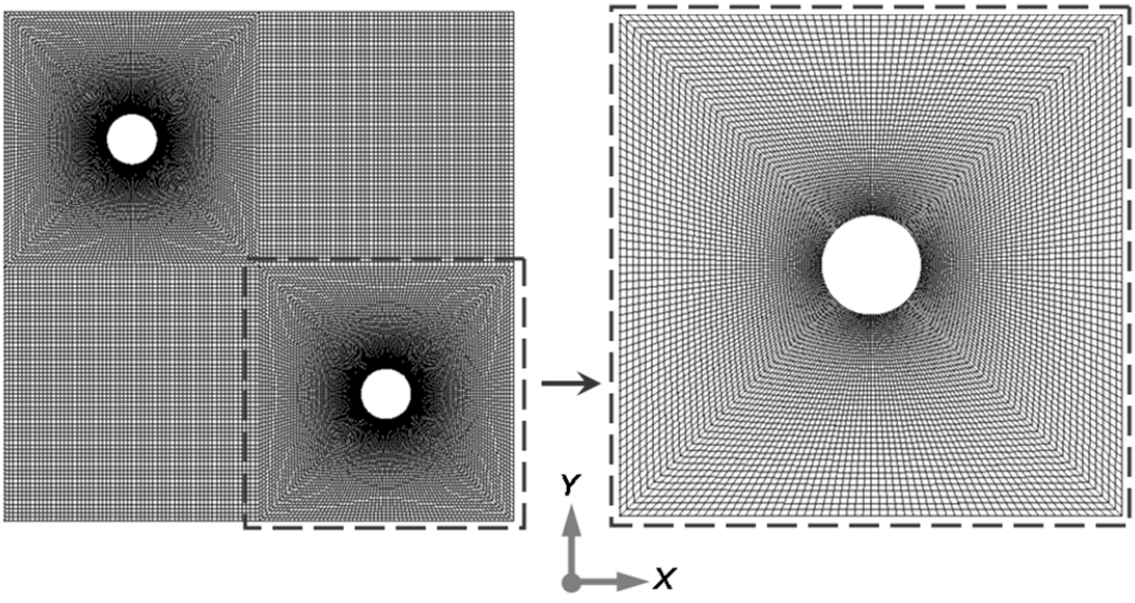

Figure 2: Part of the employed grid for the $10D$ case showing (a) block-structured grid composed of H- and O-grids (b) stretched O-grid for the cylinder region

2.4 Boundary Conditions

At the channel bed and at the cylinder wall the no-slip boundary condition is applied. This is justified by the fact that $3-4$ points off the wall are situated within the viscous sublayer. Figure 3 presents the distribution of the dimensionless wall distance $y^+ = \Delta y u_*/\nu$ around the cylinder for the three different vegetation densities at $Re_D = 1340$. The upper row of Figure 3 presents contours of y^+ and it can be seen that only locally maximum values of $y^+ = 7$ prevail. A more quantitative distribution of the dimensionless wall-spacing is provided in the lower row of Figure 3 where y^+ values at three different elevations, i.e., near the bed, at mid depth and near the water surface along the circumference of the cylinder are plotted. This figure provides proof of the validity of using the no-slip condition because in all three cases the wall distance is found to be in the order of $y^+ = 1$ for most of the circumference. However, towards the point of flow separation, i.e., where the highest velocities tangential to the cylinder wall are found, maximum values of $y^+ = 4$ in the $10D$ case, $y^+ = 5$ in the $5D$ case and $y^+ = 6$ in the $2.5D$ case are observed. Though those values are still below $y^+ = 11$, i.e., the edge of the viscous sublayer an additional simulation for the $10D$, $Re_D = 1340$ at a considerably finer grid resolution is carried out. This is considered the (worst) case in terms of grid resolution and it can be seen from Figure 3, that the near wall resolution is approximately two times higher in the finer grid than in the original grid.

Periodic boundary conditions are applied in the streamwise and spanwise directions, and the free surface is set as a frictionless rigid lid and is treated as a plane of symmetry. The simulations are initially run for about 20 eddy turn-over time units, t_e, defined as the water depth over the friction velocity, in order to establish fully developed flow conditions. For the calculation of flow and turbulence statistics the simulations are then continued for 50+ eddy turn-over time units. The code uses an adjustable time step size based on the CFL criteria with maximum CFL numbers of

0.5. The code is parallelized using MPI and the maximum number of CPUs employed in this study is 288 for the $2.5D$ case and consumed approximately 110,000 CPUh for approximately 300,000 timesteps.

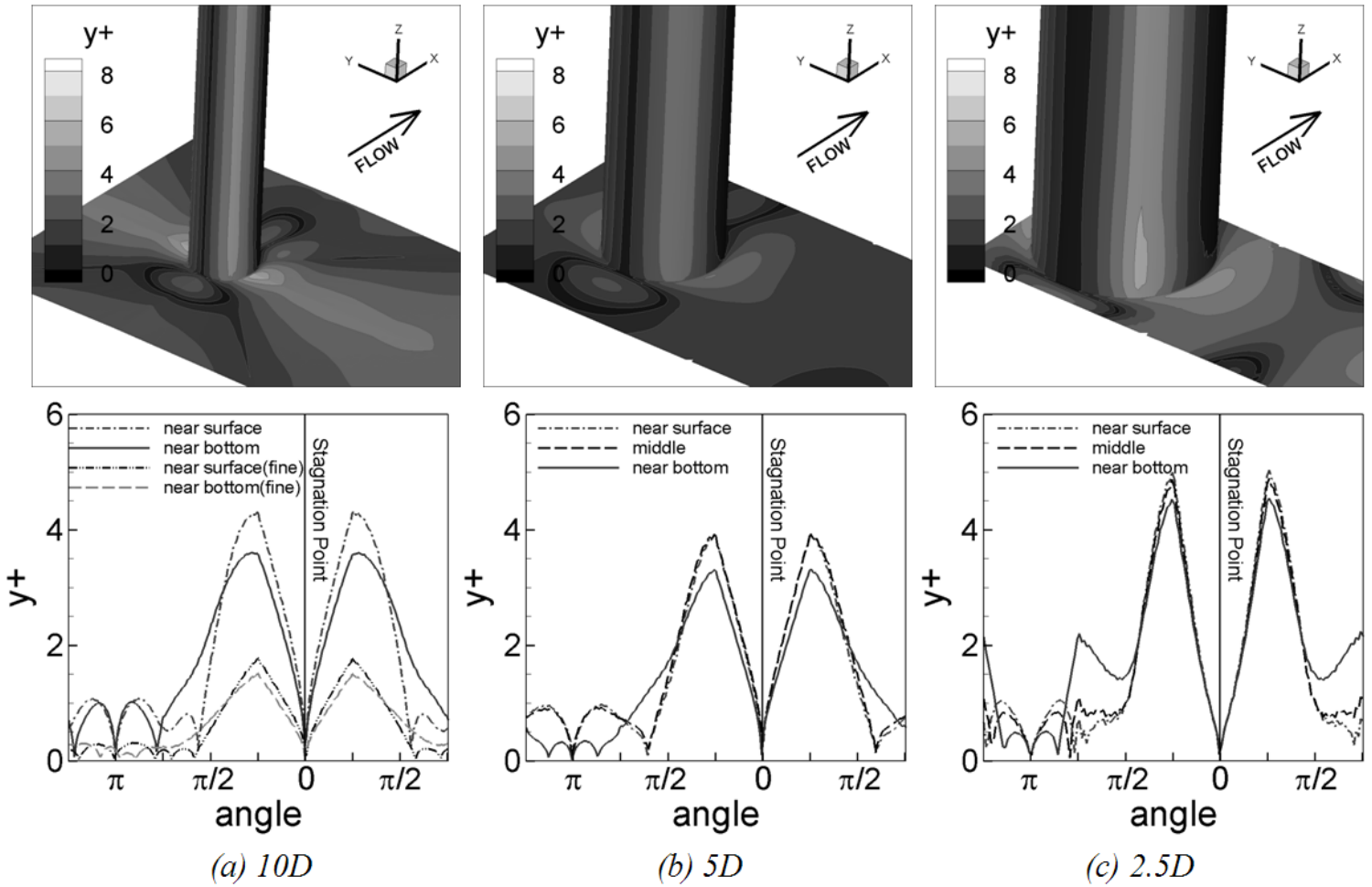

Figure 3: Contours of the dimensionless wall distance around the cylinder (above) and y^+ distributions around the cylinder circumference at three selected heights (below). The stagnation point is located at zero.

2.5 Results and Discussion

2.5.1 Time-Averaged Flow Field and Turbulence Statistics

Figure 4 presents the LES calculated time-averaged and normalized (with the bulk velocity) streamwise velocities along six profiles for the three vegetation densities, i.e., $10D$, $5D$ and $2.5D$. Also plotted are the results from the finer grid simulation and the experimental velocity data with which the simulation of the $10D$ case is validated. First of all, differences between original-grid and finer-grid LES are negligibly small, confirming the adequacy of the original grid. The velocity profiles of the $10D$ simulation (black and gray solid lines) match the Liu et al. [20] observations quite well in particular at Profiles #3, #4, #1 and #6, i.e., along the profiles in front of the cylinder and behind the cylinder (Figure 1). There is a local acceleration of the flow near the surface just behind the cylinder, i.e., Profile #1, which might be the result of a local water-surface depression (the water-surface was not measured in great detail hence this is speculative). The fact that this feature is not picked up by the LES (using a rigid lid) supports the hypothesis of a local water surface depression. Also, there is a small but consistent overestimation of calculated streamwise velocity magnitude of approximately 7 % visible in Profiles #2 and #5. This could be due to an underestimation of u_{bulk}, or due to the fact that the flow is slightly deeper between cylinders, or both. Noteworthy is a near bed velocity bulge in Verticals #1 and #6 in the $10D$ case that is accurately predicted by the LES. This velocity bulge is a result of the prevailing secondary flow (discussed below) entraining high momentum fluid into the wake near the bed. This mechanism has been discussed by Liu et al. [20] as well. Such a distinct velocity bulge is absent or less pronounced, respectively, in the $5D$ and $2.5D$ cases. Worth mentioning is the fact that streamwise velocities are found to be almost constant over the depth and vegetation density and that the profiles deviates marginally from a logarithmic distribution irrespective of location.

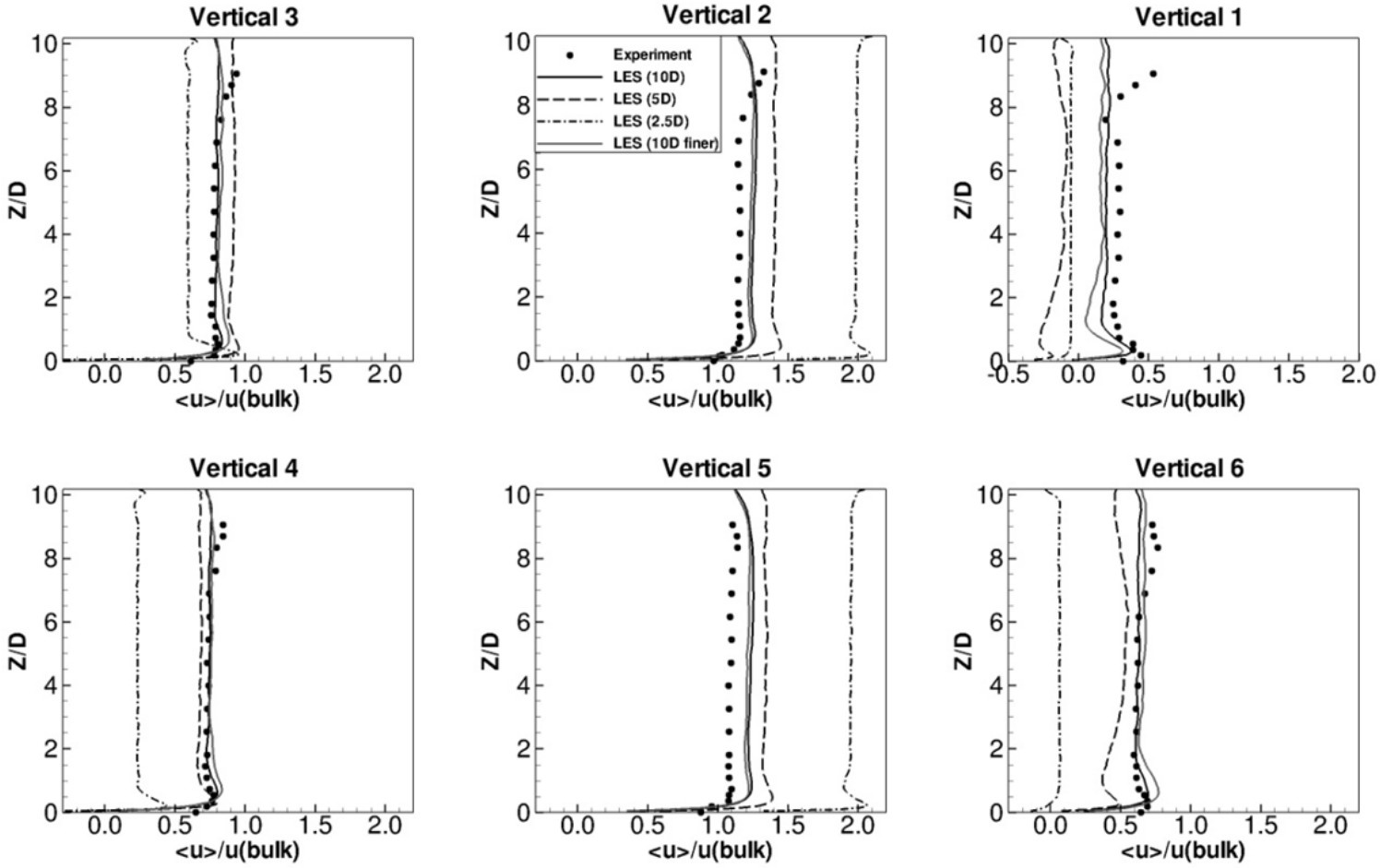

Figure 4: Time-averaged streamwise velocity profile along the six selected verticals for the $10D$, $5D$ and $2.5D$ case at $Re_D = 1340$

Figure 5 compares calculated vertical velocities with measured data along the six verticals for the $10D$ case but also includes profiles for the other two cases. The agreement between the $10D$ case simulation and the experiment is quite good, regardless of grid resolution. Overall very small vertical velocities are observed in both $10D$ and $5D$ cases except just behind the cylinder (Verticals #1 and #6) where relatively large values of vertical velocity indicate considerable upward movement of fluid. In the $2.5D$ case, however, upward and downward movement of fluid is observed close to the bed in all verticals.

Figure 6 presents contours of the time-averaged streamwise velocity and streamlines at about half depth for the three different vegetation densities investigated. While in the $10D$ and $5D$ cases a clear wake behind the cylinder and an area of higher velocities between the cylinders is identified, the $2.5D$ flow field exhibits large velocity gradients in both streamwise and spanwise directions. In the $10D$ and $5D$ cases the maximum velocity is found to be about 30 % higher than the bulk velocity, whereas in the $2.5D$ case the flow accelerates to about 2.5 times the bulk velocity between cylinders. The streamlines of the flow, presented in the lower half of the figure, reveal that the $10D$ and $5D$ cases exhibit similar flow features, i.e., flow separation at approximately 95° and a relatively large recirculation region comprising two counter-rotating vortices that are about the length of the cylinder diameter. In the $2.5D$ case the flow separates considerably later (at approximately 130°) and the recirculation region behind the cylinder in the $2.5D$ case is much smaller than the ones found behind the cylinders of the $10D$ and $5D$ case, respectively. The length of the vortex pair behind the $2.5D$ case cylinder is approximately only 1/4 of the cylinder diameter.

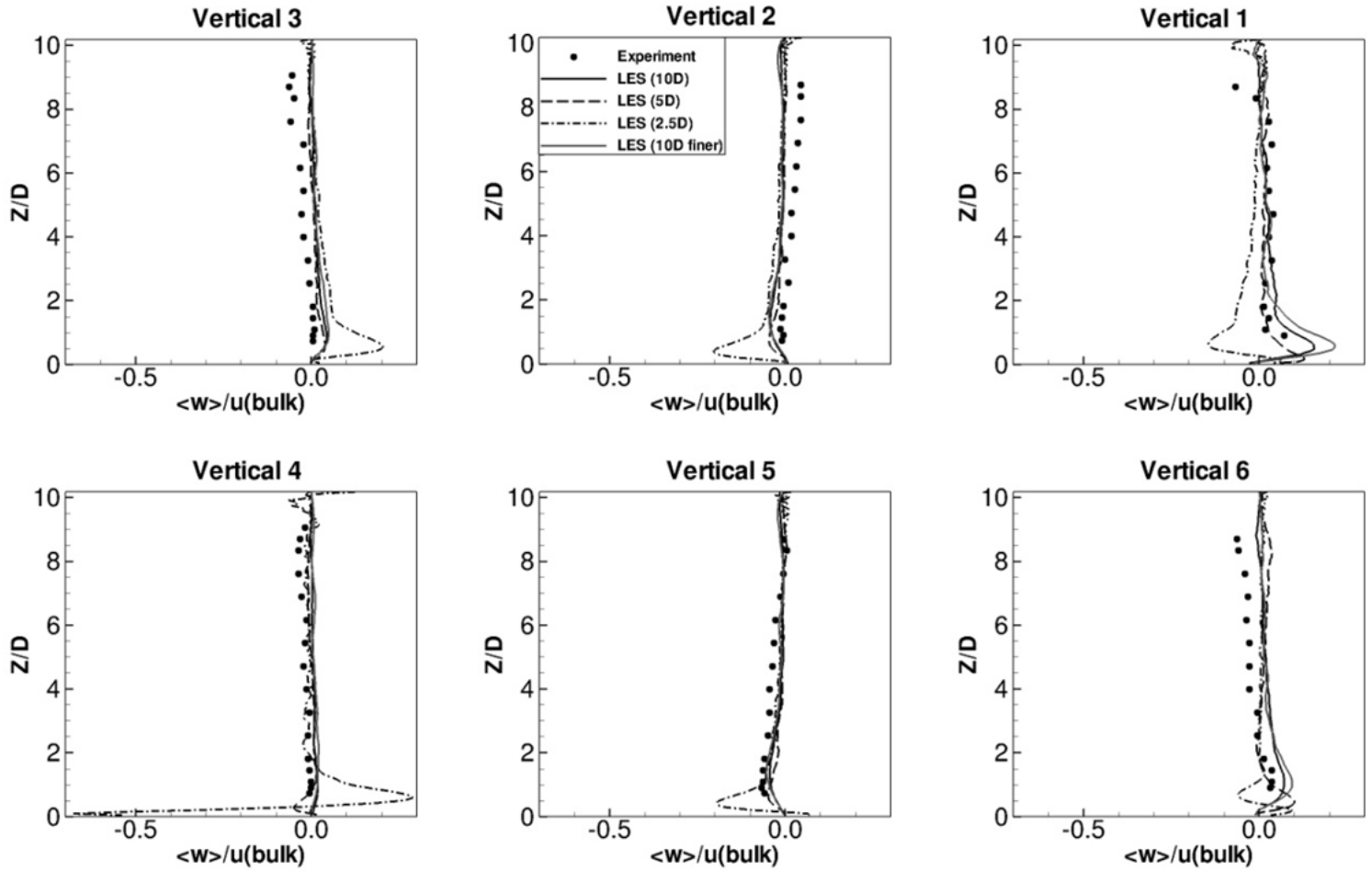

Figure 5: Time-averaged vertical velocity profile along the six selected verticals for the $10D$, $5D$ and $2.5D$ case at $Re_D = 1340$

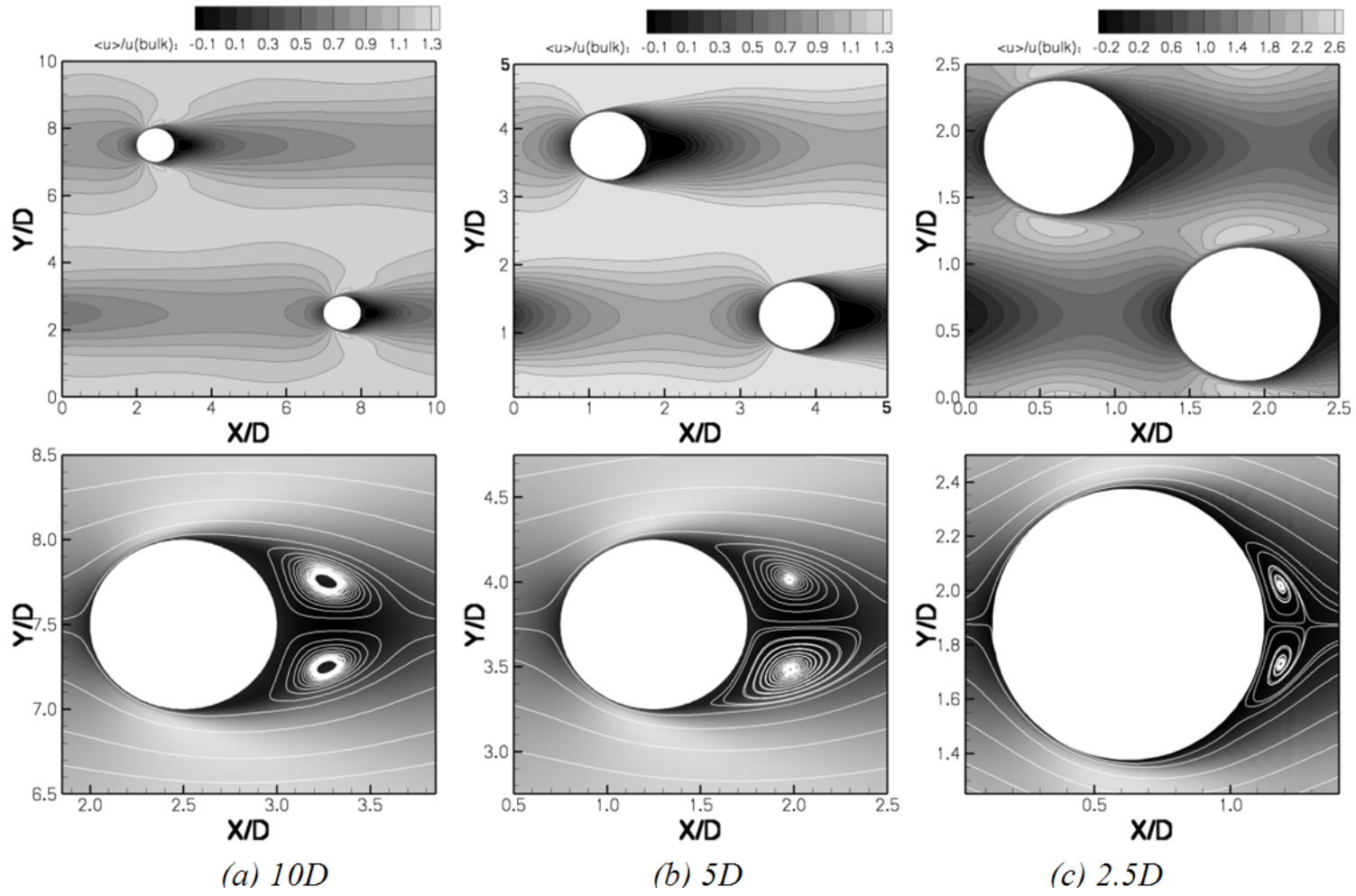

Figure 6: Distribution of time-averaged streamwise velocities in a horizontal plane at $Z/D = 0.5$ (upper row) and streamlines around the cylinder (lower row) for the 3 cases at $Re_D = 1340$

Figure 7 presents contours of the primary flow velocity and streamlines of the secondary flow in three selected cross sections for the three vegetation densities. In the $10D$ case (upper row) a distinct secondary flow pattern develops behind the cylinder featuring a counter-rotating vortex pair near the bed. This vortex pair is a result of fluid entrainment from the high momentum region between the cylinders filling the low momentum wake behind the cylinder. The fluid that enters the wake behind the cylinder from either side converges at the cylinder-axis, initiates an upflow (see also Profile #1 in Figure 5) and results in the vortex pair. The vortex pair diminishes rather quickly. In the $5D$ case (middle row) a similar counter-rotating vortex pair is also being formed, however it appears to be flatter and less developed than in the $10D$ case. The distance behind the cylinder is too short for the vortices to fully develop. Also the upflow of fluid behind the cylinder is slightly weaker than in the $10D$ case (see also Profile #1 in Figure 5). The $2.5D$ case does not exhibit a distinct secondary flow pattern, nevertheless strong vertical movement is observed but only very close to the bed (see also Figure 5). Also interesting is the fact that behind the $2.5D$ cylinder downflow occurs whereas in the other two cases upflow is found.

The above discussed flow features are reflected in the turbulence intensity distribution along the six verticals. In Figure 8 measured (for the $10D$ case from Liu et al. [20]) and computed streamwise turbulence intensities (i.e., the RMS of the velocity fluctuation normalized with the bulk velocity, u'/u_{bulk}) are plotted. The comparison of computed streamwise turbulence intensities (solid line) with the measured values is very agreeable (regardless of grid resolution). The biggest differences are found near the bed in Vertical #1, which is the recirculation region with the highest turbulence, where the finer grid provides a better match, hence discrepancies in the original grid simulation can be attributed to the fact that only the resolved RMS quantities of the LES are plotted. The sreamwise turbulence intensity profiles are similar for all three cases and are almost a straight vertical line. This is significantly different from

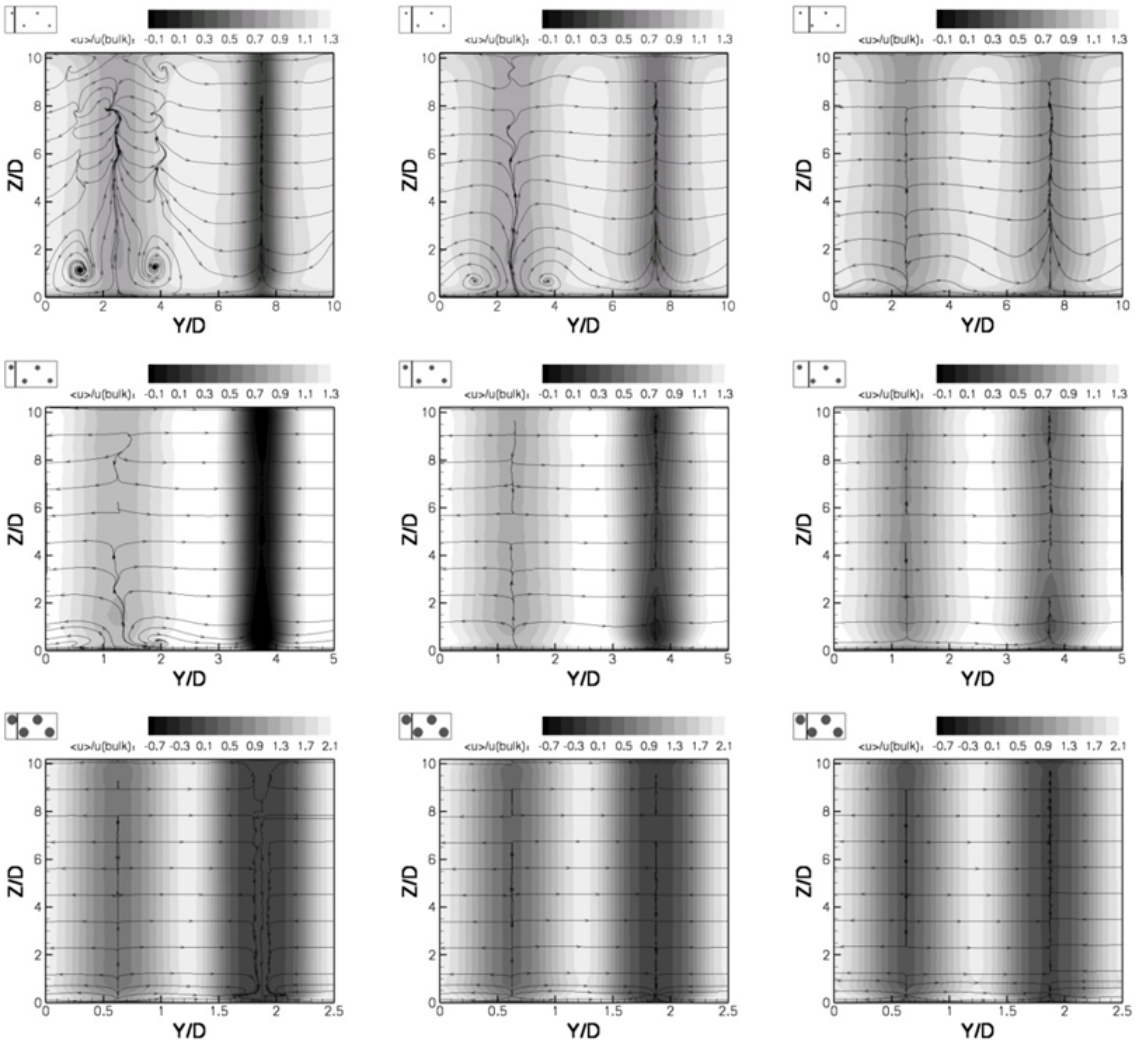

Figure 7: Distribution of time-averaged streamwise velocity and streamlines of the secondary flow in three cross-sections (the location is indicated in the sketch in the upper left of each figure and corresponds to $X/D = 1s/4$, $X/D = 2s/4$, $X/D = 3s/4$) for the $10D$ (upper row), $5D$ (middle row), and $2.5D$ (lower row) cases at $Re_D = 1340$

unobstructed channel flow not only in shape but also in magnitude. The $10D$ and the $5D$ cases exhibit the same behaviour, however slightly higher streamwise turbulence intensities are observed in the $5D$ case. The $2.5D$ case exhibits considerably higher streamwise turbulence intensities, in particular between the cylinders (i.e., Verticals #2 and #5), which is a result of both spanwise and streamwise velocity gradients. The strong up and down flow close to the bed in the $2.5D$ case is reflected in kinks in the streamwise turbulence intensity profiles near the bed.

A quantitative comparison between measured [20] and computed normalized vertical turbulence intensities (for the $10D$ case) is provided in Figure 9. Computed vertical turbulence intensities are in good agreement with the measurements for all six verticals. The distributions from the finer grid simulation are identical to the ones from the original grid. A small peak can be seen near the bed of Profile #1, a result of the relatively strong upward movement of fluid behind the cylinder. The $5D$ and the $2.5D$ distributions of vertical turbulence intensity are generally similar to the $10D$ case, but with higher magnitudes. There are peaks of vertical turbulence intensity near the bed in the $2.5D$ case, a result of the strong vertical movement.

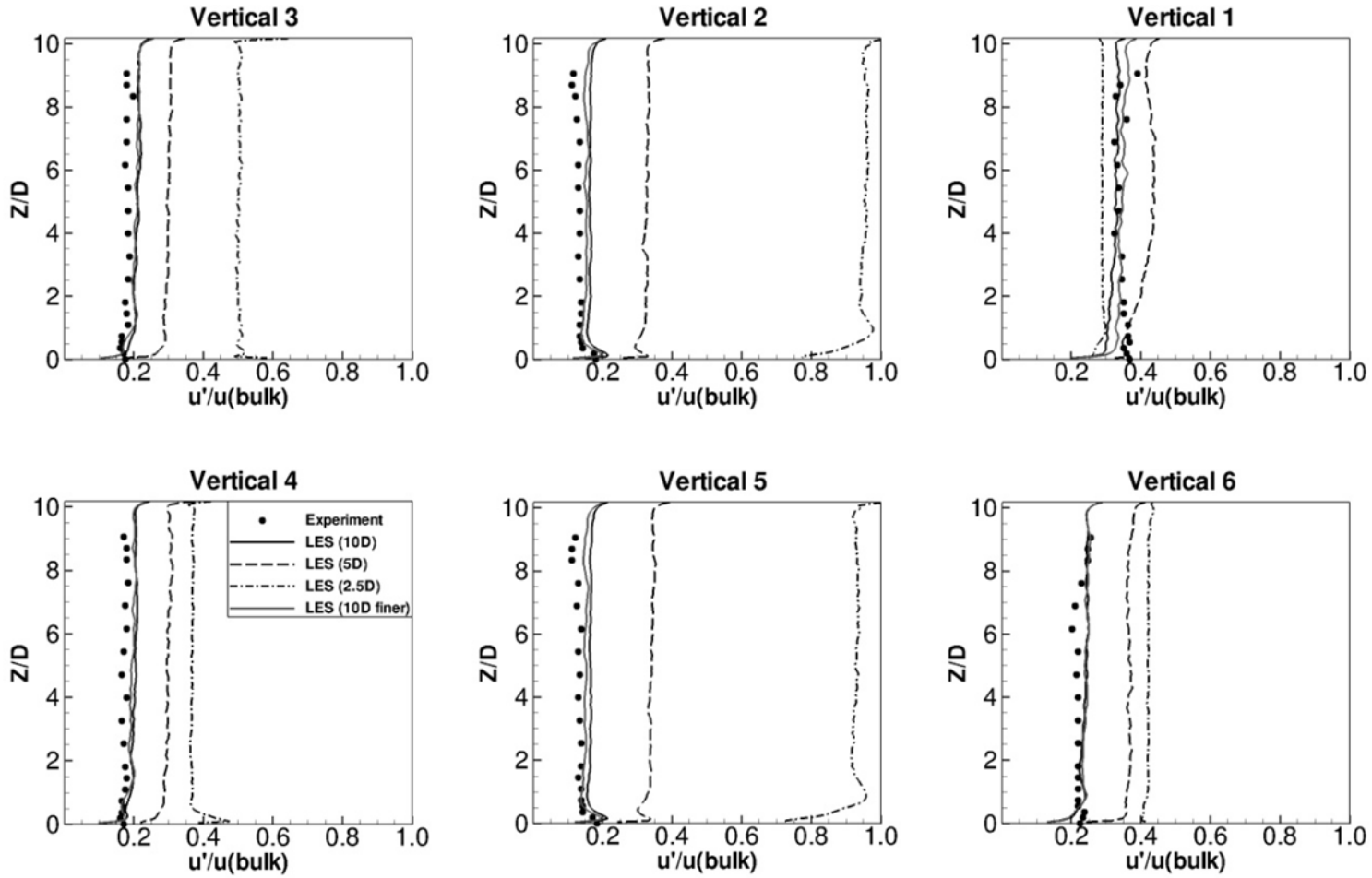

Figure 8: Profiles of streamwise turbulence intensities of the LES along the six selected verticals for the $10D$, $5D$ and $2.5D$ case at $Re_D = 1340$

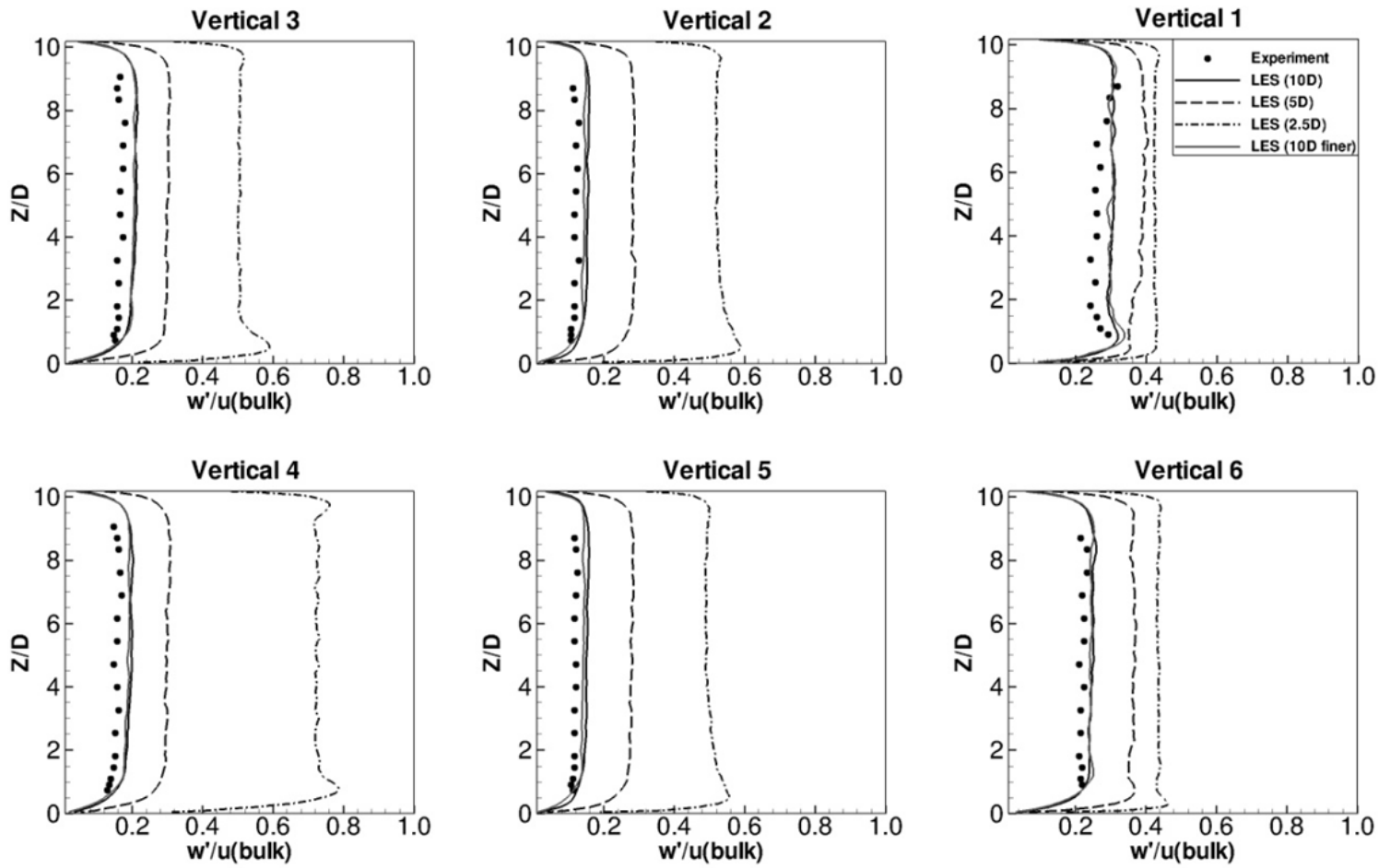

Figure 9: Profiles of vertical turbulence intensities of the LES along the six selected verticals for the $10D$, $5D$ and $2.5D$ case at $Re_D = 1340$

Figure 10 depicts turbulence intensities of the three components of the velocity vector in a horizontal plane at approximately half depth ($Z = 5D$). While the $10D$ and $5D$ distributions of turbulence intensities are similar to each other, the $2.5D$ distributions are obviously different from the $10D$ and $5D$ cases. The most obvious difference is that the wake of the $10D$ and $5D$ case is characterized by high turbulence intensities while the wake of the $2.5D$ case has lower values of turbulence intensity. In the $10D$ case there is a corridor between cylinders (i.e., around $Y/D = 5$) which is characterized by very low values of turbulence intensities. This implies that the flow and turbulence downstream of the cylinder is not affected by the cylinders that are arranged laterally. In the $5D$ case the distribution of turbulence intensities do not exhibit a distinct corridor with low values suggesting that the wake behind the cylinder is influenced by lateral cylinders. In the $2.5D$ case highest turbulence intensities are found in the area between the cylinders, being a result of local acceleration in the streamwise direction. In the $10D$ and $5D$ cases streamwise turbulence intensities peaks are observed downstream of the flow separation from the cylinder (i.e., 95°) resulting in a sickle shaped distribution of maximum turbulence intensities. The distributions look very similar to those of the flow around a long isolated cylinder. The streamwise turbulence intensity peaks in the $2.5D$ case occur clearly upstream of flow separation, which is where the maximum streamwise velocity is found (see also Figure 6). Areas of high spanwise and vertical turbulence intensities are present in the vicinity of the stagnation point. This is due to vortices that are shed upstream impinging on the cylinder. In the $2.5D$ case the highest spanwise and vertical turbulence intensities occur upstream of the cylinder, while there is hardly any turbulence downstream of the cylinder. This is due to the fact that the $2.5D$ case does not exhibit distinct vortex shedding as in single cylinder flow. Clearly the turbulence in the $2.5D$ case is rather generated by high streamwise velocity gradients, while von Karman vortex shedding occurs in the $5D$ and $10D$ cases.

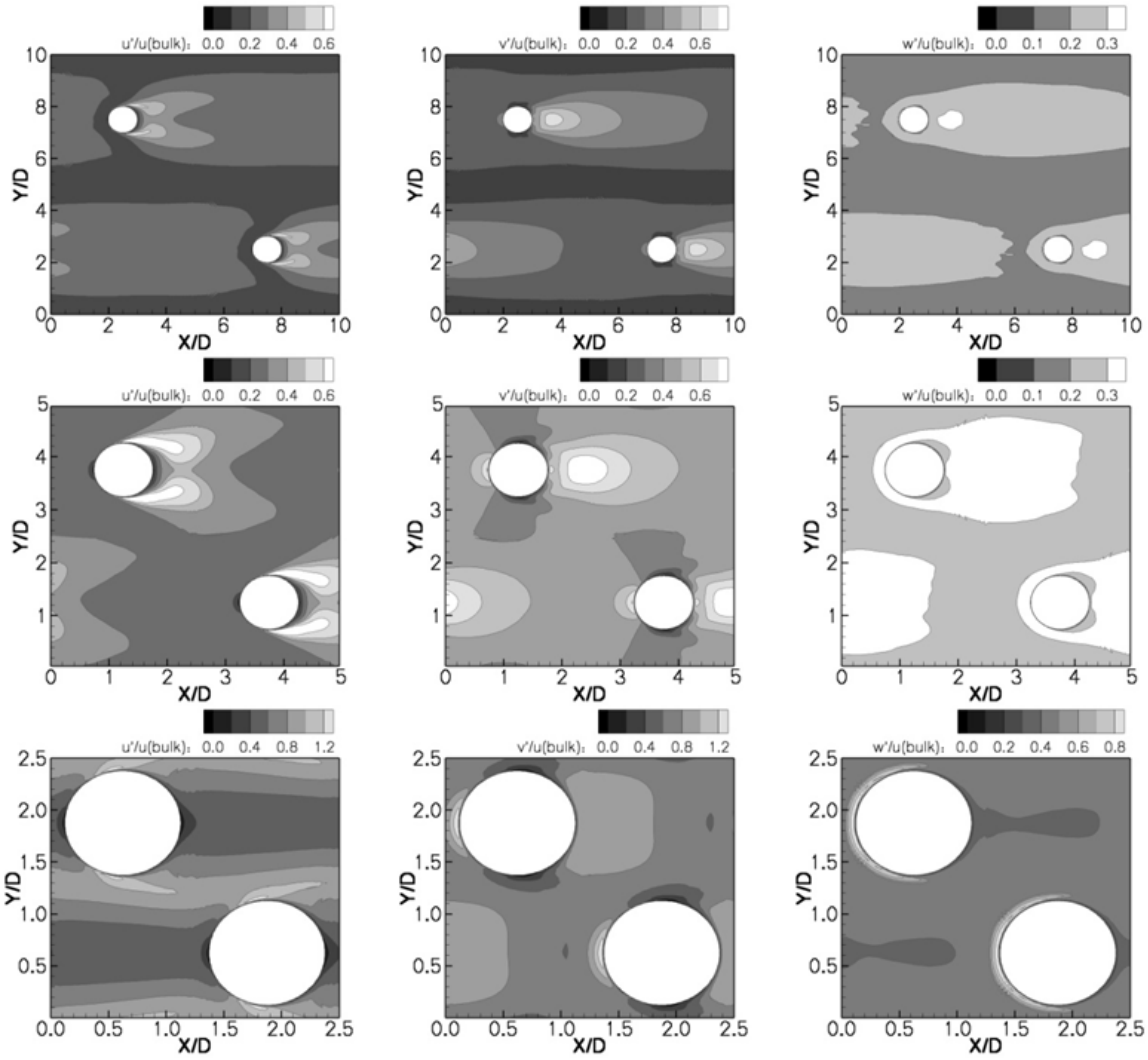

Figure 10: Distribution of the three turbulence intensities(u'/u_{bulk}, left column; v'/u_{bulk}, middle column; w'/u_{bulk}, right column) at half depth for the three vegetation densities ($10D$, top row; $5D$, middle row; $2.5D$, lower row)

Drag forces on the cylinder are a result of pressure differences between the upstream and downstream side of the cylinder and by viscous stresses on the cylinder. From the time-averaged velocity and pressure fields the drag force on the cylinder, decomposed into a pressure drag and a friction drag component, and the friction drag on the channel bed are calculated. Figure 11(a) presents contours of the time-averaged pressure coefficient C_p on one cylinder of the $10D$ case from different perspectives (i.e., at the front view, side view and rear view). High C_p values are found in the vicinity of the stagnation point and the magnitude is almost constant over the entire cylinder height. Time-averaged flow separation occurs at approximately 95°, the location at which the coefficient of pressure turns negative due to the formation of the recirculation zone behind the cylinder. The negative pressure coefficient behind the cylinder is seen in the rear view, again showing almost constant C_p values over the entire depth. Streamlines on the $10D$ cylinder, viewed from three different perspectives, are provided in Figure 11(b). The flow diverges at the stagnation point and the time-averaged flow appears to be two-dimensional except close to the bottom, where some downward movement is observed. The side view shows the separation line at a fairly constant angle of 95°. This line is therefore largely vertical and only at the bottom it is slightly bent in the downstream direction as the separation occurs a little later. In the rear region the motion is primarily backwards and upward along the cylinder as was discussed already. Near the bed there is only a backward component around the cylinder, which seems to be originating from a nodal point near the ground. This backward motion near the ground rolls up, as it approaches the slightly delayed separation point at the sidewall so that a focal point develops associated with a vortex. This vortex however is very close to the bed, is very weak and quickly disappears.

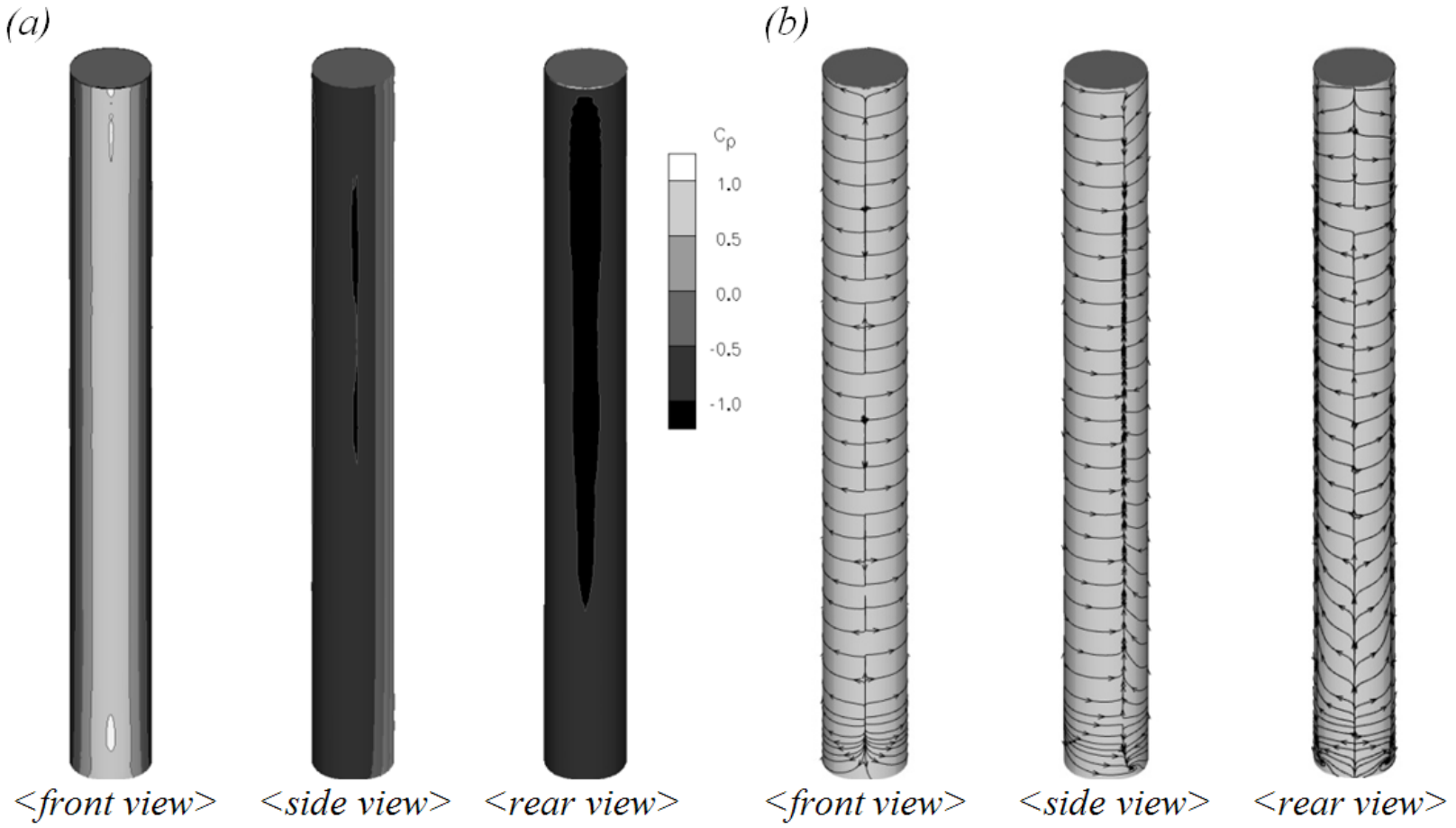

Figure 11: (a) Pressure distribution and (b) streamlines on one cylinders of the $10D$ case

Figure 12 presents the contributions of both pressure drag and friction drag on the cylinder as well as the integral force from the bed shear stresses to the total flow resistance in channel flow through vegetation for the three vegetation densities and the two cylinder Reynolds numbers Re_D. Clearly, flow resistance is mainly due to the presence of the cylinder. For the higher Re-number cases pressure drag accounts for approximately 90 %, friction drag for approximately $6-7$ % and the bed shear stress decreases with increasing vegetation density and is almost negligible, especially in the $2.5D$ case. The vegetation density has almost no effect on the percentage distribution of the contributing forces to the overall loss. For the lower Re_D cases shear forces are slightly increased, however, pressure drag still accounts for about $80-90$ % of the total loss. The portion of friction drag is constant regardless of vegetation density and the contribution of bed shear stress decreases with an increase in vegetation density.

The normalized drag force, defined as $F_D = f_D/(\mu u_{bulk} h)$, on the cylinder is compared with measured normalized drag forces of flow through emergent vegetation from a recent experimental study [58]. Tanino and Nepf [58] carried out laboratory experiments to investigate the effect of cylinder Reynolds number and vegetation density (characterized by the solid volume fraction, $\phi = m\pi D^2/4$, in which m is the number of cylinders per unit horizontal area) on the drag force and on the drag coefficient. Tanino and Nepf [58] covered a fairly wide range of vegetation densities, i.e., $0.091 < \phi < 0.35$. The LES presented herein have a vegetation density of $\phi = 0.016$, 0.063, and 0.251, for the $10D$, $5D$ and $2.5D$ case, respectively.

The LES calculated drag forces as a function of cylinder Reynolds number are plotted together with Tanino and Nepf's measured values in Figure 13. The LES complement nicely the previous experimental observations and match the observed trends remarkably well. This is particularly obvious for the $2.5D$ case (with $\phi = 0.25$) for which the LES computed drag force can be regarded as a direct extension to the measured drag forces from the experiment with almost the same density of $\phi = 0.27$.

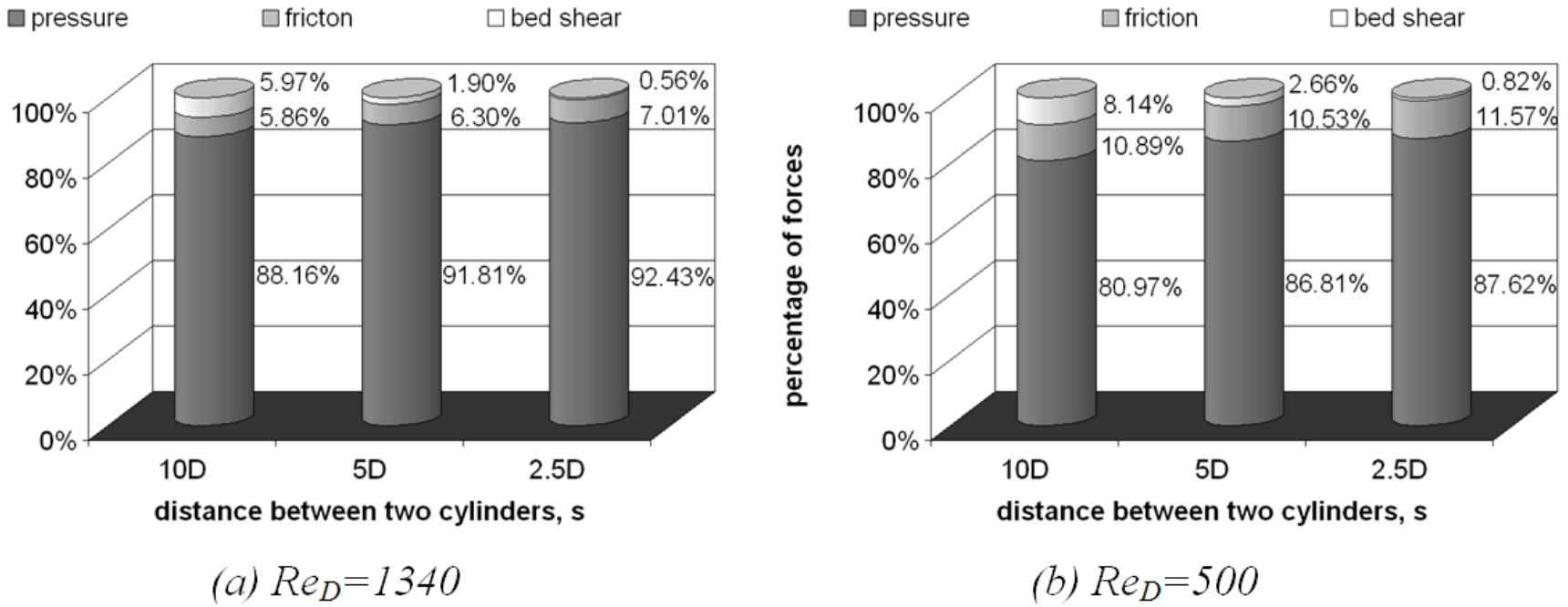

Figure 12: Contributions of pressure drag, friction drag, and bed shear to the total energy loss in flow through vegetation at various vegetation density and Reynolds numbers

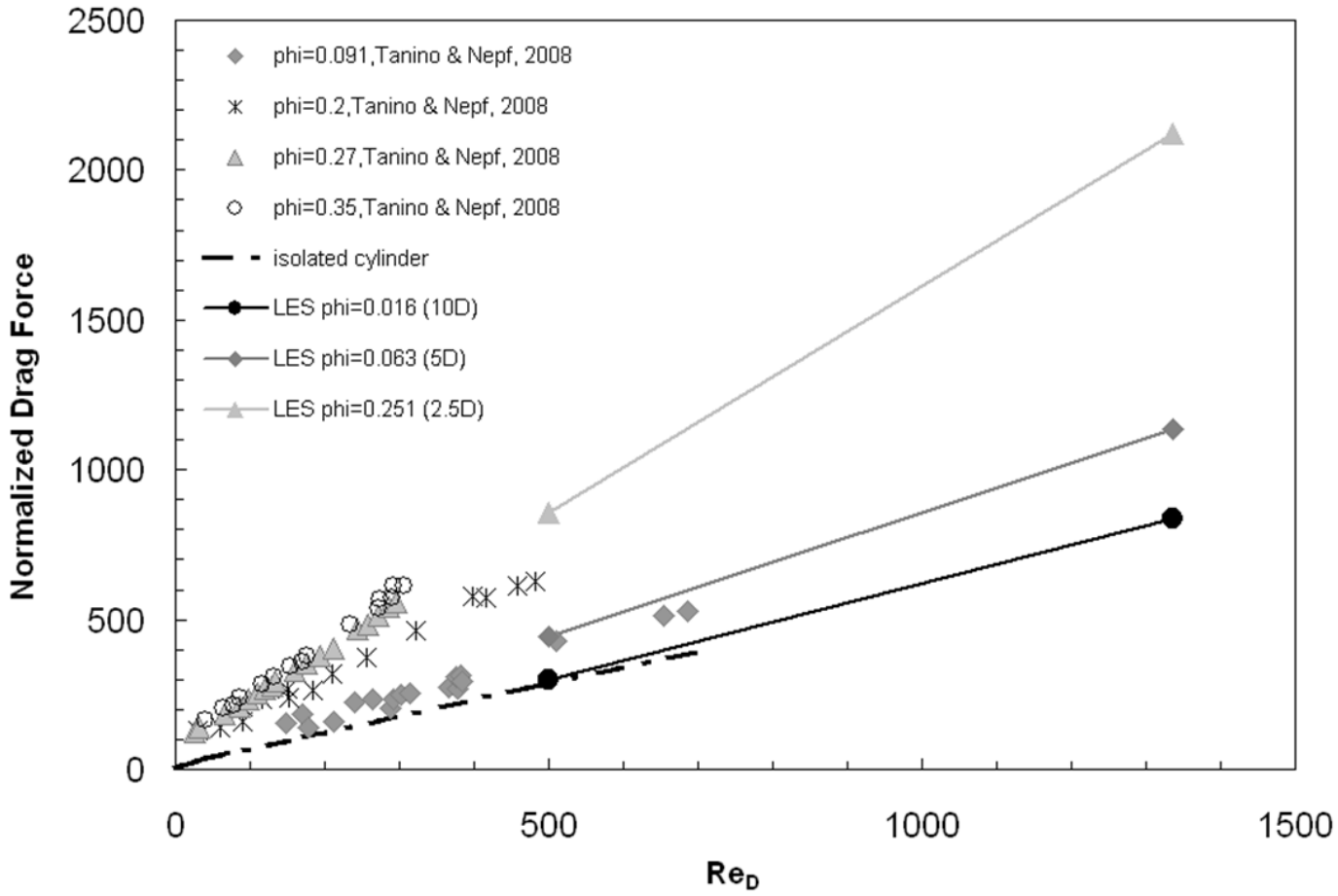

Figure 13: Normalized drag force, $F_D = f_D / (\mu u_{bulk} h)$ as a function of cylinder Reynolds number for various vegetation densities

The drag force distribution of the $10D$ case exhibits the same behavior as an isolated cylinder (dashed line, [64]) suggesting that the flow recovers sufficiently behind each cylinder. With an increase in both the vegetation density and the cylinder Reynolds number the drag force increases.

Drag coefficients are calculated and are compared with the values obtained by Tanino and Nepf [58] in Figure 14. The calculated drag coefficients C_D show a reasonable match with the extrapolated line from the experimental data. The drag coefficient is clearly a function of the cylinder Reynolds number, at least for lower values of Re_D. A greater influence on the value of C_D is the vegetation density, and it seems that the increase is linear, i.e., as the vegetation density doubles, the value of the drag coefficient doubles.

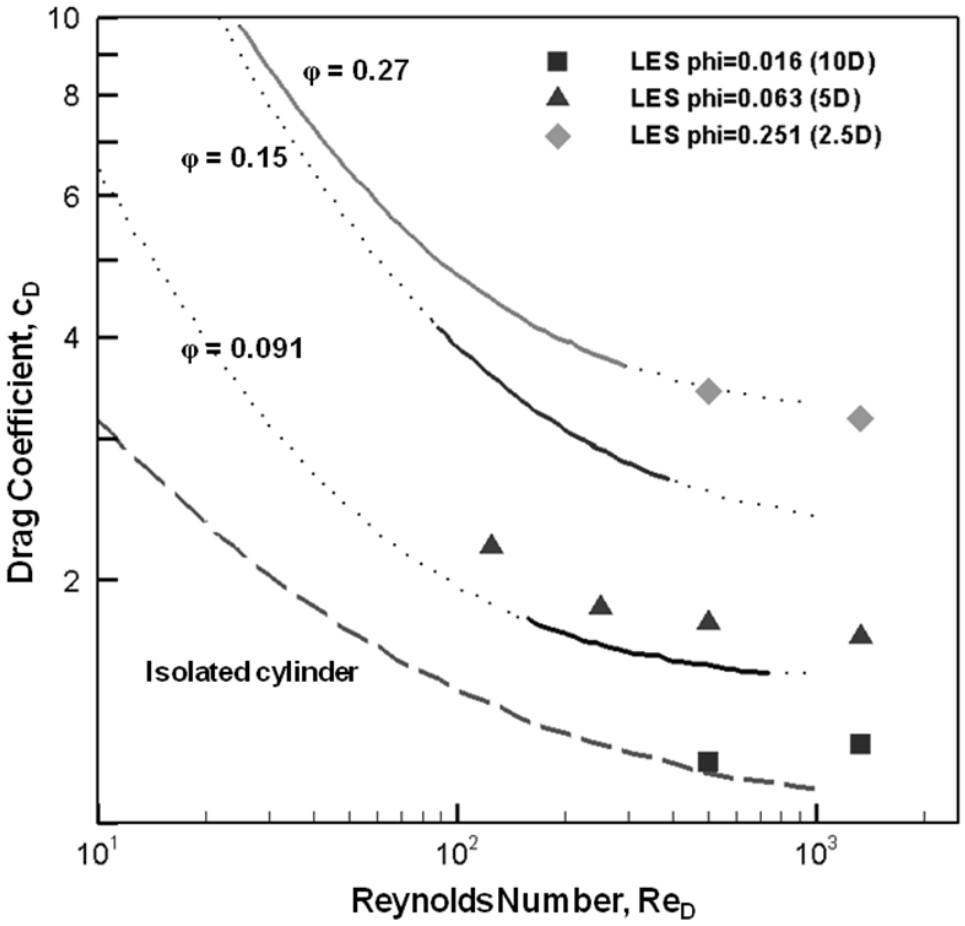

Figure 14: Drag coefficient C_D as a function of cylinder Reynolds number for various vegetation densities (lines represent experimental data from Tanino and Nepf [58])

2.5.2 Instantaneous Flow Field and Turbulence Structures

An impression of the development of large-scale vortical structures can be obtained from the temporal development of iso-surfaces of the pressure perturbation $p' = (p - \langle p \rangle) / \left(\rho {U_\infty}^2\right)$. Snapshots showing such iso-surfaces in an oblique view are presented in Figure 15. For both the $10D$ and $5D$ cases vortices are observed shedding from the cylinder due to Kelvin Helmholtz instability. These vortices extend over the full cylinder height, display clear two-dimensionality and are similar to von Karman vortices behind long isolated cylinders. In the $2.5D$ case the process is influenced strongly by the above discussed flow acceleration between cylinders and the prevailing high levels of turbulence, which alter the shedding process. As a result, these vortices are less coherent and do not exhibit clear two-dimensionality.

Snapshots of three-dimensional turbulence structures visualized with iso-surfaces of the Q-criterion [12] for the three vegetation densities are presented in Figure 16. In the $10D$ case (upper row) the above mentioned von Karman-type vortices are clearly visible. While these structures exhibit two-dimensionality in their early stage, they are stretched in the streamwise direction and packets of smaller vortices evolve, which eventually impinge on the downstream cylinder. In the above mentioned corridor between cylinders there are hardly any vortices present supporting the above made statements that the flow behind the cylinder is not interfered with structures from lateral cylinders. In the blow-up on the right hand side of Figure 16(a) the occurrence of alternating vortex shedding is indicated by the black lines. In Figure 16(a) alternating shedding is observed, the vortices on opposite sides being offset and the distance between vortices on the same side being rather large. In the $5D$ case, depicted in Figure 16(b), the vortex shedding from the cylinder walls is influenced by vortices shed from upstream and lateral cylinders. The quasi two-dimensional structure of the von Karman vortices is apparent close to the cylinder. In contrast

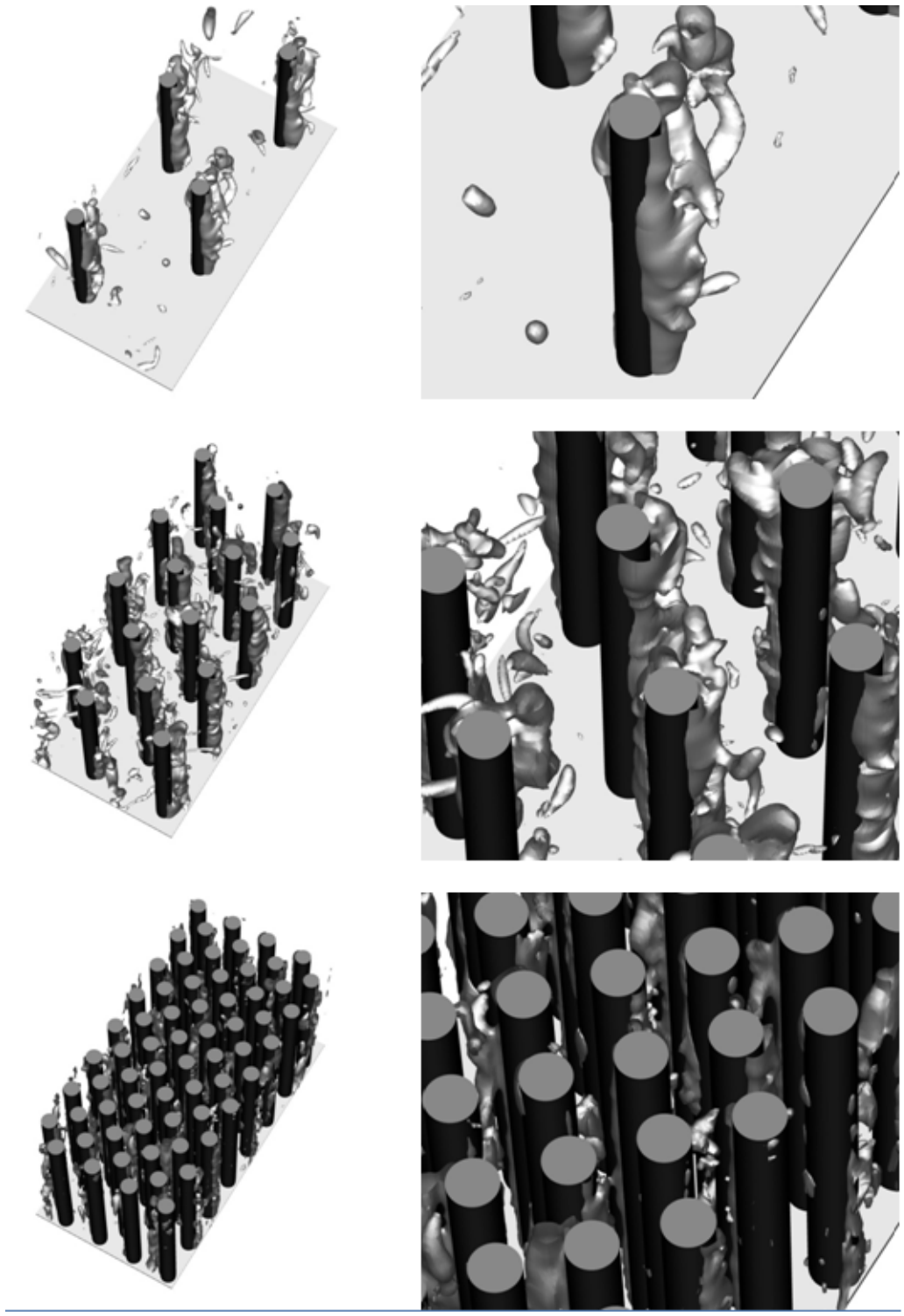

Figure 15: Isosurfaces of pressure fluctuations for the three vegetation densities ($10D$, upper row; $5D$, middle row; $2.5D$, lower row)

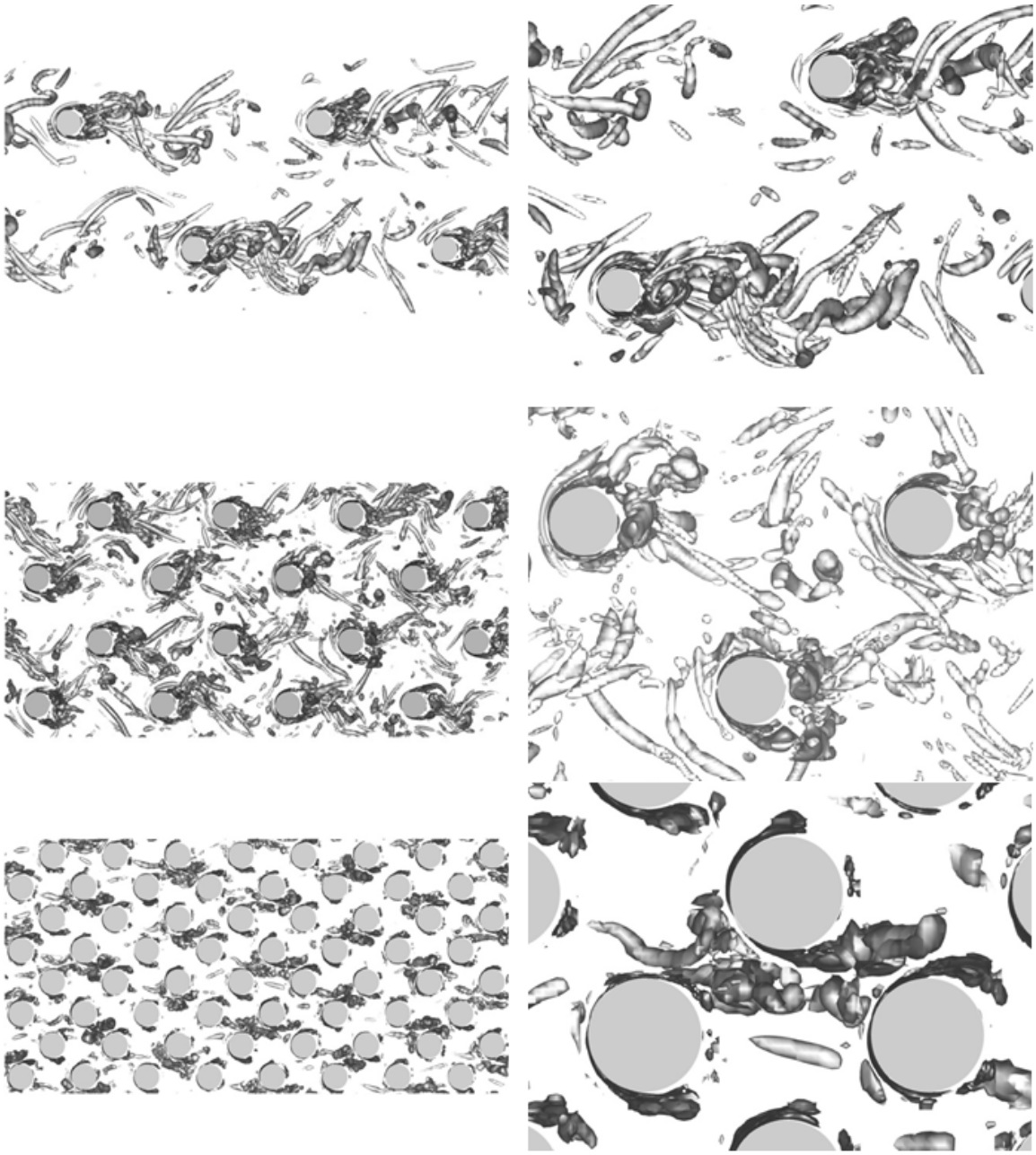

Figure 16: Instantaneous isosurfaces of the Q-criterion for the three vegetation densities ($10D$, upper row; $5D$, middle row; $2.5D$, lower row)

to the $10D$ case these vortices remain rather strong when they impinge on the downstream cylinder, with the consequence that they alter the shedding behaviour of the vortices there. Also vortices from lateral cylinders seem to be entering the wake behind the cylinder. These flow features are reflected in the shedding behaviour and whilst in the $10D$ case only regular, alternating shedding is observed, shedding in the $5D$ case becomes more irregular. Both alternating vortex shedding (A-B-C) as well as symmetric shedding (D-E), i.e., the vortices on opposite sides show little longitudinal offset, is seen. The vortex interference is amplified in the $2.5D$ case (Figure 16(c)) and vortex shedding occurs irregularly. In the blow-up on the right hand side of Figure 16(c) both alternating (A-B) and symmetric (D-E) shedding is observed. The frequency of vortex shedding is visibly increased, i.e., the longitudinal distance between vortex cores is much shorter in the $2.5D$ case than in the $10D$ and $5D$ cases. Animations of the $2.5D$ case have shown that some vortices impinge on the cylinder located immediately downstream while others are convected through the gaps and impinge on a lateral cylinder further downstream. Also, these vortices maintain their strength over a considerable distance. These animations can be accessed at (http://cfd.ce.gatech.edu/index_files/ASCEvegetation.htm)

The horizontal distribution of vertical vorticity (z-vorticity) at an instant in time and in a plane approximately at half water depth ($Z = 5D$) for the three vegetation densities is presented in Figure 17. The findings from the analysis of Figures 15 and 16 are confirmed by the contours of vertical vorticity. In the $10D$ case strong two-dimensionality of the von Karman vortices close to the cylinder is indicated with high levels of vertical vorticity, decreasing while the vortices are being convected downstream. In the vicinity of the downstream cylinder z-vorticity magnitudes are close to zero. Regular alternating shedding of clockwise and counter-clockwise rotating vortices occurs. As the density of vegetation increases, the vortex shedding at the cylinders is influenced by vortices that are shed from upstream cylinders resulting in

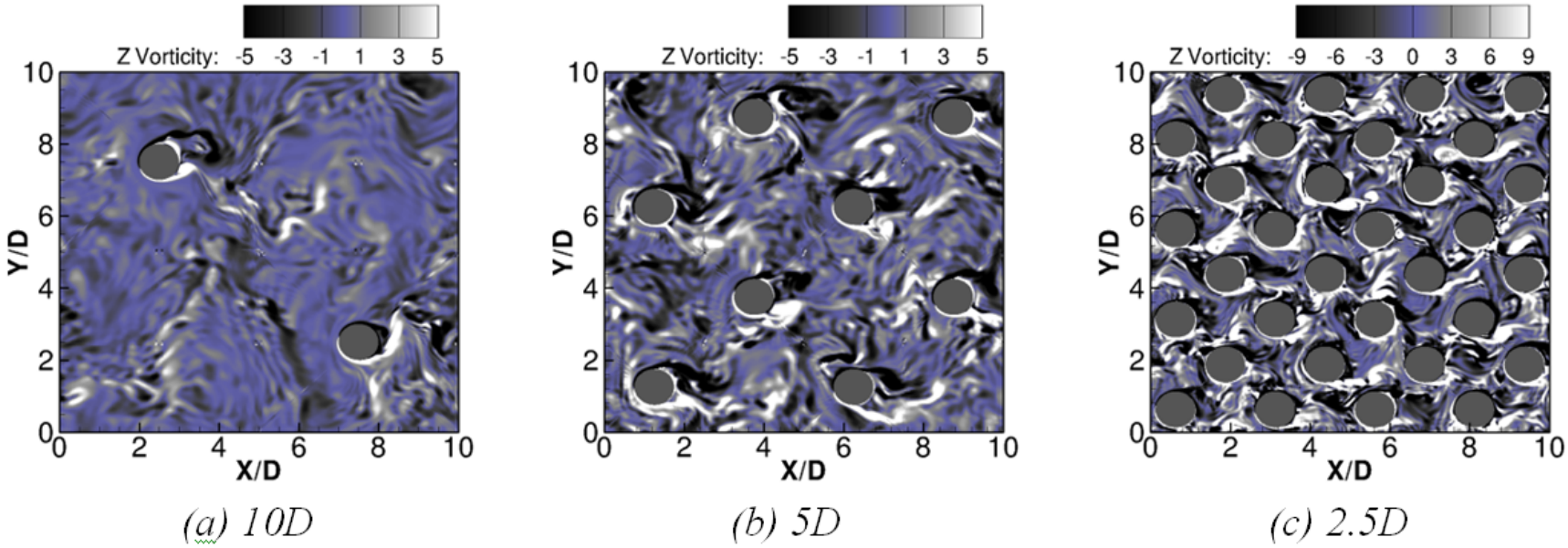

Figure 17: Contours of instantaneous vorticity in a horizontal plane at half channel depth for the three vegetation densities. Note that the $2.5D$ case has a different scale.

a more irregular shedding behaviour. This is supported by elevated levels of vertical vorticity in front of cylinders in the $5D$ case. The magnitude of vertical vorticity in the $5D$ case is similar to the $10D$ case. A further increase in vegetation density results in an increase in vorticity magnitude with the magnitude of vertical vorticity levels being almost twice as high in the $2.5D$ case as in the $10D$ or $5D$ case, respectively.

Time signals of all three velocity components were recorded at selected points over a duration of 0.5 (for the $2.5D$ case) to 1.0 (for the $10D$ case) in dimensionless eddy turn over time units $t_e = H/u_*$ by storing every 10th point in time. Spectra of the streamwise and spanwise components obtained with the method of Welch [38] are reported here as they best reveal the presence of von Karman vortex shedding. Also probability density functions (PDF) of the time signal were obtained to further analyze the instantaneous flow field. Spectra in the cylinder wake at approximately half depth are depicted in the upper row of Figure 18 for the three vegetation densities. The vortex shedding frequency is identified as a distinct peak in the velocity spectra, in particular the one of the spanwise velocity component. For the $10D$ case the peak occurs at approximately $f = 30$ Hz corresponding to a Strouhal number of $S_t = fD/u_{bulk} = 0.197$ while for the $5D$ case a slightly higher shedding frequency ($f = 32$ Hz) is obtained from the peak in the spectra and corresponds to a Strouhal number of $S_t = 0.21$. For the $2.5D$ case however, vortex shedding occurs at a much higher frequency, in fact almost three times as high as the other two cases ($f = 90$ Hz). This corresponds to a Strouhal number of $S_t = 0.5$. Furthermore, the spectra of the $10D$ case and in large parts of the $5D$ case exhibit a pronounced $-5/3$ (dotted line) decay of energy as typically observed in wake flows with alternating vortex shedding. The velocity spectrum for the $5D$ case arguably exhibits two different slopes in the inertial range as is notable when comparing to the two straight lines representing the $-5/3$ slope (dotted line) and a $-5/2$ slope (dashed line). It seems that at higher frequencies energy transfer to smaller scales is accomplished at higher rates, suggest-

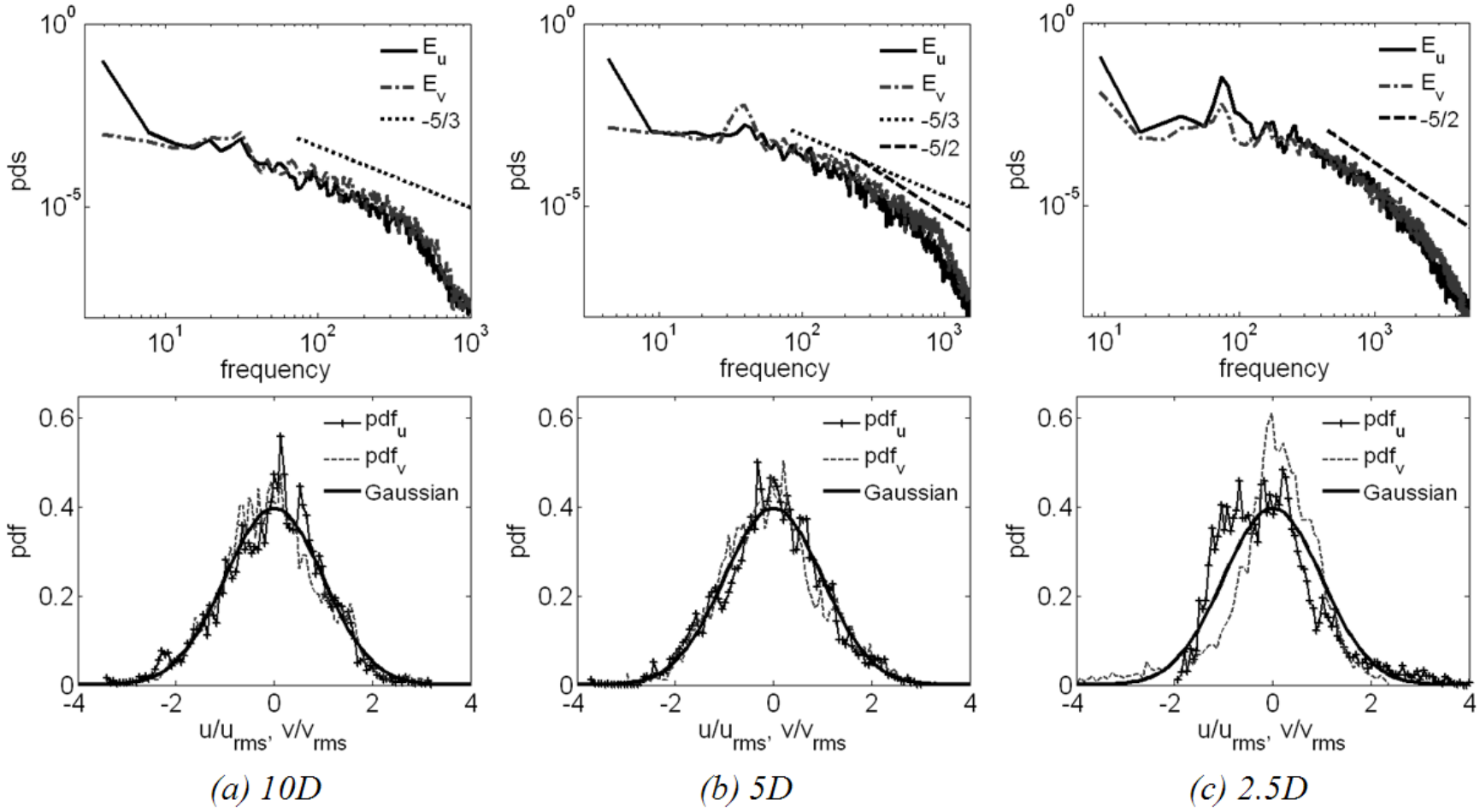

Figure 18: Time signals of the streamwise and spanwise velocity component (upper row) velocity spectra (middle row) and normalized probability density function (lower row) at a location (half depth) along Vertical #2

ing vortex interference. Rather interesting is the velocity spectrum of the $2.5D$ case: vortex interference is clearly visible as the spectrum exhibits multiple peaks, i.e., vortices that are shed at upstream cylinders and entering the wake of the present cylinder. This is in good qualitative agreement with Umeda and Yang [63] who investigated vortex shedding in dense tube bundles. The two additional peaks have similar levels of energy than the primary peak and reflect additional vortices shed from an upstream cylinder and a cylinder located laterally. Also noteworthy is the fact that the inertial subrange (here covered over a frequency decade) in the $2.5D$ case does not exhibit the classical $-5/3$ Kolmogorov subrange but rather follows a steeper $-5/2$ energy transfer range. This is the result of strong streamwise and spanwise velocity gradients with the vortex being confinement and accelerated between cylinders. This obviously results in faster energy transfer from large scales to small scales. For all three cases the range in frequency between the shedding mode(s) and the high-frequency mode with larger slope, at which energy is rapidly dissipated via SGS modelling, spans more than a decade. In amplitude the range is almost 2 decades. Both ranges covered by the LES demonstrate the good spatial and temporal resolution of the simulations.

The normalized PDF of the streamwise and vertical velocity signals of the $10D$ and $5D$ cases show a similar behaviour and appear to be distributed normally. Fairly significant differences are observed in PDF of the $2.5D$ case for both streamwise and spanwise velocity signal. Both functions differ from a Gaussian distribution (solid line). The v-velocity function has a pronounced peak around the zero value and seems to be skewed towards positive values but the signals are quite noisy and longer time-series is needed to provide conclusive evidence. The u-velocity function exhibits a multi-modal behaviour, a result of periodically passing through of vortices passing through the close spacing between cylinders.

Normalized (with the total drag) drag and lift forces on one cylinder over several

eddy turn over time periods for the three cases and the two Reynolds numbers are plotted in Figure 19. The drag and lift forces on the cylinder are due to vortex shedding and the shedding frequency is represented in the peaks of the drag force and well pronounced in the positive and negative peak values of the lift force. The smaller amplitude of the lift force at some instants in time in the $10D$ and $5D$ cases can be attributed to upstream turbulence. The severe vortex interaction in the $2.5D$ case is visible in the distribution of the lift force over time as the line is not as smooth as in the other cases showing the above mentioned high-frequency fluctuations. For the lower cylinder Reynolds number, the shedding frequencies are almost identical for the $10D$ and $5D$ cases while with an increase in viscous effects, the shedding frequency is decreased in the $2.5D$ case leading to a lower Strouhal numbers of $S_t = 0.5$ for the $Re_D = 500$ case.

The Strouhal numbers of the six simulations performed in this study are plotted in Figure 20 together with values from previous studies. All observations made above suggest that the $10D$ case exhibits features that are very similar to single cylinder flow and this is also confirmed by the comparison of the S_t number as a function of Re_D. The values obtained herein match rather well the isolated cylinder values of Zhang and Dalton [69], Kevlahan [15] or Liu and Fu [21] or the theoretical curve provided by Norberg [30] which is a result of an extensive literature review on flow around isolated cylinders. For the cylinder Reynolds numbers covered herein, the Strouhal number in the flow through vegetation appears to be independent of Re_D a finding that is in line with observations made for isolated cylinders. As the density increases there is an increase in Strouhal number but again no obvious dependency on the cylinder Reynolds number. Comparison with the experiments of flow through a staggered array of cylinders (also at a density of $5D$) confirms this finding. The Strouhal numbers obtained in this study match the ones found by Lam and Lo [18] pretty well. The distribution of the Strouhal number as a function of Re_D for the

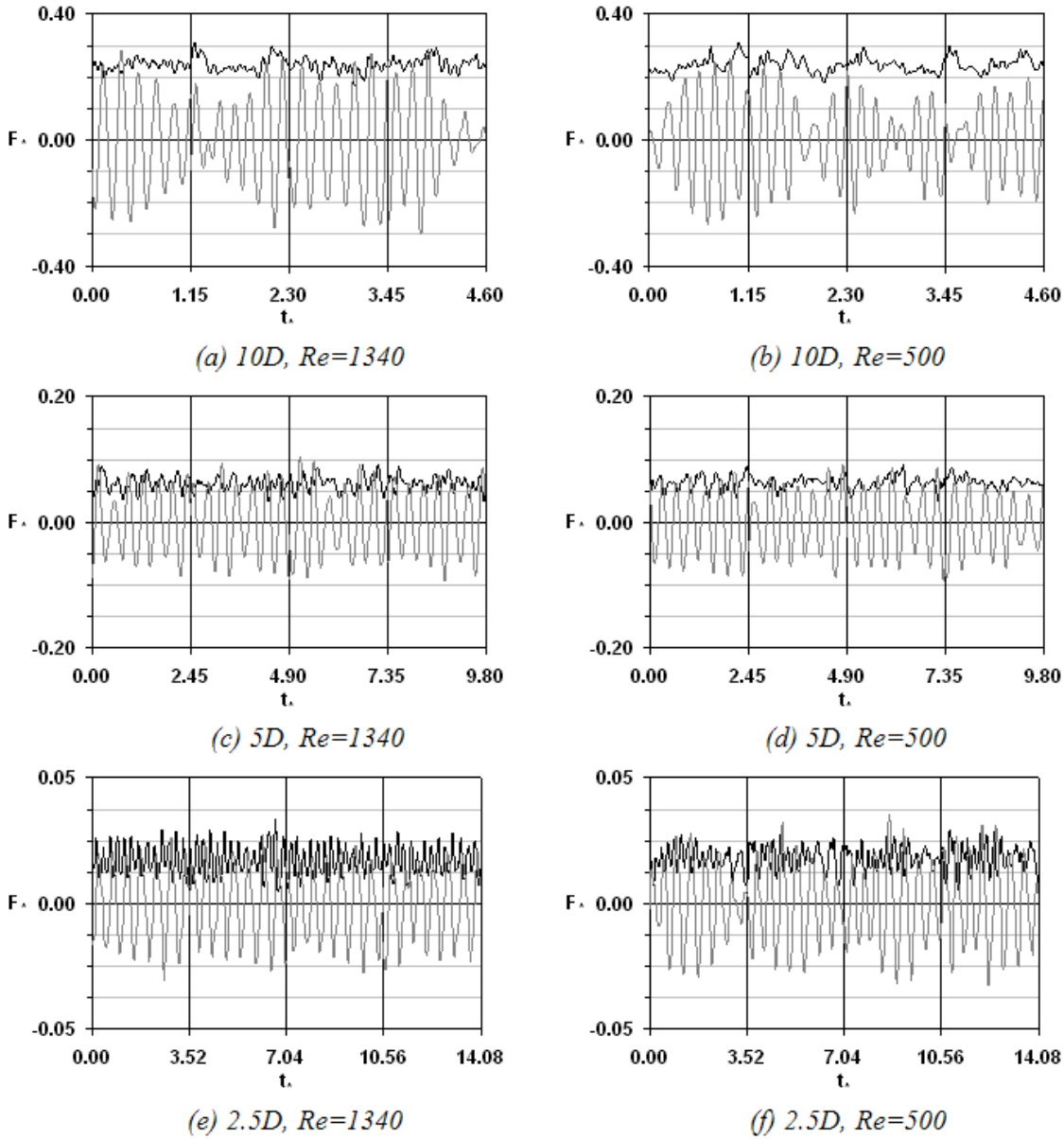

Figure 19: Temporal distribution of lift (grey line) and drag (black line) forces for the three vegetation densities and the two Re_D numbers

2.5D case however suggests that there is a dependency of S_t on the cylinder Reynolds number at higher vegetation densities as the Strouhal numbers decrease with an increase in Re_D. This is again in agreement with the observations of Lam and Lo [18].

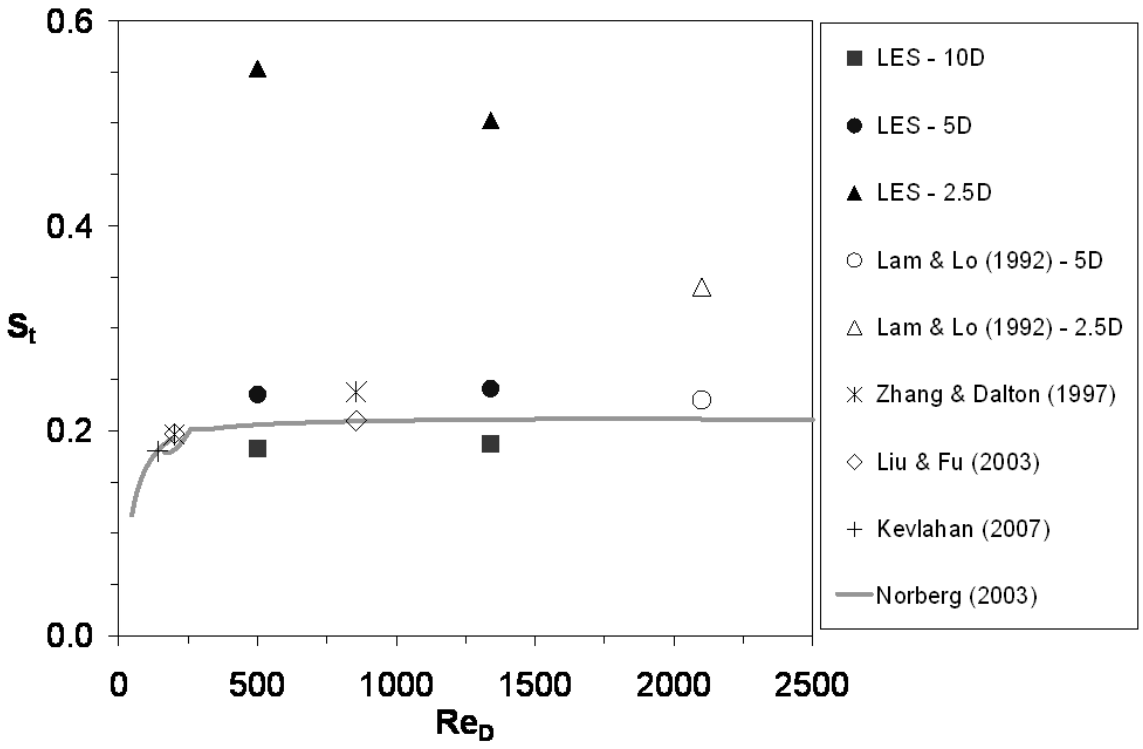

Figure 20: Strouhal number as a function of cylinder Reynolds number for the LES performed in this study versus isolated cylinder and tube bundle flow

2.6 Conclusions

Several large-eddy simulations of flow through a matrix of regularly arranged emergent cylinder were performed. For a low vegetation density, experimental data obtained from Liu et al. [20] were used to validate the first LES. Good agreement was found between measured and simulated data confirming the great accuracy of the LES method. Further simulations at higher vegetation density and at a second, lower cylinder Reynolds number were carried out to study the effect of vegetation density and cylinder Reynolds number on the mean flow, the turbulence statistics, flow resistance and instantaneous flow field. At low vegetation density the flow behaves similar to the flow around an isolated cylinder, while there are significant structural differences at high cylinder density, which is reflected in the turbulence statistics as well as in the flow resistance. Calculated drag forces are in good agreement with experimental data and suggest that flow resistance increases with both density and cylinder Reynolds number. Visualized turbulence structures, velocity signal analysis as well as distributions of the drag and lift force over time confirm the structural changes in the flow.

CHAPTER III

CLOSURE MODELING AND LOW-RESOLUTION LARGE EDDY SIMULATIONS OF VEGETATION DRAG FOR DIVERSE ARRAYS OF EMERGENT VEGETATION

3.1 Introduction

Vegetation on banks or floodplains of rivers and streams significantly affects the horizontal and vertical velocity distributions as well as the turbulence statistics. Accurate quantification of the bulk effects of flow-vegetation interaction is a significant challenge in the field of open-channel hydraulics and is for instance of great importance for the design of flood protection or stream restoration schemes [54].

Over the last four decades, the tool of Computational Fluid Dynamics (CFD) has been developed and refined. CFD models are able to provide accurate flow predictions of many flows of practical hydraulic and/or hydrological interest. In general, the methods of DNS (Direct Numerical Simulation), LES (Large Eddy Simulation), and RANS (Reynolds-Averaged-Navier-Stokes) have evolved. LES lies between the extreme approaches of DNS, where all turbulent fluctuations are computed and no turbulence model is required, and steady RANS, where only the mean velocity field is computed and all the unsteady effects of turbulence are accounted for by a turbulence model. Nowadays, RANS is considered an computationally-efficient engineering tool, while DNS and LES are much more expensive and are mainly used in research. LES (and DNS) offer a substantial increase in accuracy over time-averaged approaches, particularly when large-scale turbulent structures dominate the flow (e.g., [41]).

In the mid 90's, various RANS models were developed to simulate the flow through vegetation and different turbulence models were employed to calculate the Reynolds

stresses that are a result of Reynolds averaging. RANS models are operated on relatively coarser grids and the additional form drag due to vegetation is accounted for through subgrid forces that are added to the momentum and turbulence model transport equations. This treatment should be referred to as vegetation closure model; RANS models offer reasonable accuracy in the prediction of the time-averaged flow field [2, 4, 9, 22, 25, 26, 27, 29, 62], but agreement with measured turbulence quantities is sometimes poor [4, 27]. This is mainly due to the fact that steady RANS models do not resolve flow-vegetation interaction. Vortex shedding and local velocity gradients are absent, hence RANS models require additional drag-related terms in the turbulence models' transport equations to account for vegetation related turbulence production and its dissipation. Drag force terms in the momentum and drag-related terms in the turbulence model transport equations, require *a-priori* estimates of the drag coefficient and additional empirical constants.

Most vegetation closure models use the drag force formula, i.e., $F_D = 0.5\rho u_0^2 A_P C_D$, with ρ being the density of the working fluid, u_0 the free stream velocity, A_P the projected area of the plant, and C_D the drag coefficient, which is an empirical parameter. In many experimental investigations of flow through vegetation the cylinder analogy is made use of, i.e., vegetation can be idealized as rigid circular cylinders. The calculation of vegetation drag is then straight forward and the only uncertainty is in the selection of C_D. However, even though many RANS based studies that used the drag force approach report a reasonably good match of predicted velocity profiles with observed ones, some inaccuracies have been found in the prediction of the head loss in the system. The main reason is that RANS models adopted a "universal" drag coefficient, C_D, without consideration of its variation as a function of vegetation density and stem Reynolds number [4]. For instance, Fischer-Antze et al. [9] modeled emergent floodplain vegetation in a compound channel and due to the lack of knowledge of C_D they assumed the drag coefficient to be $C_D = 1.0$, reasoning that it

is a valid value over a wide range of cylinder (stem) Reynolds numbers, Re_D for flow around an isolated cylinder. However, the drag coefficient in an array of cylinders may differ from the one of an isolated cylinder. In a recent laboratory study, Tanino and Nepf [58] demonstrated that the drag coefficient is a function of both vegetation density and stem Reynolds number and that it can deviate largely from unity.

One way of avoiding the C_D empiricism in numerical models is to resolve the vegetation explicitly through the numerical grid. This was recently done by Stoesser et al. [53, 50] who performed several LES of the flow through submerged and emergent vegetation (idealized by rigid cylinders). They imposed the no-slip boundary condition on all solid boundaries, including the surface of the cylinders. In that way, flow-vegetation interaction was explicitly calculated. The simulations were validated with laboratory data and fairly good agreement was found. After successful validation [50] quantified the drag force of each cylinder. They confirmed the findings of Tanino and Nepf [58], i.e., C_D depends on both stem Reynolds number and vegetation density, and provided evidence that this trend is valid at stem Reynolds numbers greater than those examined by Tanino and Nepf [58].

A summary of numerical simulations of flow through vegetation is given in Table 3, which includes the mention of the respective vegetation closure model and the authors' choice for the closure coefficient/parameters. Table 3 demonstrates that almost all numerical models to date employ the drag-force concept, which requires *a-priori* knowledge of the drag coefficient. C_D was selected either based on experiments (e.g., [22]) or it was calibrated to match experimental data (e.g., [67]) or it was set to a fixed value (e.g., $C_D = 1.0$ by [9]) due to lack of knowledge of the real value. The LES in Stoesser et al. [50, 53] does not employ a vegetation closure model but the vegetation is idealized as rigid cylinders and such a treatment is computationally very demanding. Hence, LES is limited to relatively simple (vegetation) geometries and relatively low stem Reynolds numbers due to its need for very fine grids.

The first objective of this study is to assess the importance of *a-priori* knowledge of the empirical drag coefficient in flow through emergent vegetation (in here idealized as cylinder matrices) when using RANS with a vegetation closure model. The second objective is to evaluate a low-resolution LES strategy that is able to simulate vegetation drag directly. Low-resolution LES does not rely on empirical parameters and is computationally cheaper than a fully resolved LES. Simulations are carried out for different numerical and physical experiments of uniform flow through emergent vegetation at varying vegetation density and stem Reynolds numbers.

Table 3: Formulations to characterize vegetation drag by different researchers

Study	Model approach/ Turbulence closure	Drag force closure (drag coefficients)	Parameter (coefficient) treatment
Tsujimoto and Shimizu [62]	$2D$ RANS $k-\epsilon$ model	Drag force terms to mom. eqs. (C_{dx}, C_{dz}) Drag force terms to turbulence energy eqs. (C_{fk}, $C_{f\epsilon}$)	no values provided for C_{dx}, C_{dz} $C_{fk} = 1.0$, $C_{f\epsilon} = 1.3$
Wu et al. [67]	$2D$ RANS $k-\epsilon$ model	Drag force terms to mom. eqs. (C_d) Drag force terms to turbulence energy eqs. (C_{vk}, $C_{\epsilon 3}$)	$C_d = 1.0 - 4.0$ $C_{vk} = 1.0$, $C_{\epsilon 3} = 1.33$
Naot et al. [25]	RANS $k-\epsilon$ model	Drag force terms to mom. eqs. (C_D) Drag force terms to turbulence energy eqs. (C_D)	$C_D = (10^3/Re_D)^{0.25}$ for $Re_D \leq 10^3$ or min. of $0.976 + [(10^{-3}Re_D - 2)/20.5]^2$ or 1.15 for $10^3 < Re_D < 4 \times 10^4$ [44]
Lopez and Garcia [22]	RANS $k-\epsilon$ and $k-\omega$ model	Drag force terms to mom. eqs. (C_D) Drag force terms to turbulence energy eqs. (C_{fk}, $C_{f\epsilon}$)	$C_D = 1.13$ [5] $C_{fk} = 1.0$, $C_{f\epsilon} = 1.33$
Fischer-Antze et al. [9]	RANS $k-\epsilon$ model	Drag force terms to mom. eqs. (C_D)	C_D is set as 1.0
Neary [27]	RANS $k-\omega$ model	Drag force terms to mom. eqs. (C_D) Drag force terms to turbulence energy eqs. (C_{fk}, $C_{f\omega}$)	$C_D = 1.13$ [22] for case 1 and $C_D = 1.0 - 1.5$ for case 2 $C_{fk} = 1.0$ [22], $C_{f\omega} = 1.5$ for case 1 and $C_{fk} = 0.05$, $C_{f\omega} = 0.16$ for case 2
Nicholas and McLelland [29]	RANS $k-\epsilon$ model	Drag force terms to mom. eqs. (C_D)	C_D is set as 1.0
Choi and Kang [2]	Reynolds stress model	Drag force terms to mom. eqs. (C_D)	$C_D = C_{DA} f(z, h_p)$, $C_{DA} = 1.13$ [5] with z =depth and h_p =vegetation height
Defina and Bixo [4]	RANS $k-\epsilon$ model	Drag force terms to mom. eqs. (C_D) Drag force terms to turbulence energy eqs. (C_{fk}, $C_{f\epsilon}$)	$C_D = 1.0 - 3.0$ $C_{fk} = 1.0$, $C_{f\epsilon} = 1.33$ [22] and $C_{fk} = 0.07$, $C_{f\epsilon} = 0.16$ [46]
Nadaoka and Yagi [24]	$2D$ LES	Drag force terms to $2D$ mom. eqs. (C_b) A drag force term to energy transport eq. (C_b)	$C_b = 2.49$ for [61]'s case and $C_b = 2.42$ for [13]'s case
Cui and Neary [3]	LES	Drag force terms to mom. eqs. (C_D)	$C_D = 1.6$
Stoesser et al. [50, 53]	LES	Explicit resolution of circular cylinders imposing the no-slip boundary condition	

3.2 Numerical Framework

The two numerical strategies to predict the hydrodynamics of turbulent flow through emergent vegetation evaluated in this study are (1) a RANS-based approach with a subgrid vegetation closure model and (2) a novel low-resolution large-eddy simulation (LES) approach.

3.2.1 Reynolds-Averaged Navier-Stokes-Based Approach

The RANS model, validated by Fischer-Antze et al. [9], is employed to calculate the time-averaged flow through emergent vegetation, which, in this study, is emulated by a matrix of cylinders. The program solves the RANS equations with the finite-volume approach on a structured, nonorthogonal grid. A second-order upwind scheme approximates the convective terms in the momentum equations, whereas diffusive terms are approximated with a central differencing scheme. The SIMPLE method (e.g., [35]) couples the pressure to the velocity field and the standard $k - \epsilon$ turbulence closure model evades the explicit calculation of the Reynolds Stresses appearing in the RANS formulation of the Navier Stokes equations. A force term is added to the right hand side of the momentum equations to account for the momentum loss due to vegetation. The implementation is described in detail by Fischer-Antze et al. [9]. While the channel bed is treated with a no-slip condition, at the spanwise boundaries and the rigid lid free surface boundary, a slip condition is applied. Periodic boundary conditions are used in the streamwise direction to induce a fully developed uniform flow.

3.2.2 Low-Resolution Large-Eddy Simulation Approach

The low-resolution LES is developed as an alternative to high-resolution LES to simulate flow through emergent vegetation but at lower computational cost. The low-resolution LES is based on the LES code Hydro3D [52]. The code solves the filtered Navier-Stokes equations with the finite volume method for incompressible fluid flow on Cartesian grids. Convective and diffusive fluxes are approximated with central differences of second order accuracy and time advancement is achieved by a third order, three step, explicit Runge-Kutta scheme. The Poisson equation for coupling the pressure to the velocity field is solved iteratively with the SIP method of Stone [56] after the third Runge-Kutta step to ensure a divergence free flow field. The subgrid-scale stresses appearing in the filtered Navier-Stokes equations are computed using the dynamic version [10] of the original Smagorinsky model [47]. The wall boundary is treated with a no-slip condition using wall functions and the water surface is fixed as a rigid lid and a slip condition is applied there. Periodic conditions are used at the streamwise and spanwise boundaries. To treat the vegetation, the low-resolution LES code uses a simplified immersed boundary method on a Cartesian grid, similar to the one introduced in Stoesser [49]. This is in contrast to the high-resolution LES in which each vegetative element is resolved explicitly with a body-fitted, curvilinear grid. The grids of both RANS and low-resolution LES are depicted in Figure 21.

Figure 22 illustrates the concept of the novel immersed boundary method applied herein to account for the rigid cylinders, which are immersed in the low-resolution LES grid. In a preprocessing step, three types of computational cells around a circular obstacle are identified in the Cartesian grid, i.e., fluid cells, cut cells, and inside cells. The fluid volume fraction, V_f, which is defined as the ratio of the volume of fluid to the total volume of a cell, is computed for each cell. Fluid cells with $V_f = 1.0$ do not require any treatment, while inside cells (i.e., $V_f = 0.0$) are blocked out of the computation so that $u_i = 0.0$. The velocity in the cut cells, u_i, is updated after the third and

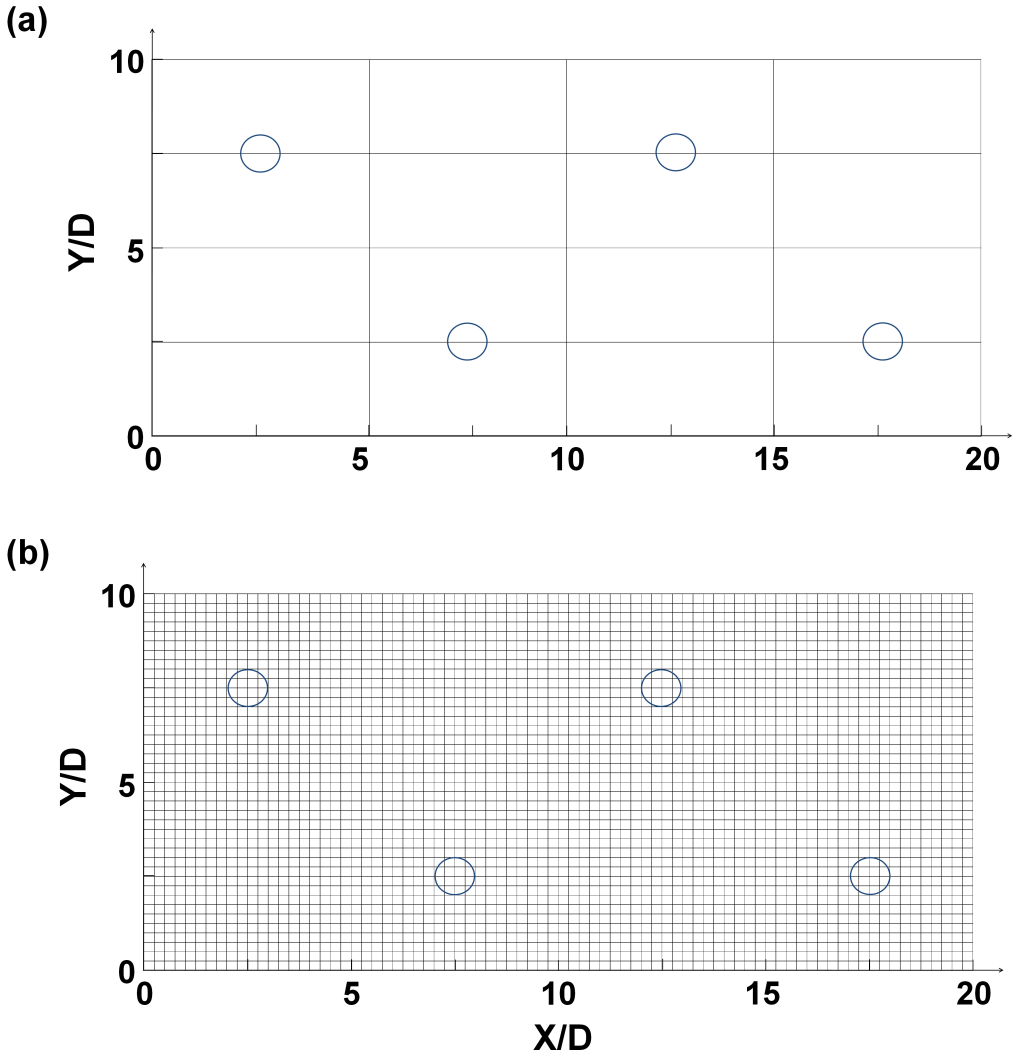

Figure 21: Coarsest numerical grid of the (a) RANS simulations and (b) low-resolution LES for the $\phi = 0.016$ case

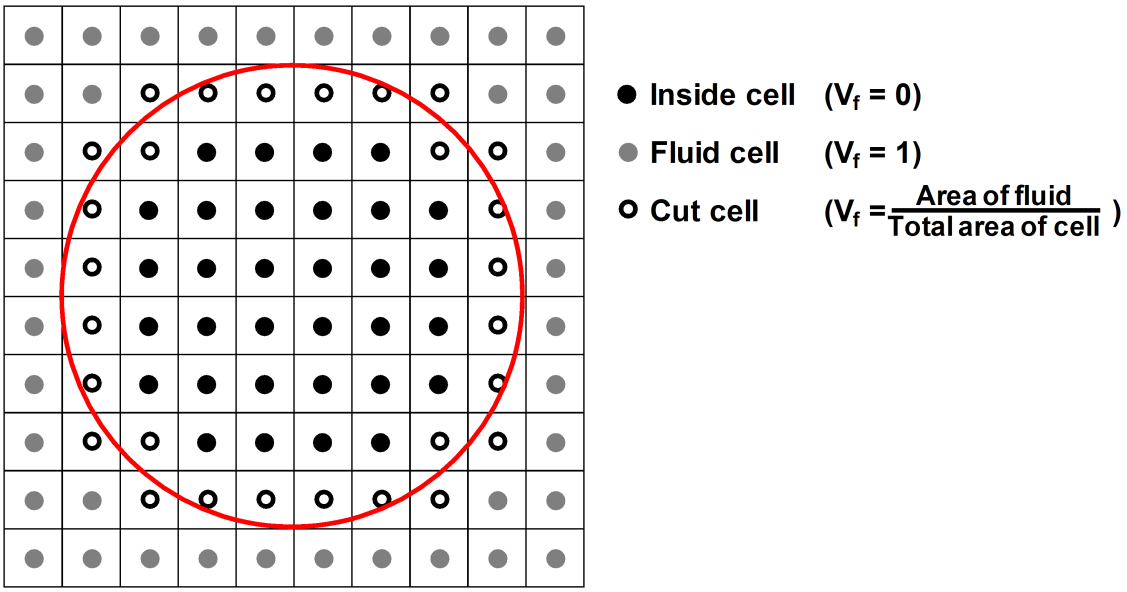

Figure 22: Concept of immersed boundary method of low-resolution LES on Cartesian grids

final Runge Kutta step by multiplying the value from the previous Runge Kutta step with the volume fraction V_f. Before moving to the next time step a divergence-free flow field is ensured by solution of a Poisson equation for the pressure followed by final update of the velocity field in the fluid cells. The proposed immersed boundary method should be considered first order accurate but is stable and oscillation free, because the gradients at the fluid-cylinder interface are somewhat smeared out. The use of a Cartesian grid together with the immersed boundary method is advantageous in two ways. First of all, solvers for Cartesian grids are more efficient than for body-fitted, curvilinear grids. Secondly, the immersed boundary method allows for very complex vegetation arrangements, e.g., random distribution of vegetation stems, in which stems can be placed very close to each other. For such scenarios body-fitted grids are inappropriate or even impossible.

3.3 Test Cases

In order to test and validate the RANS and low-resolution LES approaches, data of the laboratory experiments conducted by Tanino and Nepf [58] and high-resolution LES simulations of Stoesser et al. [50] are used. The high-resolution LES of Stoesser et al. [50] resolved the individual cylinders directly through extremely fine grids, and the results were thoroughly validated and are considered experiments for the purpose of this study. Also, supplementary laboratory experiments were carried out in the hydraulics laboratory at Georgia Tech for additional vegetation densities and stem Reynolds numbers. Overall, seven different vegetation densities, ϕ, are investigated, with ϕ defined as follows:

$$\phi = m\pi\frac{D^2}{4} \tag{3}$$

, in which m is the number of stems per unit area and D is the stem diameter.

In addition to the vegetation density, different stem Reynolds numbers, Re_D, are investigated. Re_D is defined as:

$$Re_D = \frac{u_{bulk}D}{\nu} \tag{4}$$

, in which u_{bulk} is the bulk fluid velocity, i.e., discharge divided by the flow area, and ν is the kinematic viscosity of the working fluid. Specific information of the experimental cases is provided in the following sections and an overview is given in Table 4.

Table 4: Summary of experimental cases in present study and predicted bulk drag coefficients from low-resolution LES

		Experimental cases					Low-resolution LES	
Study	Stem array	ϕ	Re_D	H/D	C_D	C_D (cylinder only)	C_D	Percent error
Stoesser et al. [50]	Staggered	0.016	500	10.22	1.28	1.17	1.23	3.8
		0.016	1340	10.22	1.31	1.23	1.06	18.9
		0.063	125	10.22	2.05	1.96	1.79	12.8
		0.063	250	10.22	1.88	1.82	1.62	14.1
		0.063	500	10.22	1.79	1.75	1.55	13.8
		0.063	1340	10.22	1.72	1.68	1.53	10.7
		0.251	500	10.22	3.48	3.46	3.84	10.1
		0.251	1340	10.22	3.21	3.19	3.86	20.4
Georgia Tech, 2010	Staggered	0.022	1700	13.4	1.43	-	1.16	18.9
		0.087	695	16.5	2.02	-	1.90	5.8
Tanino and Nepf [58]	Randomly	0.091	170	24.62	2.14	-	-	-
		0.091	500	15-34	1.35-2.09	-	2.00	-
		0.091	1340	15-34	1.32-2.00	-	1.95	-
		0.150	193	20.89	3.03	-	-	-
		0.150	263	21.38	2.86	-	-	-
		0.150	363	22.69	2.72	-	-	-
		0.150	500	15-34	1.96-2.83	-	2.49	-
		0.150	1340	15-34	1.78-2.59	-	2.44	-

3.3.1 Numerical Simulations by Stoesser et al. [50]

The high-resolution LES were performed in analogy to the experimental investigations undertaken by Liu et al. [20]. They placed a matrix of rigid cylinders in a staggered arrangement into a rectangular flume and carried out detailed LDA measurements. The distance between neighboring cylinders in both streamwise and spanwise directions is $s = 10D$ ($\phi = 0.016$). The Reynolds number based on the bulk velocity, u_{bulk} and the cylinder diameter $D = 0.00635$ m, Re_D, is approximately 1340. The validation of the high-resolution LES is described in detail by Stoesser et al. [50]. They reported that their high-resolution LES reproduced the experiments quite accurately in terms of first and second order statistics. After successful validation of this case, Stoesser et al. [50] expanded the parameter range by performing simulations for two additional vegetation densities, $\phi = 0.063$ ($s = 5D$) and $\phi = 0.251$ ($s = 2.5D$), and for additional stem Reynolds numbers, $Re_D = 500$, 250, and 125 for some cases. In total, eight high-resolution LES cases are available for comparison with RANS and low-resolution LES. Figure 23(a) depicts the numerical setup of the high-resolution LES and the grid resolution of each high-resolution simulation is detailed in Table 5.

3.3.2 Laboratory Experiments by Tanino and Nepf [58]

The laboratory experiments by Tanino and Nepf [58] investigated the drag exerted by randomly distributed, rigid, emergent, circular cylinders of uniform diameter on the flow. The authors covered the following vegetation densities ($\phi = 0.091$, 0.15, 0.20, 0.27, and 0.35) and a fairly wide range of stem Reynolds numbers, $Re_D = 25 - 685$. They provide the bulk drag coefficient in an equation form (i.e., Eq. (5) in their paper), which is used herein to attain the corresponding drag coefficients. In the numerical study presented here, two densities, i.e., $\phi = 0.091$ and 0.15 are selected for RANS and low-resolution LES evaluation. In addition, one additional flow with

Table 5: Grid resolution of the present simulations and for comparison of the high-resolution LES of Stoesser et al. [50]

Cases		Total number of gridpoints		
ϕ	Re_D	High-resolution LES	RANS	Low-resolution LES
0.016	500	7,564,000	275	534,681
	1340	11,604,640	275	534,681
0.063	125	12,297,600	275	534,681
	250	12,297,600	275	534,681
	500	12,297,600	275	534,681
	1340	22,994,560	275	534,681
0.251	500	9,963,008	891	534,681
	1340	29,514,240	891	534,681

$Re_D = 1340$ is tested for both densities with the assumption that the relationship provided by Tanino and Nepf can be extrapolated to higher stem Reynolds numbers, i.e., $Re_D > 685$. The numerical setup of these laboratory experiments utilizes MATLAB's (The MathWorks, Inc.) random number generator, with which the distribution of the cylinders is determined for the two densities (e.g., $\phi = 0.15$ in Figure 23(b)).

3.3.3 Supplementary Laboratory Experiments at Georgia Tech

Additional experiments were conducted in the Georgia Tech hydraulic laboratory in a 8 m long, 0.99 m wide, 0.4 m deep flume that has a fixed bottom slope of $S_0 = 0.006$ (Figure 23(c)). Two different vegetation densities, $\phi = 0.022$ ($s = 8.5D$) and $\phi = 0.087$ ($s = 4.25D$) were emulated using thin, wooden dowels of diameter $D = 0.01$ m, which were arranged in a staggered fashion. The dowels covered a length of 4.88 m of the flume, whereas the exit and entrance section featured coarse gravel to obtain a smoother flow transition into and out of the vegetation section. Different flow scenarios were investigated, mainly to determine the uniform flow depth for seven different discharges at two different vegetation densities, i.e., $\phi = 0.022$ and

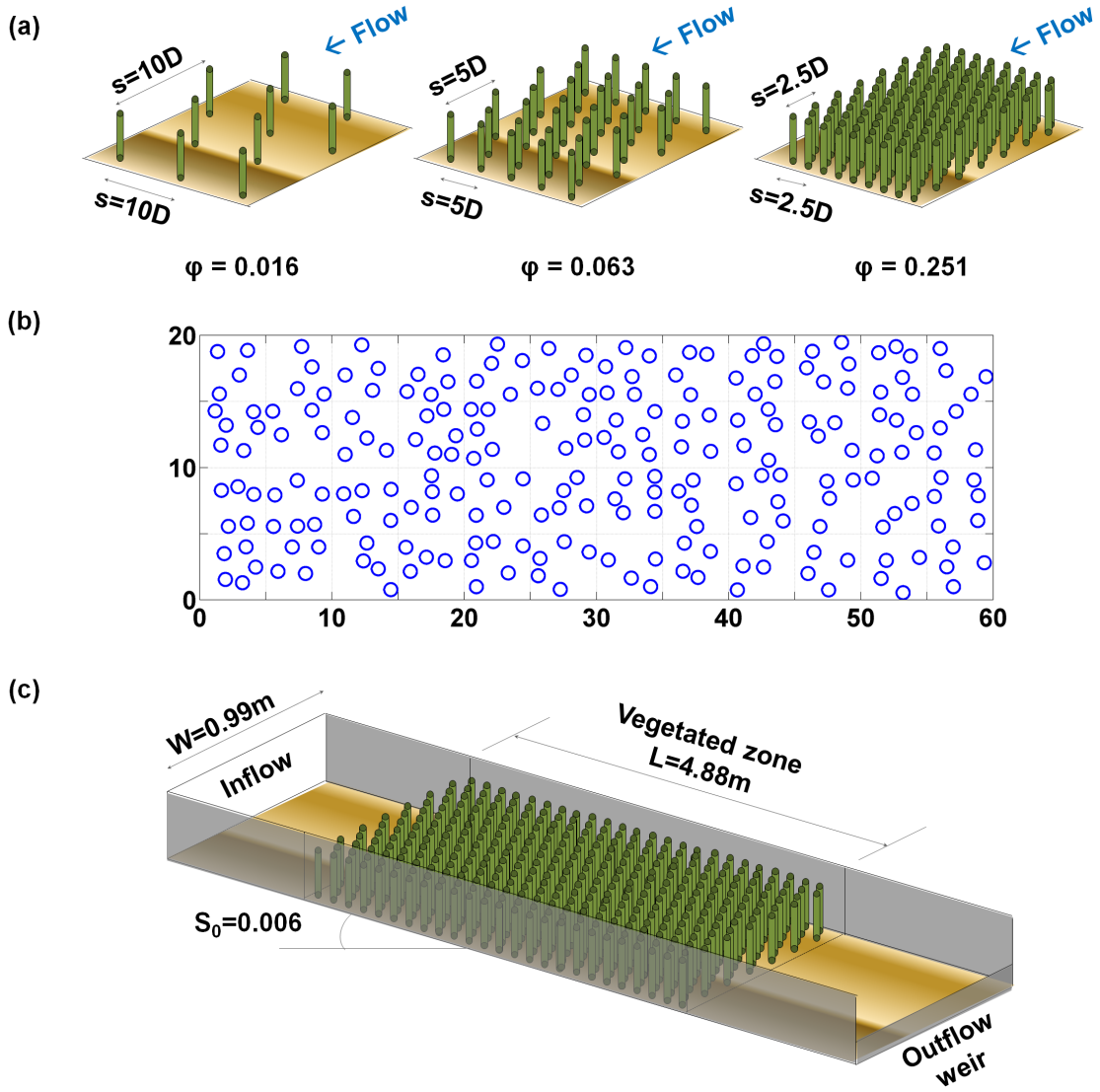

Figure 23: Setup of test cases used in this study; (a) high-resolution LES of Stoesser et al. [50], (b) sketch of experiments by Tanino and Nepf [58], and (c) experiments at Georgia Tech

$\phi = 0.087$. Water surface profiles were measured with a point gage along the centerline of the flume at intervals of 0.3 m. The precision of the point gage was 1/10 mm. A flexible tailgate allowed for setting different downstream water depths. The uniform flow depth was found from the intersect of M1 and M2 water surface profiles for the same discharge. A regression analysis of the measured data was used to determine the slope of the two profiles. Once the uniform flow depth was determined, the tailgate was adjusted accordingly and flow uniformity was confirmed by repeating the water surface profile measurements. The stem Reynolds number based on dowel diameter, Re_D varied between 1675 to 1750 and from 600 to 695 for the $\phi = 0.022$ and $\phi = 0.087$ cases, respectively. Two flows for each vegetation density were selected to supplement the high-resolution LES and the experimental data of Tanino and Nepf [58].

3.4 Results and Discussion

3.4.1 The Effect of Re_D and ϕ on the Bulk Drag Coefficients

The selected experiments (and simulations) are analyzed first for the bulk drag coefficient, C_D in particular for the effect of stem Reynolds number and vegetation density. This is summarized in Table 4. The bulk drag coefficient of the laboratory experiments conducted at Georgia Tech, C_D, is computed by equaling the integral shear force as a result of gravity, F_g and the sum of the drag forces exerted by the emergent vegetation, F_D,

$$F_g = F_D \tag{5}$$

$$\rho g H S_0 = M \frac{1}{2} \rho C_D H D u_{bulk}^2 \tag{6}$$

$$C_D = \frac{g S_0}{M \frac{1}{2} D u_{bulk}^2} \tag{7}$$

, in which g is the acceleration due to gravity ($= 9.81 m/s^2$), S_0 is the bottom slope of the channel, and M is the total number of individual stems in the measurement section.

In this formulation, the channel bottom and channel side-wall friction is assumed to be negligibly small, which is a common assumption [8, 17, 58]. An advantage of including the high-resolution LES as additional experiments is that this assumption can be proven directly, because Stoesser et al. [50] have provided the contributions of cylinder drag and bed shear drag to the total flow resistance. The effect of bed friction on the bulk drag will be discussed later.

The dependence of the bulk drag coefficient on Re_D and ϕ are shown in Figure 24. Darker symbols represent denser vegetation. The symbol shape varies according to the data source, i.e., diamonds represent the data of Stoesser et al. [50], circles represent the data of Tanino and Nepf [58], and triangles represent the data of the additional experiments carried out at Georgia Tech. From Figure 24(a) it is apparent that C_D is a function of both Re_D and ϕ. The effect of stem Reynolds number is less significant than the effect of vegetation density, which is better illustrated in Figure 24(b). In Figure 24(b) a decrease in stem Reynolds number is indicated by solid arrows. At low vegetation density the effect of Reynolds number disappears, which is consistent with experiments of flow around an isolated cylinder. The C_D-values obtained from the laboratory experiments carried out as part of this study are consistent with and complement previous observations [8, 17, 58]. Noteworthy is the fact that the vegetation arrangement, i.e., staggered vs. random, does not seem to affect the value of the bulk drag coefficient. This is easily observable when comparing the drag coefficient obtained by Tanino and Nepf, i.e., gray circles, with the C_D found from the Georgia Tech experiments (i.e., gray triangles). Both experiments featured a vegetation density of $\phi \approx 0.09$.

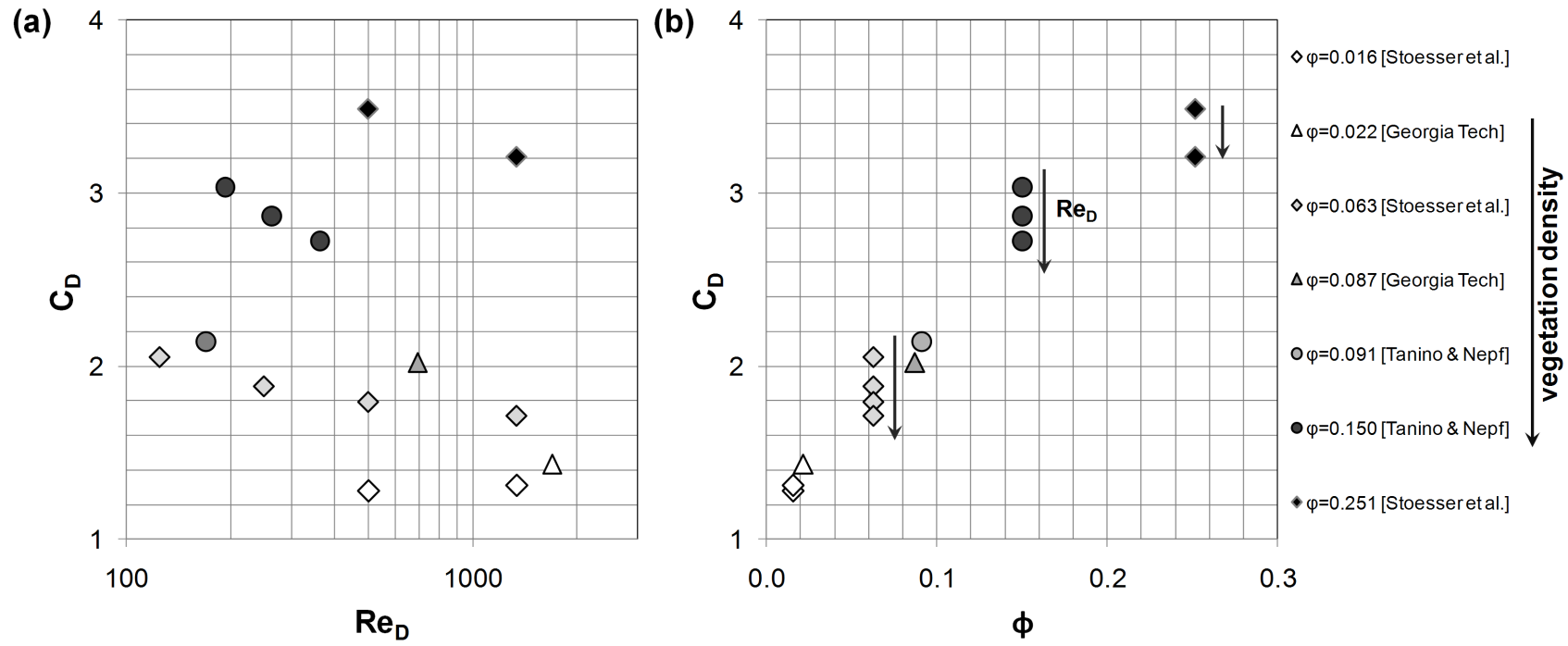

Figure 24: The effect of (a) Re_D and (b) ϕ on the bulk drag coefficient

3.4.2 The Importance of *a-Priori* Knowledge of Drag Coefficients on Flow Resistance Predictions Using RANS

As mentioned above, RANS models employ a vegetation closure model that includes an empirical coefficient, i.e., the bulk drag coefficient. In this study, two sets of RANS simulations are performed to investigate the importance of *a-priori* knowledge of the drag coefficient and to quantify its influence on the headloss in the system; the first set of simulations uses known drag coefficients (from the corresponding experiment or from the formula to calculate C_D suggested by Tanino and Nepf [58], and the other set of simulations uses an assumed drag coefficient of unity (commonly used when there is lack of knowledge of the exact C_D). For the quantification of flow resistance, the normalized global bed shear stress, i.e., $\tau_0/(u_{bulk}^2\rho)$ is used. The value obtained from RANS simulation (τ_0 calculated as $\tau_0 = dp/dx \cdot H$ of each available experiment) is then compared with the one measured (τ_0 calculated as $\tau_0 = \rho \cdot g \cdot H \cdot S_0$). Figure 25(a) compares the first set of RANS simulations using known bulk drag coefficients with experimental values and the data almost collapses on the 45 degree line that indicates a perfect match. For the densest vegetation case, i.e., $\phi = 0.251$, RANS slightly underestimates the flow resistance, though the exact cylinder drag coefficient was provided from the high-resolution LES. This should be attributed to the fact that in RANS strong streamwise and spanwise velocity gradients that are prevailing in the flow with the highest vegetation density are not reproduced.

The RANS simulations using a constant bulk drag coefficient of $C_D = 1.0$ generally underestimate the flow resistance (Figure 25(b)). The underestimation of flow resistance is more severe with increasing vegetation density and the maximum error is found to be almost 78 % for the cases with $\phi = 0.251$. However, the lower density cases exhibit better agreement, especially in the cases of $\phi = 0.016$ and $\phi = 0.022$. This is owing to the fact that the flow through vegetation at low vegetation density is similar to the flow around an isolated cylinder [50], in which the drag coefficient

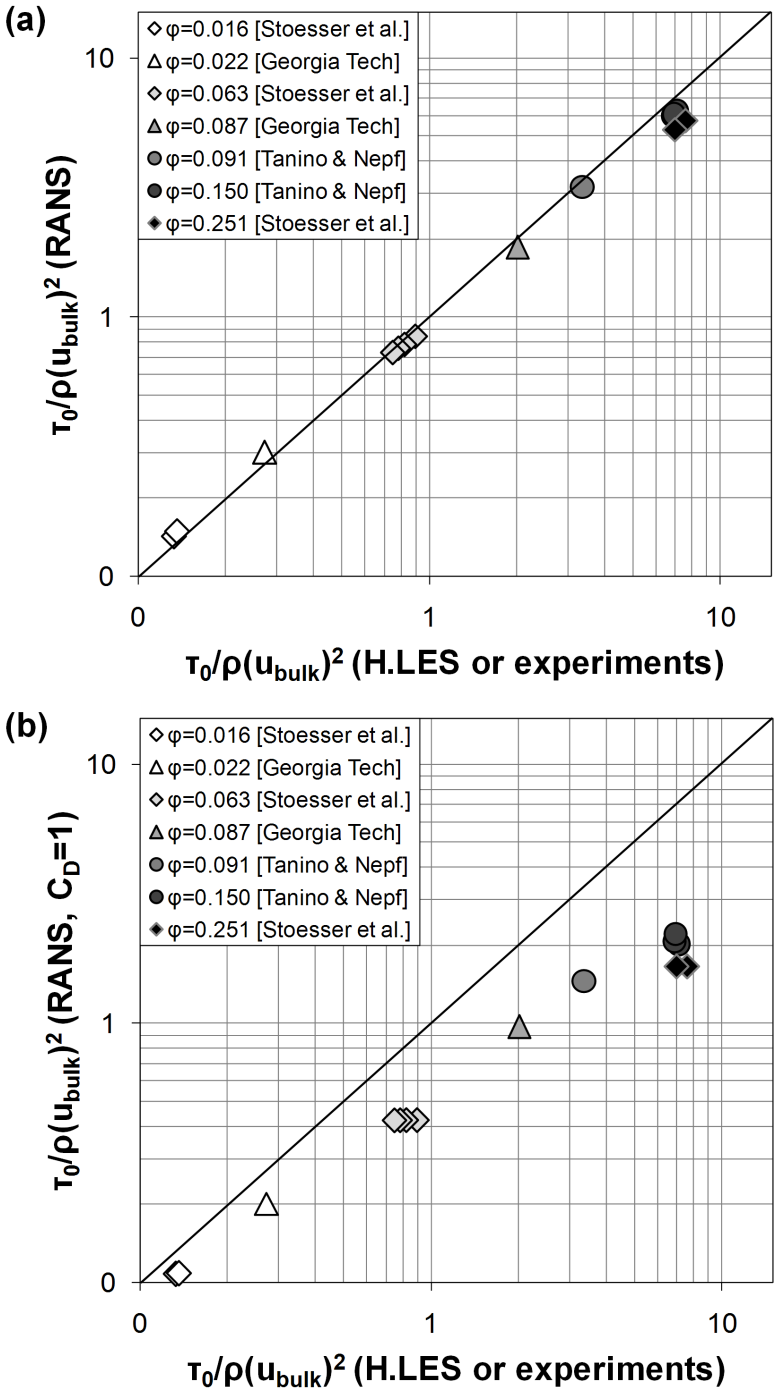

Figure 25: Predictions of global shear stress using RANS using (a) *a-priori* known C_D and (b) $C_D = 1.0$

converges to unity over a wide range of stem Reynolds numbers.

Overall, *a-priori* knowledge of the bulk drag coefficient is found to be important when employing a vegetation closure model in RANS simulations. This study shows that if a drag coefficient of unity were used for simulations of the flow through emergent vegetation, the headloss in the system would be significantly underpredicted especially at high vegetation density or low stem Reynolds numbers, respectively.

3.4.3 The Contribution of Bed Friction

When determining the bulk drag coefficient from experiments, the bed friction is assumed to be negligibly small. Hence, so determined C_D-values theoretically include both vegetation drag and bed friction. What follows is that a RANS simulation that uses an experimentally determined bulk drag coefficient accounts for the bed friction twice and tends to overestimate the global bed shear stress, τ_0. In the high-resolution LES of Stoesser et al. [50] the percentage contribution of bed friction to the overall drag was calculated directly from the high-resolution data. Figure 26(a) illustrates the contribution of bed friction as a function of vegetation density and stem Reynolds number. The LES data are regressed for each available stem Reynolds number using a power law. For both data sets the squared regression coefficient is $R^2 = 0.9998$. As with the bulk drag coefficient, the bed friction shows a greater dependency on the vegetation density than on the stem Reynolds number, and its contribution increases exponentially for vegetation densities less than 0.1. This information is used to correct the bulk drag coefficient obtained from the experiments and a third set of RANS simulations is carried out, but only for the physical experiments. Figure 26(b) presents the results of the third set of RANS simulations, again comparing directly the simulated global shear stress with the measured one. It is seen that the already good match is not necessarily improved further. Only minimal improvements are

observed for the low density experiment (white triangle), and for higher vegetation density flows of Tanino and Nepf [58] the difference is not noticeable. However, given the exponential increase in bed friction contribution at decreasing vegetation density, the assumption of negligible bed friction may be invalid for vegetation densities lower than the ones reported herein.

3.4.4 Evaluation of the Low-Resolution LES Approach

Above simulations have demonstrated the importance of *a-priori* knowledge of the bulk drag coefficient in RANS models that feature a common cylinder drag based vegetation closure. For uniform flow through emergent vegetation in which the vegetation covers the entire channel width, the relationships given by Tanino and Nepf [58] can be used to calculate the unknown C_D value. The so obtained C_D can then be plugged into a RANS vegetation closure to predict reliably the flow resistance because of emergent vegetation. Figure 27(a) compares the C_D's of the present study with the range of C_D's computed from Tanino and Nepf's equation. It appears that the measured C_D values are consistently at the higher end of the range of the C_Ds computed with Tanino and Nepf's equation. This could be attributed to the fact that Tanino and Nepf's experiments were carried out at gradually varying flow, while the data used herein stem from experiments and simulations under uniform flow conditions. Nevertheless, the so calculated C_D values match observed values under uniform flow conditions quite well, regardless of stem Reynolds number.

In practical flows, however, the vegetation may not be distributed uniformly over the entire channel width or length in question. For instance, vegetation on floodplains may grow in heterogeneous patches and the drag of individual plants may vary largely within the patch. For such engineering applications the high-resolution LES is unfeasible due to the high computational costs; hence, is not an alternative to RANS. A less

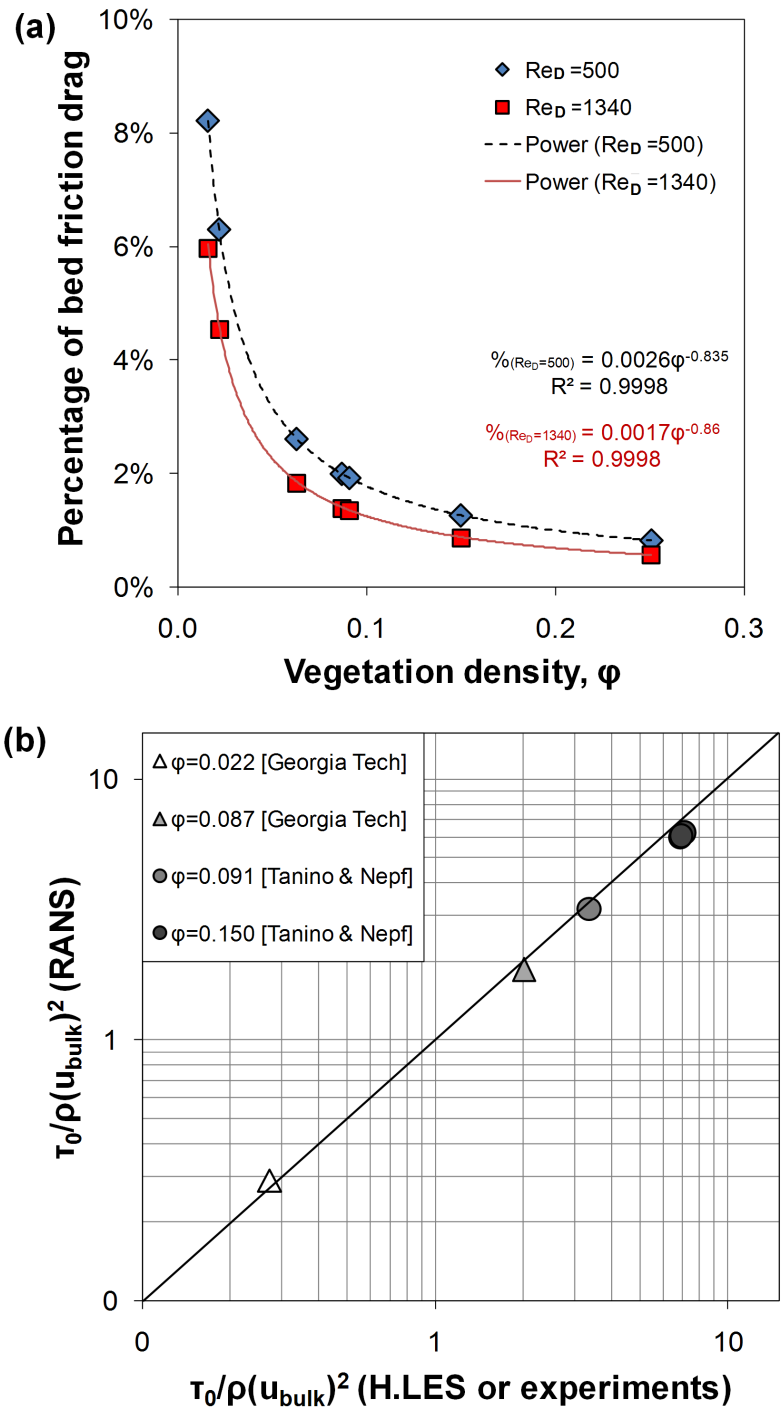

Figure 26: (a) Percentage of bed shear stress as a function of vegetation density and (b) comparison of global shear stress between experiments and RANS

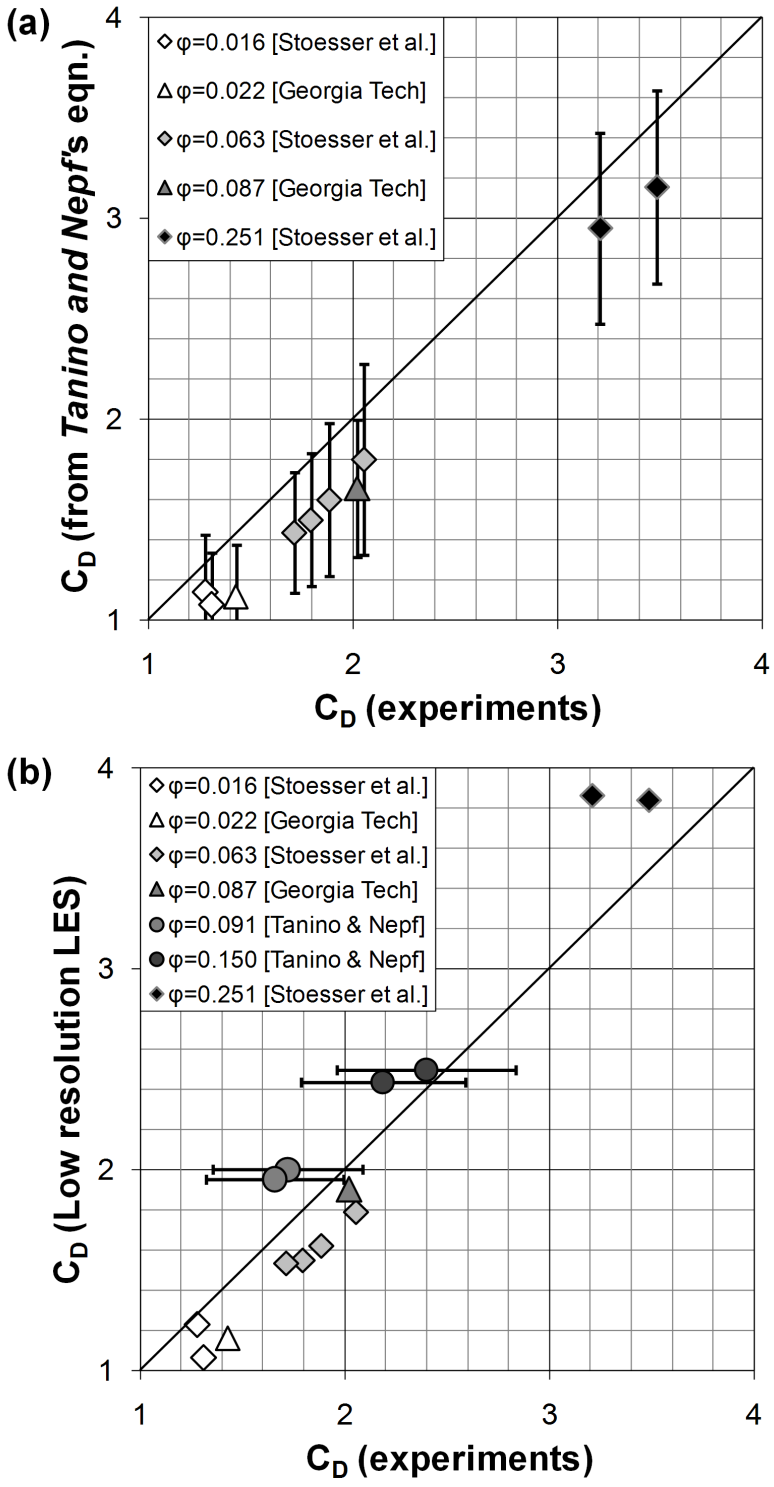

Figure 27: Comparison of drag coefficients from experiments with (a) C_D from Tanino and Nepf's equation and (b) C_D predicted by low-resolution LES

expensive, low-resolution LES may overcome the dependency on *a-priori* knowledge of C_D of RANS vegetation closures and at the same time decreases considerably the enormous computational effort of a fully resolved LES. The low-resolution LES of the present study are performed with a ten times finer grid (in each flow direction) than the RANS and with a 20 times coarser grid (in the horizontal) than the LES (see Table 5). If successful, the method of low-resolution LES could be used to provide drag coefficients for more complex vegetation arrangements.

The total drag in the low-resolution LES is calculated from the pressure gradient that drives the flow as $F_{D,total} = (dp/dx) \cdot Vol \cdot (1 - \phi)$. The drag coefficient is then computed from $C_D = 2F_{D,total}/(u_{bulk}^2 \cdot M \cdot H \cdot D)$. The following vegetation densities are considered, $\phi = 0.016, 0.022, 0.063, 0.087, 0.091, 0.150,$ and 0.251, and the predicted bulk drag coefficients are summarized in Table 4. A comparison of calculated C_Ds with the measured ones is plotted in Figure 27(b), showing an overall reasonably good agreement with the experimental cases except for the densest vegetation case with $\phi = 0.251$. The percentage error is in the range of $1 - 20\%$ (see also Table 4). It is obvious that the low-resolution LES generally underestimates the drag coefficient, in particular for the cases in which the vegetation is arranged in a regular (staggered) way. For the randomly arranged vegetation by Tanino and Nepf [58], the low-resolution LES predicts the bulk drag coefficient near the higher end of the range provided by Tanino and Nepf's equation. This suggests fairly good agreement (see discussion of Figure 27(a)). The $\phi = 0.251$ case of the high-resolution LES shows that the drag coefficient is overestimated, and for the higher stem Reynolds number the overestimation is about 20%. In the low-resolution LES approach the grid is too coarse to compute reliably the distribution of pressure on the cylidner, and a way of assessing the accuracy of the LES method is to investigate the size and strength of the recirculation behind each cylinder.

Figures 28 and 29 present contours of the streamwise velocity together with

streamlines for the case of $\phi = 0.087$ and $\phi = 0.251$ at half water depth (i.e., $Z/H = 0.5$) for both the high- and low- resolution LES. The results of the low-resolution LES for the $\phi = 0.087$ case reasonably match the high-resolution LES in terms of the velocity gradients (see top row of Figure 28) and in terms of the recirculation region (bottom row of Figure 28). The length of the recirculation zone is minimally shorter in the low-resolution LES of $\phi = 0.087$, leading to minimal underprediction of the drag coefficient (see Table 4). For the high density case, i.e., $\phi = 0.251$, the match is obviously not as good, and the velocity gradients (top row of Figure 29) as well as the size of the recirculation zone (bottom row of Figure 29) are predicted erroneously by the low-resolution LES (here overprediction of the length). Additionally, because very strong streamwise velocity gradients occur, the simulation suffers from numerical wiggles, which are a result of the central differencing scheme on a coarse grid. A more quantitative comparison of the time-averaged streamwise velocity is carried out by extracting profiles along two streamwise and spanwise lines (Figure 30(a) and (b), respectively, here only for the $\phi = 0.087$ case). The time-averaged velocity from both the high- and low- resolution LES exhibit a pretty good overall match. The low-resolution LES is able to reproduce both streamwise and spanwise velocity gradients quite accurately. The stagnation point and the recirculation region behind the cylinder are resolved adequately, and the mismatch in recirculation length is obvious from profile x1.

Figure 31 presents vertical profiles of the spatially-averaged streamwise velocity (normalized with the free stream velocity, u_0, i.e., the magnitude of the velocity in the spatially averaged velocity profile away from the bed) from the low-resolution LES, RANS, and, for comparison, high-resolution LES for three cases with $\phi = 0.016, 0.063,$ and 0.251 at $Re_D = 1340$ ((a) - (c)). It is remarkable that even though the RANS simulations are unable to capture all the details of the flow, the vertical velocity profiles of RANS match the spatially averaged velocity profile of the high-resolution

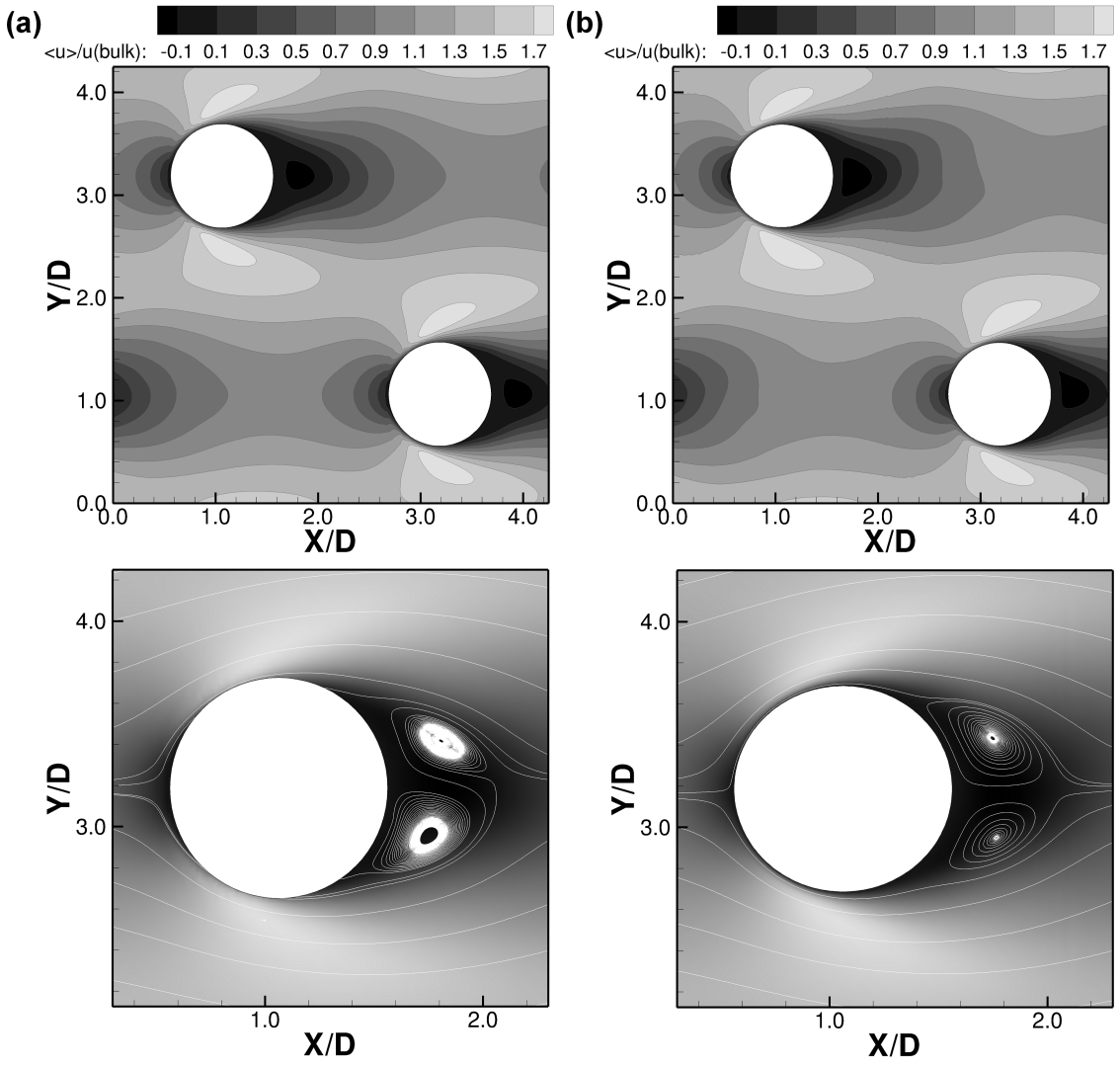

Figure 28: Contours of time-averaged velocity (top row) and streamlines around one cylinder (bottom row) of the $\phi = 0.087$ case simulated by (a) low-resolution LES and (b) high-resolution LES

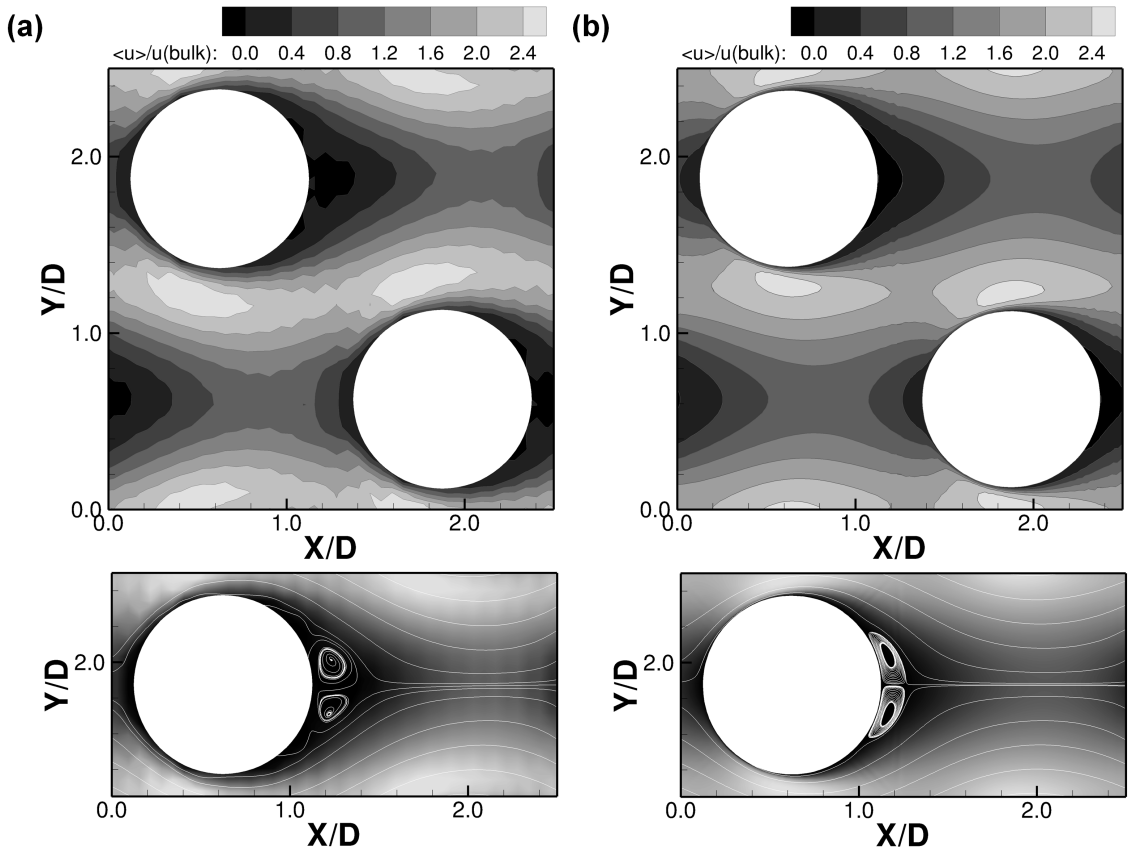

Figure 29: Contours of time-averaged velocity (top row) and streamlines around one cylinder (bottom row) of the $\phi = 0.251$ case and $Re_D = 1340$ ($Z/D = 5$) simulated by (a) low-resolution LES and (b) high-resolution LES

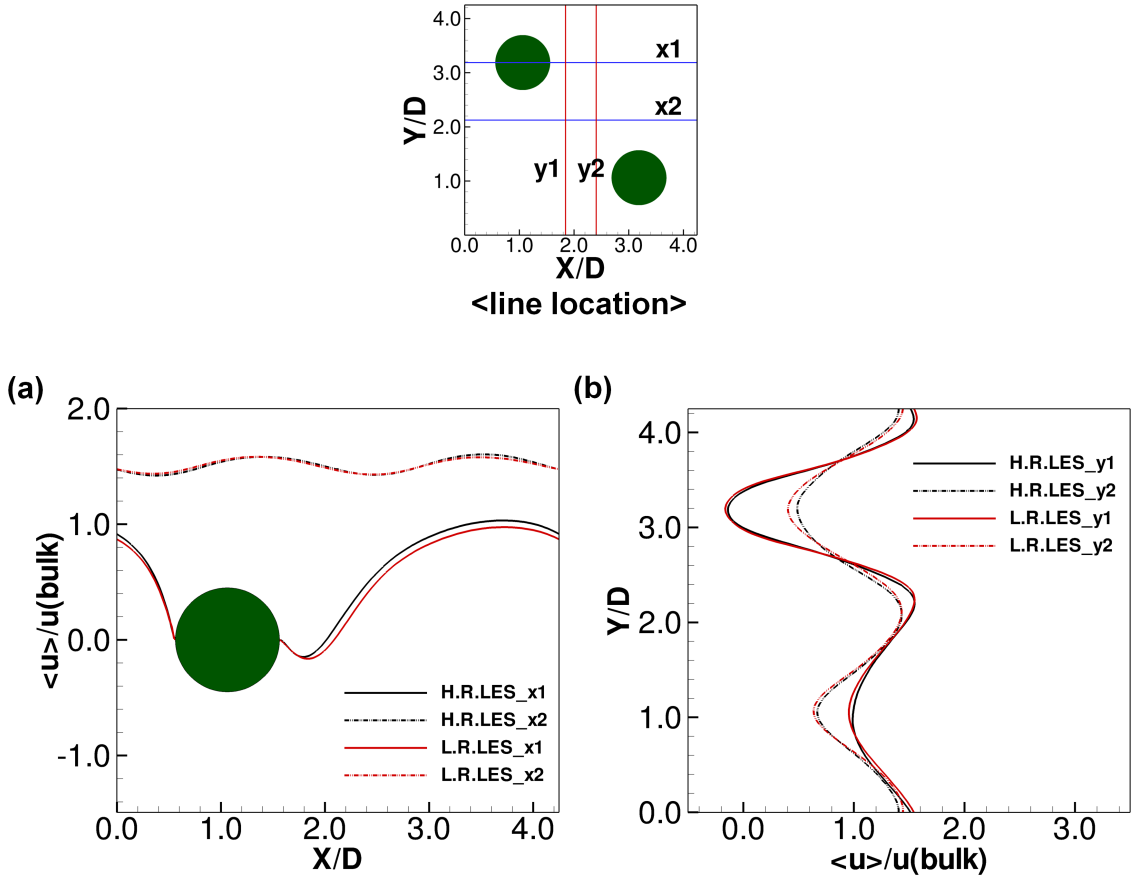

Figure 30: Profiles of time-averaged streamwise velocity from low-resolution and high-resolution LES along selected lines of the $\phi = 0.087$ case along (a) streamwise and (b) spanwise directions

LES quite well. This is true regardless of vegetation densities. Also, RANS is able to predict the decrease in bottom boundary layer thickness as vegetation density increases. However, the RANS simulated profiles show some deviations near the bed, where RANS computes a thicker boundary layer and is unable to predict the velocity bulge. Both features are a result of secondary currents (see [50]) that are transporting high-momentum flow to the channel bed, and since a RANS model that uses a drag force vegetation closure does not resolve the flow around individual cylinders it cannot predict such flow features. The low-resolution LES is able to resolve reasonably well velocity gradients, a wake behind the cylinder and secondary currents. As a result, the spatially averaged velocity profiles are in relatively good agreement with the high-resolution LES, including boundary layer thickness and velocity bulge.

A more detailed comparison of individual velocity profiles of low- and high-resolution LES is presented in Figure 32. This is done for the cases in which the low-resolution LES exhibits the best (i.e., $\phi = 0.016$) and the worst (i.e., $\phi = 0.251$) performance in terms of predicting the bulk drag coefficient. Five velocity profiles around the cylinders are selected, and their location in the flow is indicated in the included sketch. The comparison of the profiles confirm the statements made above, i.e., the existence of stream- and spanwise gradients, that are particularly large in the $\phi = 0.251$ case. For $\phi = 0.016$, all of the profiles predicted by low-resolution LES match the high-resolution LES quite well, except near the bed at location 1, which is very close to the cylinder. Here the lower grid resolution prevents a better match. The overall good match is reflected in the small discrepancy in bulk C_D. For the high vegetation density case, the match between low-resolution LES and high-resolution LES is quite poor along several profiles, in particular for profiles two and six. Apparently, the low-resolution LES is unable to accurately reproduce velocity gradients, clearly overestimates the recirculation zone (see vertical 6) and even produces a rather unphysical profile at vertical 2. Interestingly, the spatially averaged velocity profile

almost collapses onto the high-resolution LES profile (see Figure 31(c)). The rather large discrepancy in terms of the recirculation zone is directly reflected in the poor match of bulk drag coefficient.

Finally, the computational costs of the different simulation approaches should be discussed. The RANS simulations were run on very coarse grids and a fully converged simulation for steady state took less than a minute on a desktop computer. Both LES approaches are much more expensive in terms of computing time and demand sophisticated computer hardware. LES calculates the instantaneous flow and time-averaging requires sampling of each quantity at every time-step over a certain averaging period. For example, the physical simulation time for 10 flow throughs (i.e., the time a fluid element requires to be convected through the computational domain) of the $\phi = 0.016$ case took about 4600 and 140 CPU hours by high- and low- resolution LES, respectively. For the simulations reported herein, approx. 10 flow throughs are needed to develop the flow and another 30 flow throughs to collect reliable first order statistics. For the high-resolution LES a 96 processor Linux cluster was needed, while the low-resolution LES was carried out on a 4 processor Linux workstation.

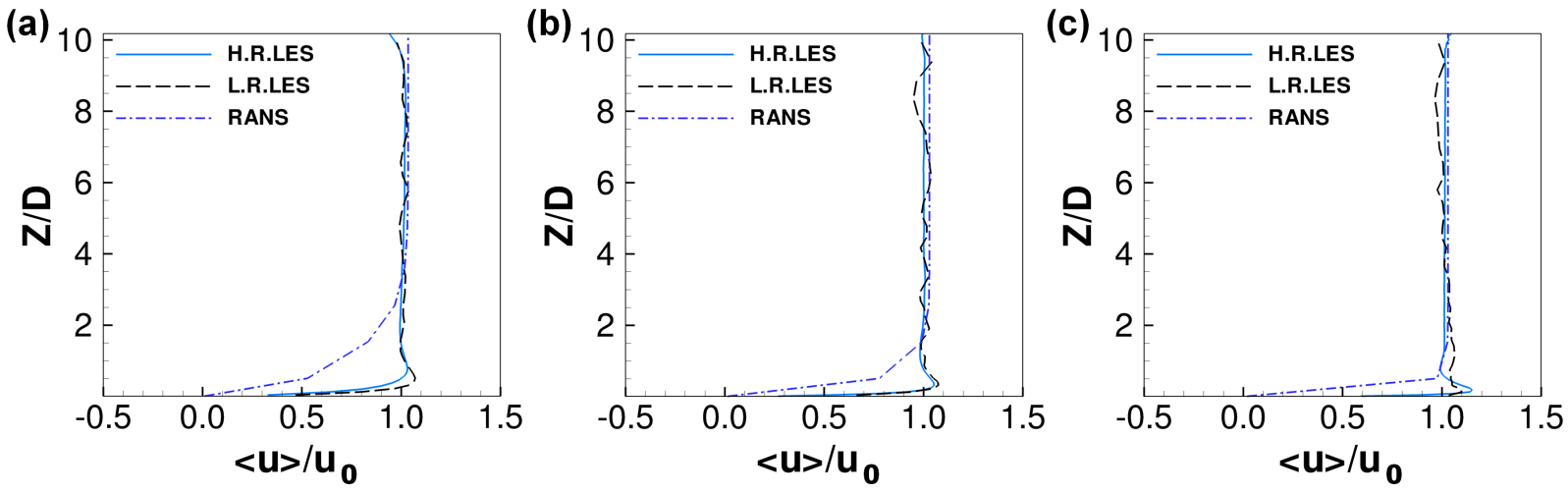

Figure 31: Vertical profiles of spatially-averaged streamwise velocity for (a) $\phi = 0.016$, (b) 0.063 and (c) 0.251 at $Re_D = 1340$

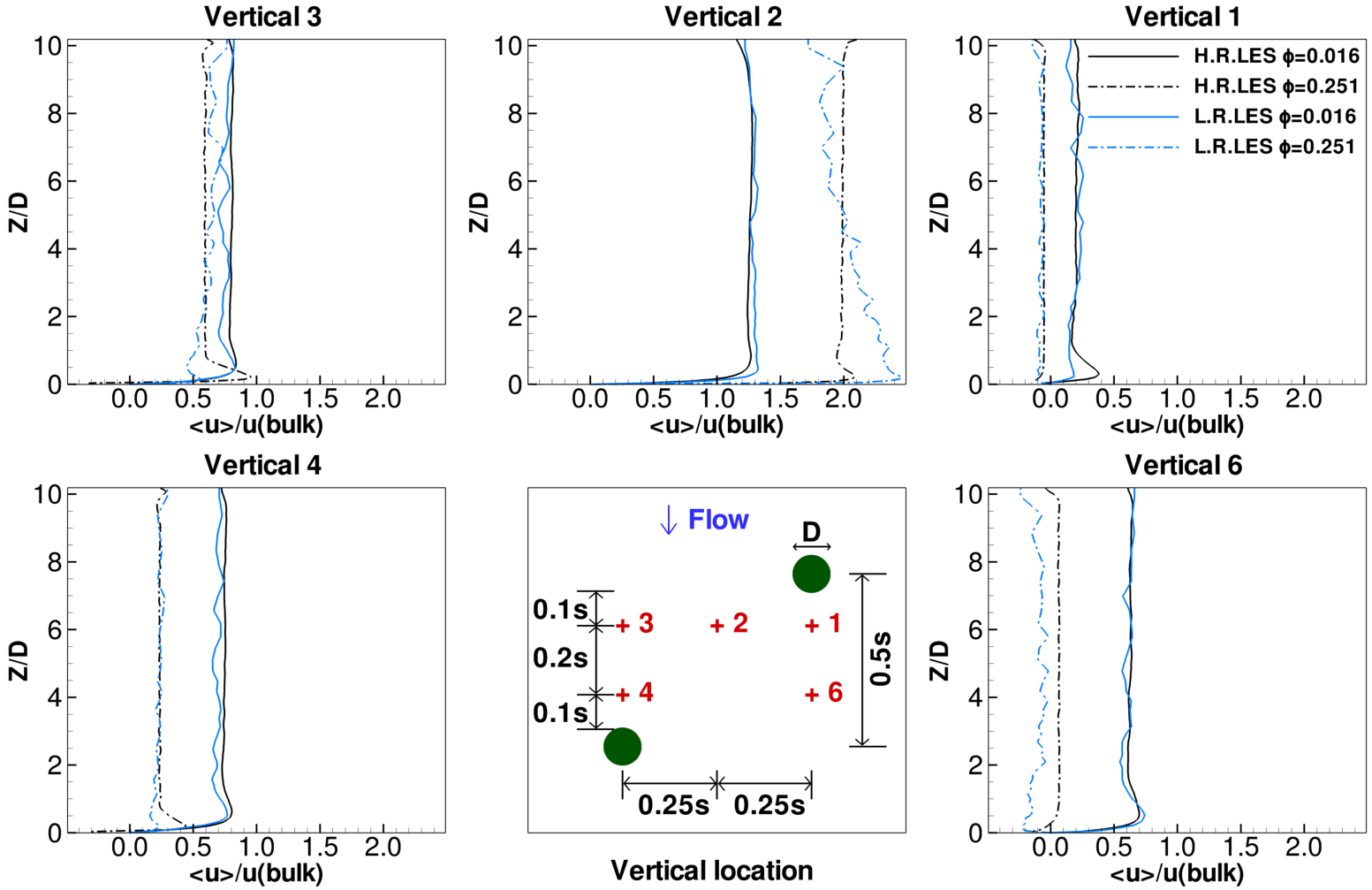

Figure 32: Time-averaged streamwise velocity profiles along five selected verticals for two densities of the $\phi = 0.016$ and 0.251 cases at $Re_D = 1340$ predicted by high- and low-resolution LES

Table 6: Grid sensitivity analysis of the low-resolution LES with $\phi = 0.016$ and $Re_D = 500$

Numerical strategy		Total number of gridpoints	Number of cells around a cylinder	C_D
High-resolution LES		7,564,000	240	1.28
Low-resolution LES	(a)	2,152,008	64	1.27
	(b)	551,368	32	1.23
	(c)	144,648	16	1.26

3.4.5 Grid Sensitivity Analysis of Low-Resolution LES

As was shown above, the low-resolution LES method appears to work fairly well, at least for lower vegetation densities. The number of grid points chosen for the low-resolution LES is based mainly on efficiency (with upscaling in mind) and not necessarily on near wall LES resolution requirements. Therefore, a grid sensitivity study is carried out for the case of $\phi = 0.016$ at $Re_D = 500$ in order to determine if the accuracy increases/decreases with an increase/decrease in grid resolution. Two more grids are generated, i.e., one grid (referred to as case (a) in the following) has a 4 times higher resolution than the original low resolution grid (in the following case (b)) while the other grid resolution (case (c)) has 4 times less grid points than the original low resolution grid (details are provided in Table 6). The number of grid points in the vertical is kept constant. The numbers of cut cells (see Figure 22) for the immersed boundary of one cylinder in a horizontal plane are 64, 32, and 16 for the cases (a), (b), and (c), respectively. The number of cut cells used in case (a) is still considerably less than the number of cells in the body-fitted, curvilinear grid of the high-resolution LES (i.e., 240) to resolve one cylinder. The results in terms of the bulk drag coefficient of the grid sensitivity study are also provided in Table 6. Even the lowest resolution LES is able to predict the drag coefficient fairly well.

For a comparison of the flow fields, horizontal distributions of the time-averaged

velocity at half water depth, i.e., $Z/D = 5$, of the low-resolution LES ((a) - (c)) are presented together with the result from the high-resolution LES (d) in Figure 33. Overall, the distribution of time-averaged streamwise velocity of all grid resolutions are in good agreement with the one predicted by the high-resolution LES. The recirculation zone behind the cylinder is fairly well predicted by the low-resolution LES with the finest grid, but with a decrease in grid resolution, the recirculation length increases. Interestingly, this increase is associated with a decrease in width of the wake behind the cylinder, which is why the bulk drag coefficients are not negatively affected. This is also reflected in the more quantitative comparison that is provided in Figure 34. The spatially-averaged vertical velocity profiles of (a) to (c) are in reasonably good agreement with the high-resolution LES profile regardless of the number of grid cells employed (see Figure 34(a)). Figure 34(b) plots the velocity profile along the centerline for one selected cylinder in the flow. The length of the recirculation zone as well as the velocity gradients are affected by the grid resolution. The coarser the grid, the less resolved the gradients, which results in a mismatch of recirculation zone. Not surprisingly, the best agreement is found with the highest grid resolution, the recirculation zone is overestimated in the simulation on the coarsest grid.

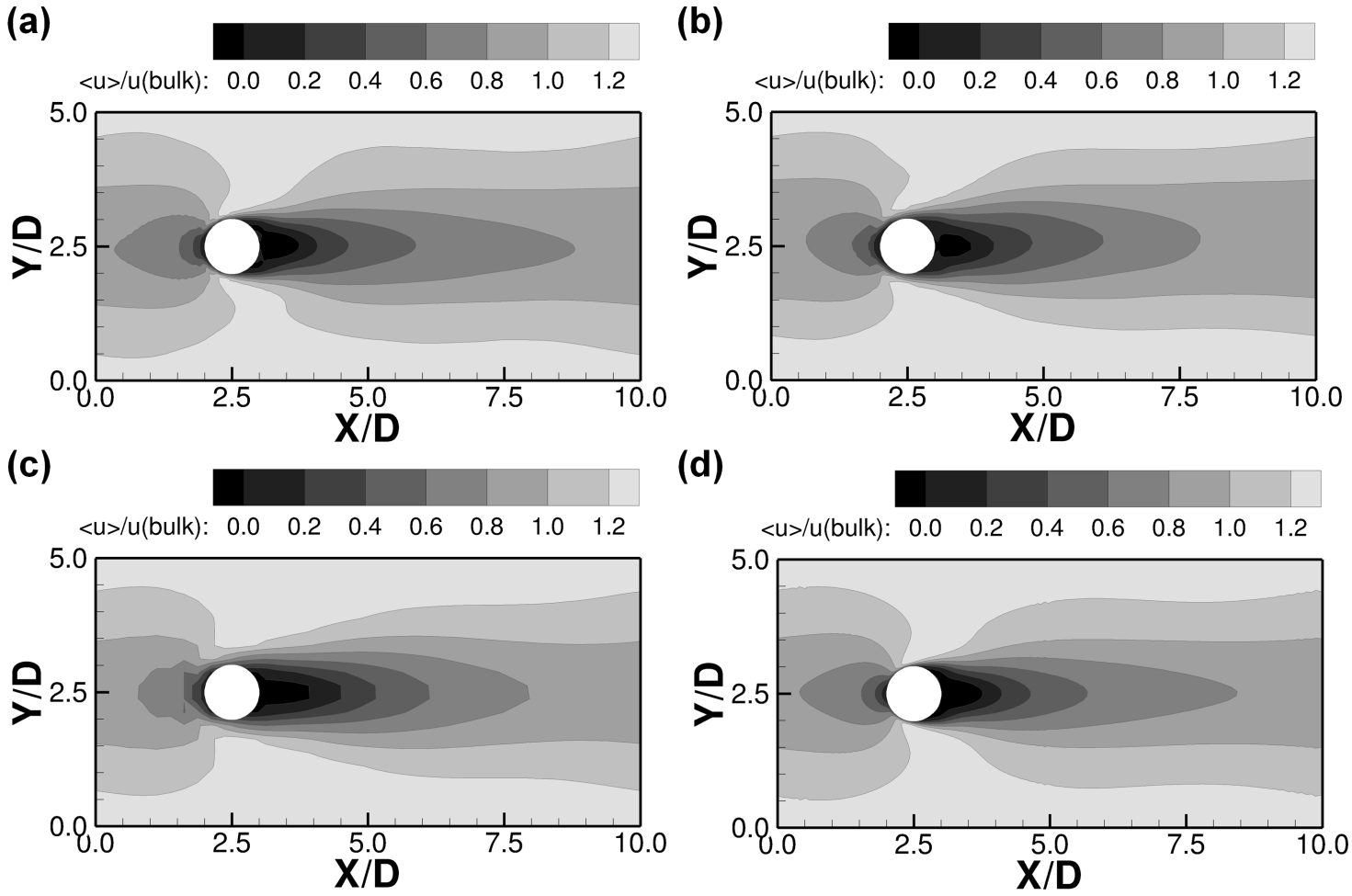

Figure 33: Distribution of time-averaged velocity of the $\phi = 0.016$ case at $Re_D = 500$ simulated on various grids by low-resolution LES, (a)-(c) ($Z/D = 5$) and by (d) high-resolution LES

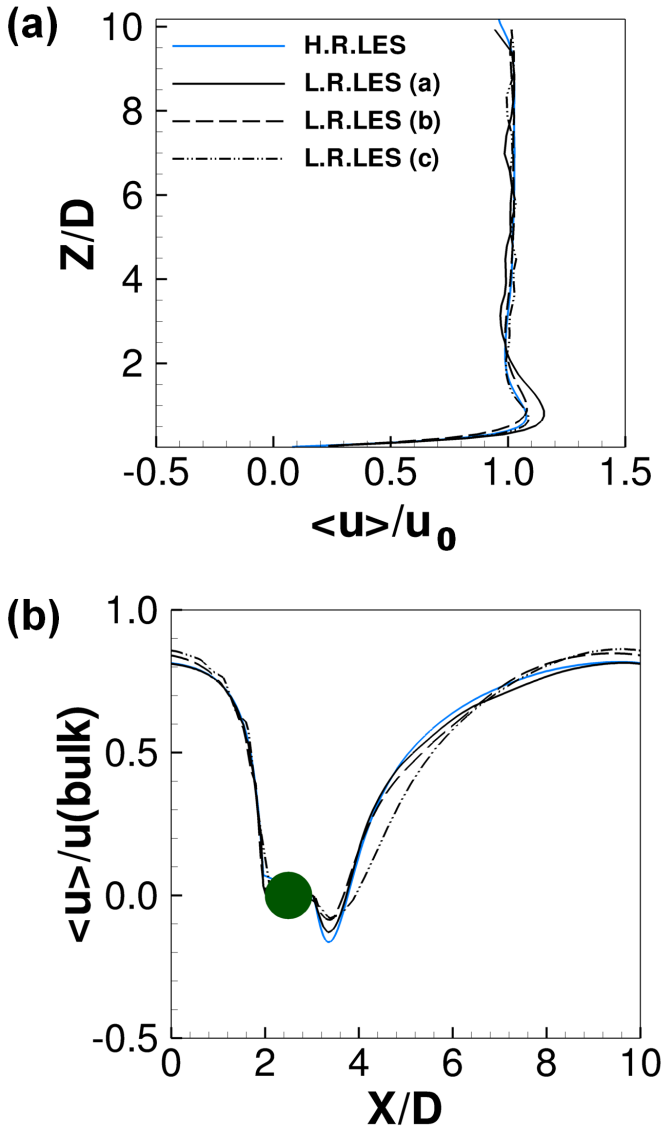

Figure 34: Profiles of (a) spatially-averaged streamwise velocity profiles in vertical direction and (b) time-averaged velocity along center line for $\phi = 0.016$ at $Re_D = 500$

3.5 Conclusions

In this study, the importance of *a-priori* knowledge of drag coefficients in RANS models was investigated first. The RANS simulations performed herein demonstrated that the drag coefficient, an empirical parameter, is key to the accuracy of RANS simulations of flow through vegetation. With *a-priori* knowledge of drag coefficients, accurate flow resistance predictions were achieved. At high vegetation densities, flow resistance due to vegetation would be severely underestimated, if a wrong C_D was used. In flow through emergent vegetation, bed friction is assumed negligibly small and measurements of drag coefficients lump the bed friction into the vegetation drag. When separating bed friction from vegetation drag in RANS simulations of flow through vegetation, predictions of flow resistance in the system are not necessarily improved, at least not for the vegetation densities investigated herein. In order to circumvent the dependency of numerical simulations of flow through vegetation on an empirical parameter, in particular for more complex vegetation arrangements than the ones presented herein, the method of low-resolution LES was introduced and evaluated. Low-resolution LES has the prospect to compute vegetation drag for complex vegetation arrangements with considerably less computational effort than high-resolution LES and without empirical input. The method combines large eddy simulations with a first order immersed boundary method on relatively coarse Cartesian grids. The results indicate that the proposed method provides reasonable accuracy in terms of predicting bulk drag coefficients. It was shown that for low to moderate vegetation densities, velocity gradients, recirculation zones and secondary flows can be predicted quite reliably. However, uncertainties remain for high vegetation densities.

CHAPTER IV

CLOSURE MODELING USING A POROSITY APPROACH FOR A SUBMERGED NATURAL PLANT

4.1 Introduction

In recent years structural measures at watercourses has focused more and more on revitalization, which includes reconnection of retention areas and resettlement and succession of vegetation on floodplains. The presence of vegetation in the aquatic environment considerably alters the turbulent flow in streams, rivers, and floodplains. The additional drag exerted by plants decelerates the flow, alters velocity distributions over the cross-section and influences the transport of sediments and solutes. Due to the additional resistance of plants, there is an increasing risk of flooding in the vicinity and upstream of revitalized stretches rivers and streams. Over the last three decades a number of experimental studies have focused on detailed examination of the flow and turbulence structure within a plant canopy. Most of the experimental studies idealized the vegetation as an array of rigid cylinders, usually at regular spacing [5, 28, 34, 46, 60] and have observed that the spatially and time-averaged velocity profile within an emergent or submerged vegetated layer (irrespective of whether the vegetation is rigid or flexible) no longer follows the universal logarithmic law. The flow resistance of a rigid cylinder can be quantified with the drag force approach [36], for which the only unknown input parameter is the drag coeffcient C_D. The drag coefficient, however, is not constant but varies greatly as a function both vegetation density and stem Reynolds number [58, 50]. Only few studies to date have dealt with natural plants, for which the presence of leaves and the vegetation's flexibility need to be taken into account for the quantification the vegetation's flow resistance. Fathi-Maghadam and

Kouwen [7] were one of the first researchers to account for the flexibility of the plants. They used coniferous trees to demonstrate that the variation of the drag coefficient depends on the approach flow condition due to increased bending of the vegetation at higher velocities. Oplatka [32] and Järvelä [14] were the first to carry out experiments with willows, one of the most common vegetation species on floodplains. Oplatka [32] focused on the load capacity of the plant's roots, but also analyzed the resistance behavior of the plants in the flow. He concluded that the drag force of bent willows may be proportional to $(velocity)^1$ instead of $(velocity)^2$. Järvelä [14] installed willows with and without leafs in different patterns and analyzed the effect of leafs on the flow resistance. He proposed three additional factors to be included into the common vegetation drag formula. Yagci et al. [68] used real coniferous vegetation in their laboratory experiments to analyze the flow characteristics upstream and downstream of single emergent vegetation elements. They observed an increase of Reynolds-Stress due to the vegetation, a recirculation zone near the water surface and an increase of flow velocity near the bed. Obviously, the flow observed in Yagci et al.'s experiment is quite different from the one observed behind rigid cylinders, and flow features and flow resistance characteristics depend strongly on the biomechanics and the nature of the vegetation.

Besides the experimental work mentioned above, several computational fluid dynamics studies were reported in the literature. The majority of CFD studies employed models that are based on the Reynolds-averaged-Navier-Stokes (RANS) equations in which the additional form drag due to vegetation is accounted for through subgrid forces that are added to the momentum and turbulence model transport equations. RANS models with a drag force vegetation closure model offer reasonable accuracy in the prediction of the time-averaged flow field and the flow resistance [2, 4, 9, 22, 25, 27] for idealized flows but still require empirical input in form of a drag coefficient. Kim and Stoesser [16] recently demonstrated the importance of *a-priori* knowledge of the

drag coefficient, C_D, in the context of RANS. One way of avoiding the C_D empiricism in numerical models of flow through vegetation is to resolve the vegetation explicitly through the numerical grid. This was recently done by Stoesser et al. [53, 50] who performed several LES of the flow through submerged and emergent vegetation (idealized as a matrix of rigid cylinders). These LES do not employ a vegetation closure model but the vegetation geometry is simplified and resolving the boundary layer on each vegetation element is computationally very demanding. Hence, LES is limited to relatively simple (vegetation) geometries and relatively low stem Reynolds numbers due to its need for very fine grids. Obviously, there are a number of challenges in moving towards accurate numerical modeling of the effect of real vegetation on the flow. One challenge is to account for the nature of the vegetation, including its biomechanics, in a physically realistic way, for which no universal relationships exist. Another challenge is to acquire relevant input parameters from the field or from laboratory experiments, which are then fed into the numerical models. To our knowledge there has been no attempt to date to simulate flow through natural vegetation other than to use the cylinder analogy and calibrate the input parameter to match observations.

In Chapter 4, we present a new method that is based on a porosity approach to simulate flow through natural vegetation. In order to validate the method, data from laboratory experiments of flow through a submerged natural plant are used. Flow velocities were measured at a high spatial resolution for two different conditions.

4.2 Test Cases

4.2.1 Laboratory Experiments at the Karlsruhe Institute of Technology

Experiments were conducted in a 0.60 m wide 0.70 m deep and 24 m long glass-walled flume in the hydraulics lab of the department of Water Resources Management and Rural Engineering at the Karlsruhe Institute of Technology. The slope of the flume was fixed at 0.18 %. The water entered the flume from a head tank through a stilling basin and a flow straightener made out of a perforated metal plate. The following 10 m stretch was used to develop the flow. The vegetation element was fixed at a pin in the center of the flume (see Figure 35). To obtain the desired flow depth an adjustable weir was installed at the downstream end of the flume. For velocity measurement a 2D electromagnetic sensor P-EMS E30 from *Delft Hydraulics* was used with a sampling rate of 100 Hz and a measuring period of 2 min at each point. This device allowed measuring flow within the plant. Data were recorded for streamwise and spanwise directions (u *and* v) at a fixed water depth of $h = 0.30$ m and a plant height in dry condition of $y_0 = 0.30$ m. Table 7 summarises the experimental conditions.

In Table 7, u_{bulk} is the mean flow velocity [m/s], h is the plant height in dry condition [m], Q is the discharge through the channel [l/s], H is the water depth [m], Re is the Reynolds number and Fr is the Froude number. Willows and shrubs are the dominating plants on floodplain areas, however the vegetative period of willows, within which the plants display foliage, lasts only four months a year. In addition,

Table 7: Experimental conditions

Test run	u_{bulk}, m/s	h, m	Q, l/s	H, m	Re	Fr
1	0.30	0.30	54	0.30	34,600	0.17
2	0.60	0.30	108	0.30	69,200	0.35

preliminary tests showed that the leaves of natural willows do not withstand the time-consuming measurements when cut and put into the laboratory flume. Therefore, a surrogate plant specie was used for the lab experiments. Schneider [45] tested several more resistant cultured plants and reported that *ficus natascha* is similar in terms of its habitus, shape and biomechanics as willows. Thus for each test run three fresh cut *ficus natascha* branches with a height of 0.30 m were attached to the pin.

As soon as the plant is subjected to the flow it bends and remains at its bent position in a quasi steady manner. For the numerical simulations, the geometry of the bent plant has to be taken into account. Thus, for each test run, pictures of the plant under hydrodynamic load were taken from the top, the front and from the side (see Figure 35 (upper row)). As the front view pictures had to be taken below the water surface the underwater camera Olympus $\mu 1030SW$ was used. For the side view and the plan view pictures ,the camera was fixed at a tripod at a distance of 1.5 m from the flume side wall and the water surface, respectively. The angle of light refraction within the water changes in comparison to air conditions. Additionally the water has a filtering effect of light frequencies. Thus the front view pictures were taken at a distance of 1 m upstream of the plant. The photographs were then digitalized to provide input data for the numerical simulations (see Figure 35 (lower row)).

In Figure 35, x, y and z are the coordinates of the system, H is the water depth [m] and B is the width of the channel [m]. Figure 36 shows the grid of the velocity measurement profiles. The grid consists of 19 cross sections and 17 spanwise locations. The vertical profiles consisted of 10 data points. The distance between data points in the vertical was constant at 0.03 m and the first data point was 0.01 m above the bed and the last one 0.02 m below the water surface. The numbering of the cross-sections starts at the pin with $x/H = 0.0$, and included three cross-sections upstream and 15 cross-sections downstream of the pin. The numbering of the spanwise locations starts at the pin with $y/B = 0.0$ and profiles were spaced $y/B = +/-0.05$ apart.

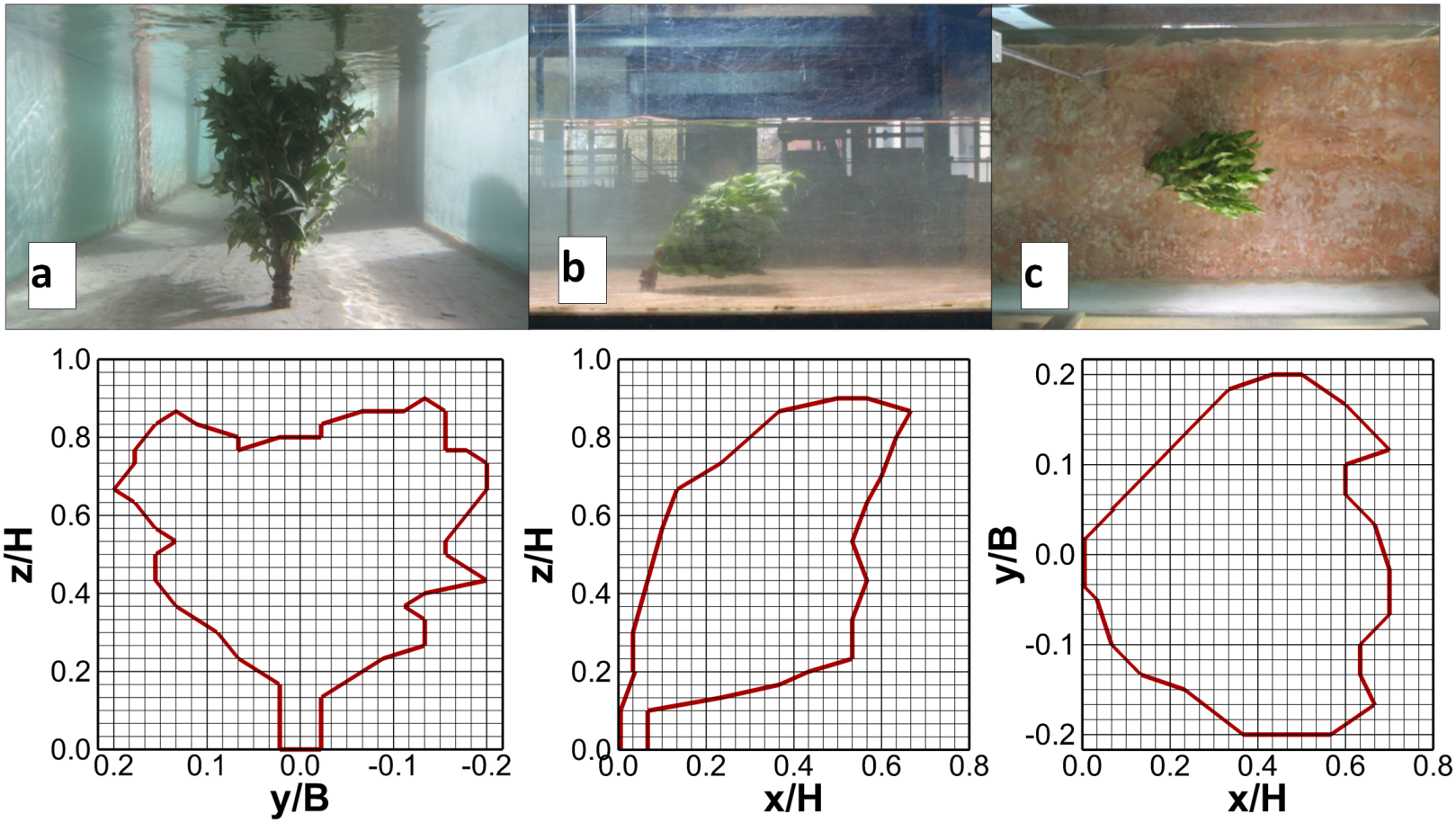

Figure 35: Pictures of the flown through plant (upper row) and discrete distributions of porosity on Cartesian grids (lower row) from (a) front view (b) side view (c) plan view

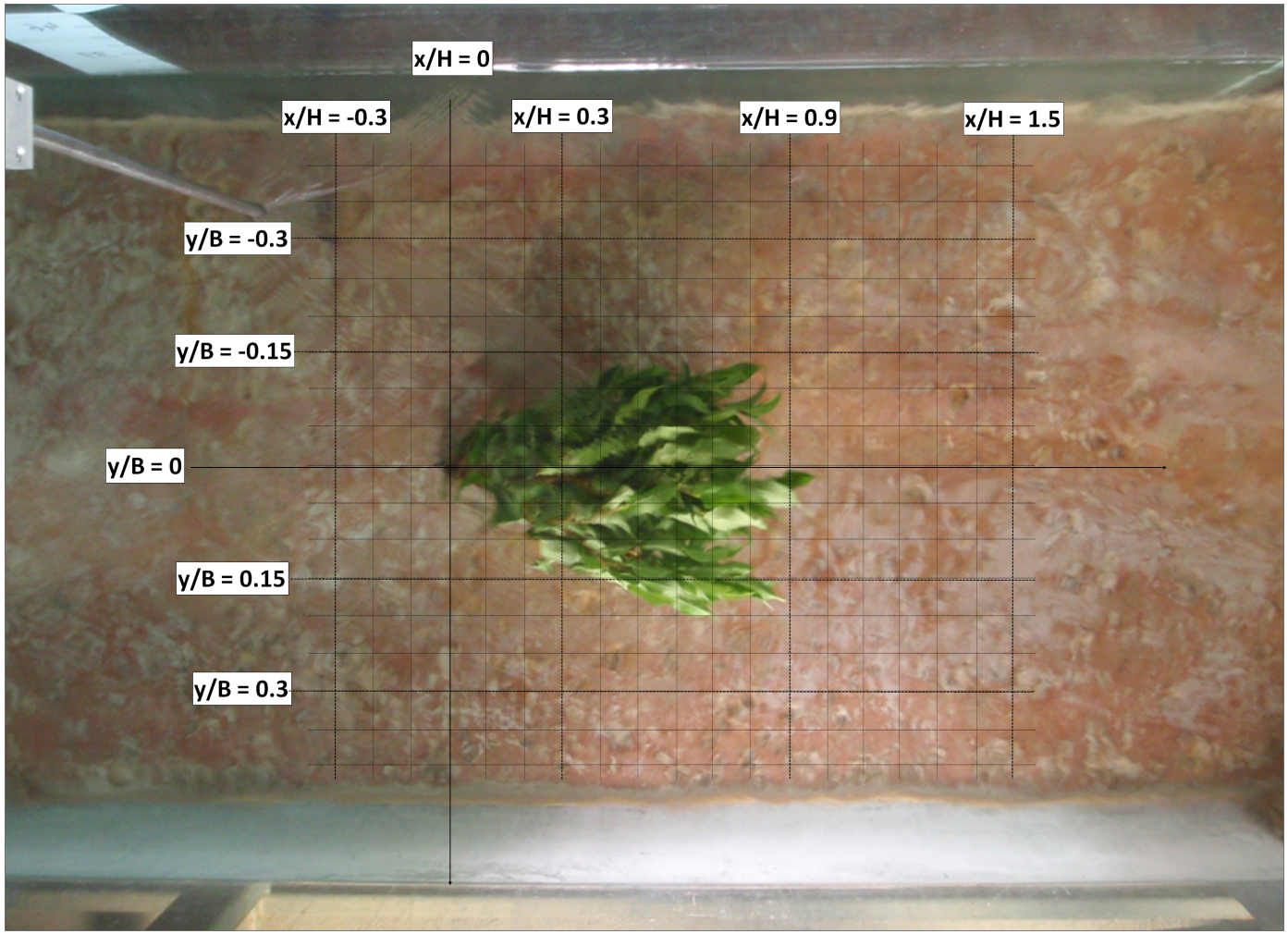

Figure 36: Illustration of the measurement grid from the top view

4.2.2 Determination of LAI

For the RANS simulations the plant's geometry was included into the grid by the use of a porosity approach, which is described in detail in the next section. Thus the distribution of the biomass within the plant had to be known. Therefore, the leaf area index (LAI) of the plant was determined, by:

$$LAI = \frac{LAI_M \cdot N}{A} \tag{8}$$

, in which LAI_M is the mean leaf area of the plant [m^2], N is the number of leaves [-] and A is the area occupied by the plant [m^2]. Due to the non-uniform distribution of the biomass of the plant, it was divided into five characteristic sections as shown in Figure 37: Two peripherical sections (allocation Characters 1 and 5), a section around the center of the plant (allocation Character 3) and the two parts between periphery and center (Characters 2 and 4). For each part the LAI was determined, which is then used to choose porosity values of the discrete plant.

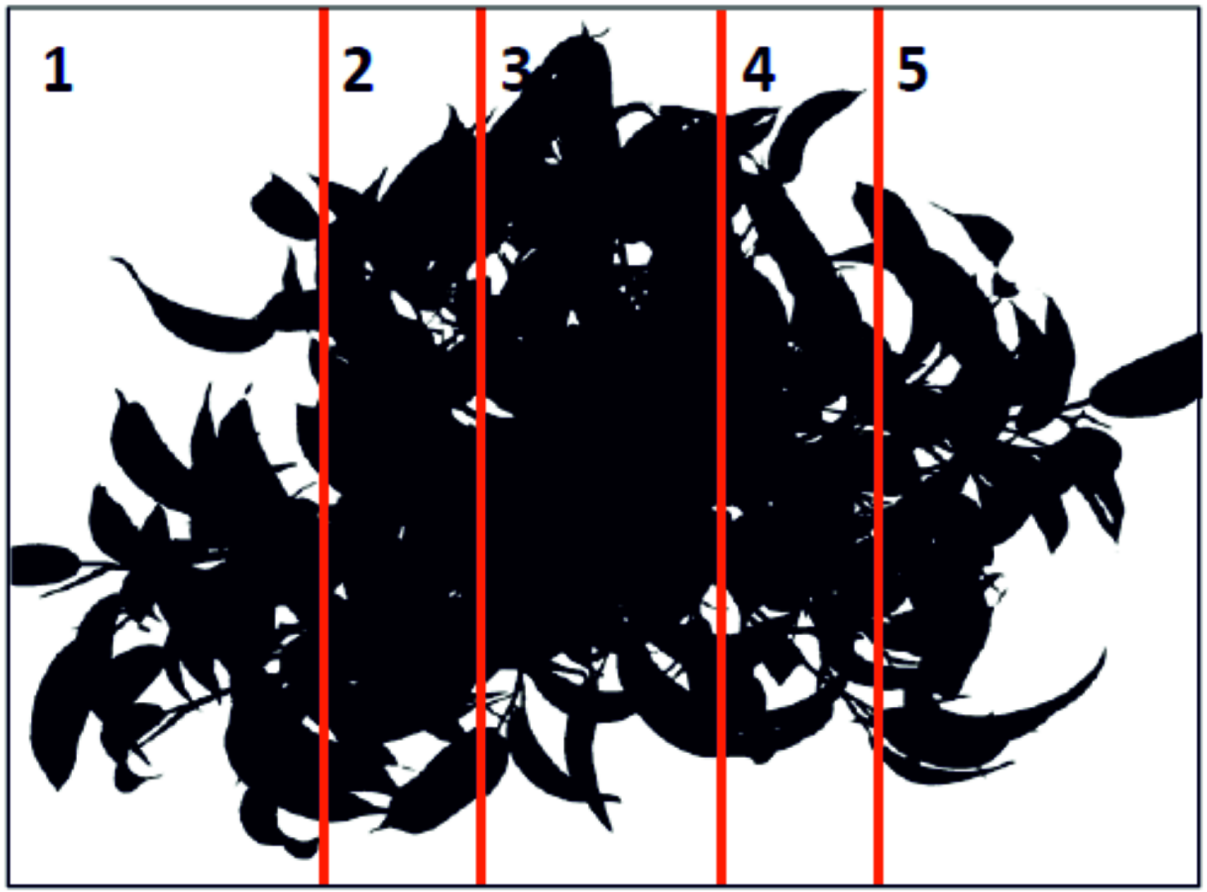

Figure 37: Determination of LAI

4.3 Numerical Framework

4.3.1 Numerical Model

The turbulent flow through and above a natural plant is calculated by the RANS model SSIIM (Sediment Simulation In Intakes with Multiblock option), which solves the Reynolds averaged Navier-Stokes (RANS) equations on a Cartesian grid using a finite volume scheme [9, 37]. The RANS equations read:

$$\frac{\partial U_i}{\partial t} + U_j \frac{\partial U_i}{\partial x_j} = \frac{1}{\rho} \frac{\partial}{\partial x_j} \left(-P\delta_{ij} - \rho \overline{u_i' u_j'} \right) - f_i \tag{9}$$

, in which U is the time-average velocity vector, x is the spatial geometrical scale, ρ is the water density, P is the pressure, δ is the Kronecker delta and u' is the velocity fluctuationvector ($u' = u - U$), in which u is the instantaneous velocity. The first and second terms on the left hand side of the equation are the transient term and the convective term, respectively. Since this is a steady state flow the transient term is zero. The convective term is approximated with a second order upwind scheme, while the diffusive term is approximated with a second order central differencing scheme. The first term on the right hand side is the pressure term, which is calculated from an iterative procedure based on the SIMPLE algorithm [35]. The second term on the right hand side of the equation is the Reynolds stress which requires a suitable closure model. The eddy-viscosity concept is introduced with the Boussinesq approximation to model the Reynolds stress term. The turbulent eddy viscosity is determined by the standard $k - \varepsilon$ turbulence model.

4.3.2 Porosity Approach

In this study a new vegetation closure method is introduced. It is proposed to model the plant with foliage by a porosity approach, which should be regarded as an exerting force from the porous plant on the water in each numerical cell. The porosity approach uses a formula for flow in porous media suggested by Engelund [6]:

$$I = \beta_0 \frac{1-n}{n^3} \cdot \frac{U^2}{gd} \tag{10}$$

, in which, I is the hydraulic gradient, β_0 is a constant, and n is the porosity. A β_0 value of 3.0 was suggested by Engelund, and was used by Olsen and Stokseth [31]. However it should be noted that Olsen and Stokseth [31] used the porosity approach in the context of large bed roughness, whereas the present study uses porosity in the context of a permeable obstruction over most of the water column.

In order to evaluate the aptitude of the proposed porosity approach, computations are also carried out with a traditional drag force vegetation closure. Therein the vegetation is typically modelled as a rigid circular cylinder for which the drag force formula applies [9]. Two input parameters are needed: 1) the drag coefficient, C_D and 2) the diameter of the cylinder occupying each computational cell. Since there is no information on C_D, C_D=1.0 is assumed. The diameter of the imaginary cylinder in each cell is computed from the porosity values determined from the LAI study as follows:

$$\frac{\frac{\pi D^2}{4} \times \Delta z}{\Delta x \Delta y \Delta z} = 1 - n \tag{11}$$

, in which, the numerator of the term on the left-hand side is the volume of the imaginary vertical cylinder and the denominator is the total volume of a finite volume cell.

4.3.3 Numerical Setup and Boundary Conditions

The numerical domain for the experimental flume spans 12 m $\times$ 0.6 m $\times$ 0.3 m (in x, y, and z directions, respectively) and the finest grid consisted of 380,091 ($= 201 \times 61 \times 31$) grid points. Uniform grid spacing is used for both spanwise- and vertical- directions while the grid is stretched in the streamwise- direction, except for the area around the plant, where a uniform spacing is used. Figure 38 shows every 5th gridline in x- and every 3rd of y- grid line of the grid in a horizontal plane.

A dirichlet condition was used at the inlet at which a discharge was prescribed. At the outlet a von Neumann condition was used for all variables. Channel bed and side walls are treated with a no-slip condition and the slip condition is applied at the free surface boundary. In order to avoid resolving the viscous sublayer the channel bed and sidewalls were treated by using walls laws in the first cell above the rough bed (Schlichting [44]). The velocity at this location is calculated as:

$$\frac{U}{U_*} = \frac{1}{\kappa} \ln\left(\frac{30z}{k_s}\right) \tag{12}$$

, in which, U_* is the shear velocity, z is the distance from the wall, and k_s is the equivalent sandgrain roughness height. The values of k_s can be computed from a Manning's n value, which is calibrated from the experiments:

$$k_s = \left(\frac{26}{n}\right)^6 \tag{13}$$

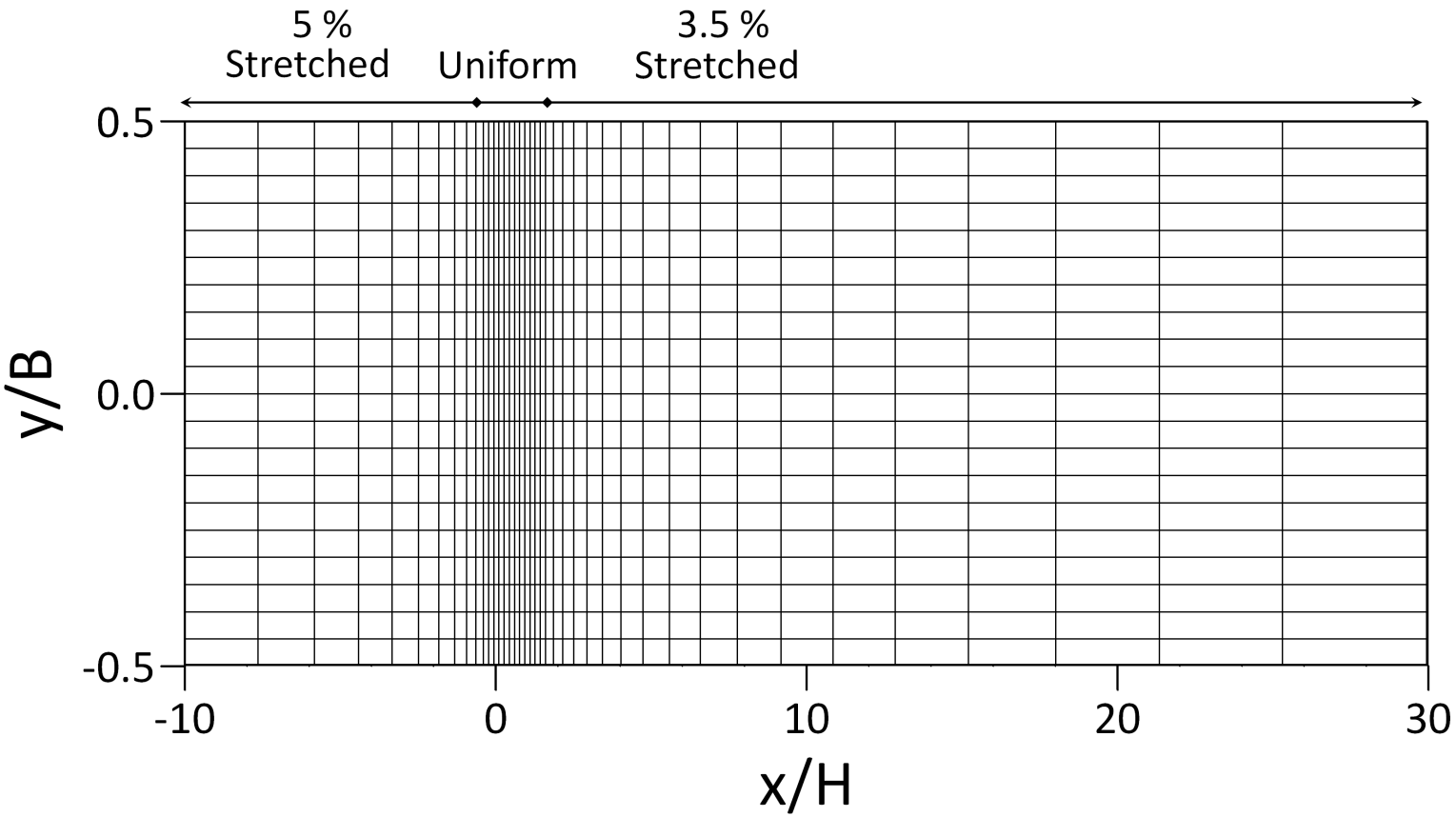

Figure 38: Numerical grid of the RANS simulations

4.4 Results and Discussion

4.4.1 Model Calibration and Grid Independence

The model roughness, in terms of a Stricklers number k_{st}, is calibrated by measured streamwise velocity profiles of the experiment without vegetation for the two cases, $u_{bulk} = 0.3$ m/s and $u_{bulk} = 0.6$ m/s. The required grid resolution as well as the k_{st} is obtained by comparing the numerical results with the measured data.

In Figure 39 the vertical profiles of streamwise time averaged velocity at the channel center are shown for the three grid resolutions tested ($coarse : 61 \times 41 \times 11$), ($fine : 61 \times 41 \times 31$) and ($finer : 201 \times 61 \times 31$). Three different Stricklers numbers were tested, i.e. $k_{st} = 60$, $k_{st} = 70$, $k_{st} = 80$ and profiles are compared to the measured values (U_E). The discrepancies near the water surface either are a result of secondary currents prevailing in the laboratory channel, a feature that an isotropic turbulence model like the standard k-eps model can not reproduce. However, besides this discrepancy the computed velocity profiles match the observations very well for both cases and the Stricklers number has only minor influence. In the following a Stricklers number of $k_{st} = 70$ is used to account for bed roughness.

Figure 40 shows contours of u/u_{bulk} for one selected cross-section in the channel for both cases $u_{bulk} = 0.3$ m/s and $u_{bulk} = 0.6$ m/s. The measurement data is plotted in the top left, followed by calculated data for each grid resolution (coarse, fine, finer). There is no significant difference between the simulations with different grid resolution and the experiments. Thus for further simulation with the plant in place the fine grid resolution ($61 \times 41 \times 31$) was chosen.

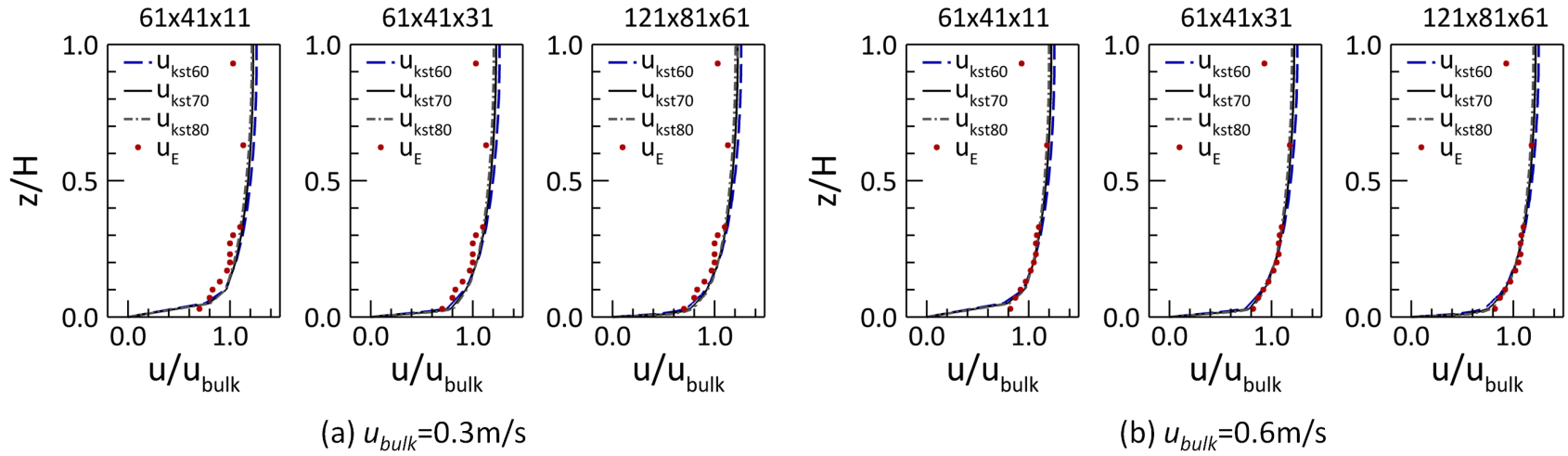

Figure 39: Profiles of time-averaged streamwise velocity at the center ($y/B = 0.0$): measurements (u_E) and RANS simulations using three Stricklers numbers ($u_{k_{st}}$) for three grid resolutions

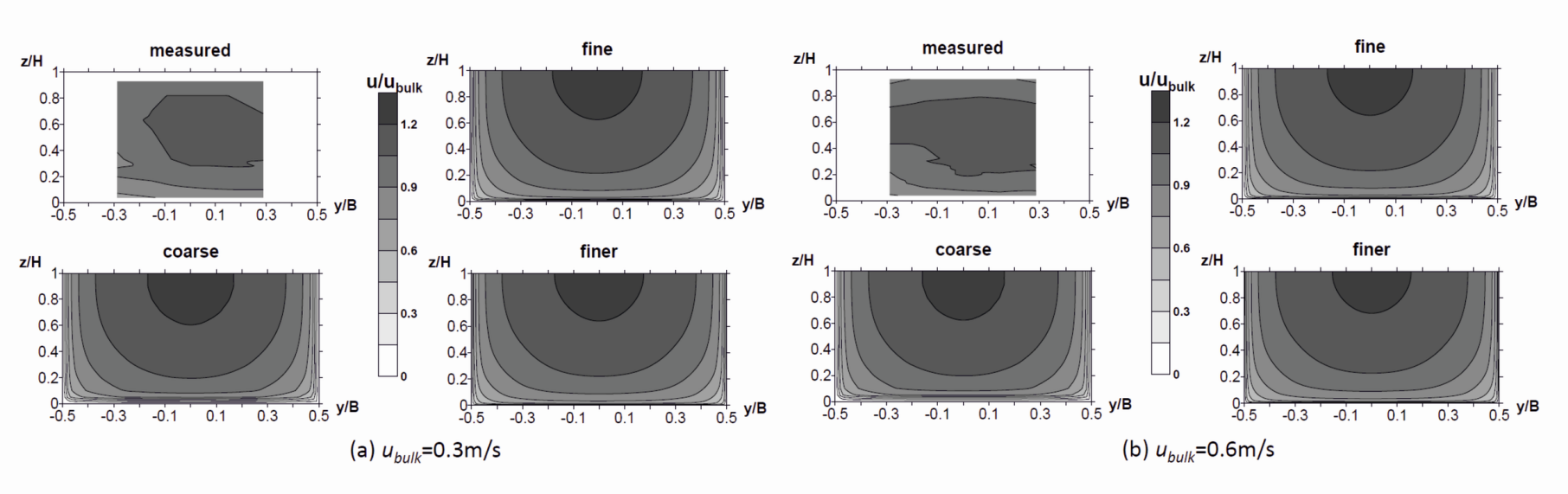

Figure 40: Contour plots of time-averaged velocity of the $u_{bulk} = 0.3$ m/s and $u_{bulk} = 0.6$ m/s

Table 8: LAI and porosity

Section	1	2	3	4	5	LAI_{bulk}
LAI	3.31	4.85	5.24	4.40	2.30	4.23
LAI/LAI_{bulk}	0.78	1.15	1.24	1.04	0.54	
Porosity	0.99	0.97	0.95	0.97	0.99	

For defining the porosity values within the discrete plant the LAI of the five characteristical sections of the natural plant as described in Chapter 4.2 is made use of. Table 8 lists the gained values of LAI.

The mean LAI_{bulk} is 4.25 and correspond to the LAI of 3 year old willows according to Ross et. al. [43]. The higher the value of LAI the higher is the plant's biomass. The distribution of the LAI-values display the tendency of biomass distribution could be estimated. However the LAI is just a reference value, as it does not correspond directly to biomass and thus to porosity. Hence further investigations regarding the distribution of biomass within several shrub species are needed. Therefore the porosity values were determined iterative by comparing the numerical results with the measured values (See Chapter 4.2). For this purpose the discrete plant was sectioned according to the five characteristic parts like the natural plant. In each part the grid cells were occupied by porosity values assumed by the distribution of LAI (see Figure 41). The values vary from 0.99 to 0.95, whereas the higher the value the lower is the plant's biomass per volume respectively LAI.

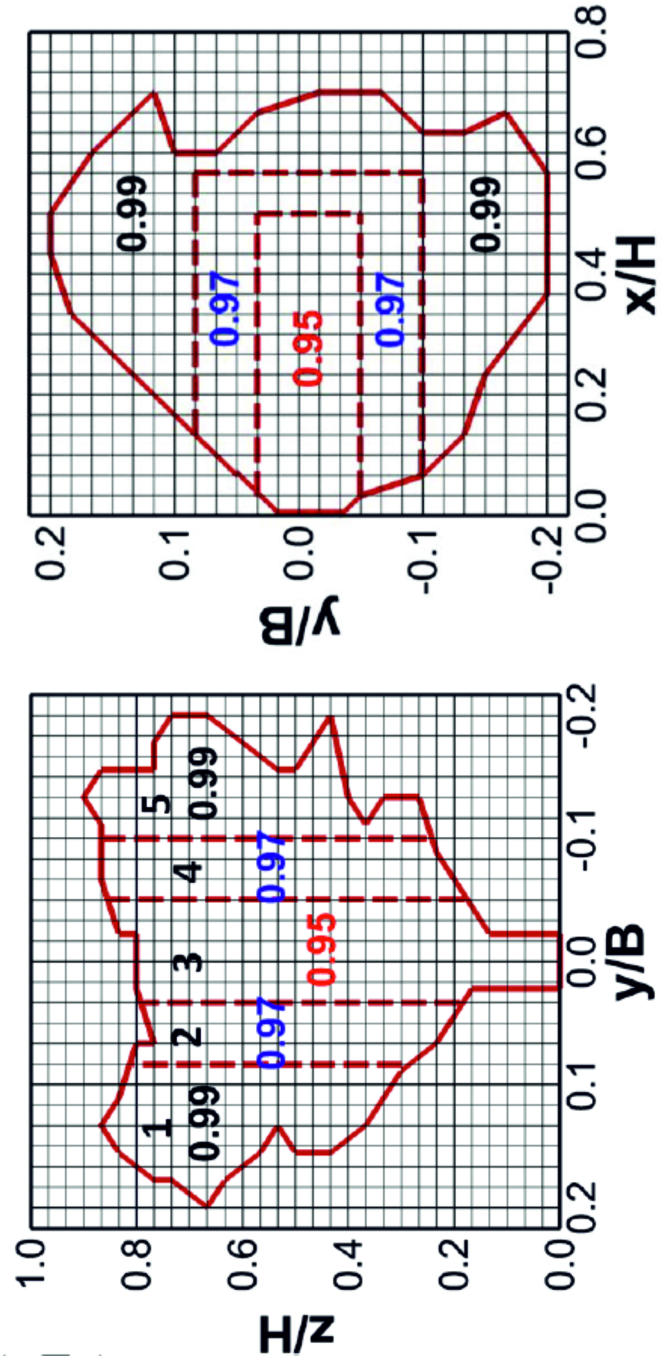

Figure 41: Concept of LAI and porosity

4.4.2 Validation by Comparing Experimental and Numerical Results

Figures 42 and 43 present contours of the measured (Figure 42) and calculated (Figure 43) streamwise velocity for the $u_{bulk} = 0.3$ m/s and $u_{bulk} = 0.6$ m/s cases in selected cross-sections. In each figure the first cross-section is positioned upstream of the plant ($x/H = -0.2$), the second is positioned directly above the pin ($x/H = 0.0$), followed by three cross-sections within the plant ($x/H = 0.2$ to $x/H = 0.6$), one at the end of the plant ($x/H = 0.8$) and three within the downstream area of the plant ($x/H = 1.0$ to $x/H = 1.4$). The distances between the cross-sections is 0.06 m each.

The flow is influenced strongly by the presence of the plant, and the flow is decelerated markedly in the center of the channel as a result of the obstruction. The obstruction is hardly noticed upstream of the plant ($x/H = 0 - 0.2$) but already at the pin ($x/H = 0.0$) the velocity contours exhibit a bulge. As the flow enters the plant a region of low momentum develops and continues to grow until approximately $x/H = 1.0$, which is already outside and downstream of the plant. In the following the flow recovers but only very slowly. There are a few intersting differences between the two cases investigated. In the $u_{bulk} = 0.3$ m/s flow, the bending of the plant is less severe than in the $u_{bulk} = 0.6$ m/s case, which has consequences on the hydrodynamics. First of all, the deceleration of the flow in the center of the channel starts earlier in the lower velocity case, a result of the plant being less deflected from the vertical due to smaller hydrodynamic forces acting on the plant. This can be seen by comparing velocity contours at $x/h = 0.0$ and $x/H = 0.2$. Within the plant (i.e., $x/H = 0.4$, $x/H = 0.6$, $x/H = 0.8$) there is more water that is conveyed over the top of the plant in the $u_{bulk} = 0.6$ m/s case, which is also a result of increased bending at higher discharge. What follows is that there is more water being conveyed along the sides of the plant when subjected to a lower bulk velocity. All this is being predicted quite well by the numerical model. A few discrepancies are observed but the overall behaviour, in particular the effect of bending and porosity on the flow, is predicted

satisfyingly.

The calculated contour plots fit well to the measured ones disregarding small fluctuations within the measured values, which are a result of oscillation of the natural plant in the current. The plant is flown through, but the flow velocity decreases from plant boundary to the centreline. This effect is linked to the mass distribution of the plant determined with LAI and simulated with porosity values. Both cases of flow velocity ($u_{bulk} = 0.3$ m/s and $u_{bulk} = 0.6$ m/s) were simulated by the same distribution of porosity values within the geometry of the discrete plant. However, for both cases the simulation results fit well to the measured ones. Thus it can be assumed that the porosity approach is independent from averaged flow velocity, but the geometry of the bended plant has to be known.

Figures 44 and 45 show a comparison of vertical profiles of time-averaged flow velocity at the plants centerline (first row), at the boundary of the plant (second row) and between the plants boundary and the channel wall (third row), whereas Figure 44 shows the profiles of $u_{bulk} = 0.3$ m/s and Figure 45 the ones of $u_{bulk} = 0.6$ m/s. The solid lined profiles show the results of simulation with porosity approach (U_P), the dotted lined profiles show the results of simulation with drag force approach (U_D) and the single dots show the results of experiments (U_P).

The influence of the plant to the distribution of flow velocity in spanwise direction can be seen by comparing the three rows in both figures. The main influence can be seen at centerline position, where the flow velocity is reduced when the plants geometry starts. The results of porosity approach fit well to the measurement results until $z/H = 0.5$. From this height on the measured flow velocity increases with height with a stronger gradient than the flow velocity simulated by porosity approach. This effect is a result of defining the porosity value in vertical direction. As in the RANS-model SSIIM just four porosity values can be defined in vertical direction it is not possible to change the porosity within the plants geometry itself. But the natural

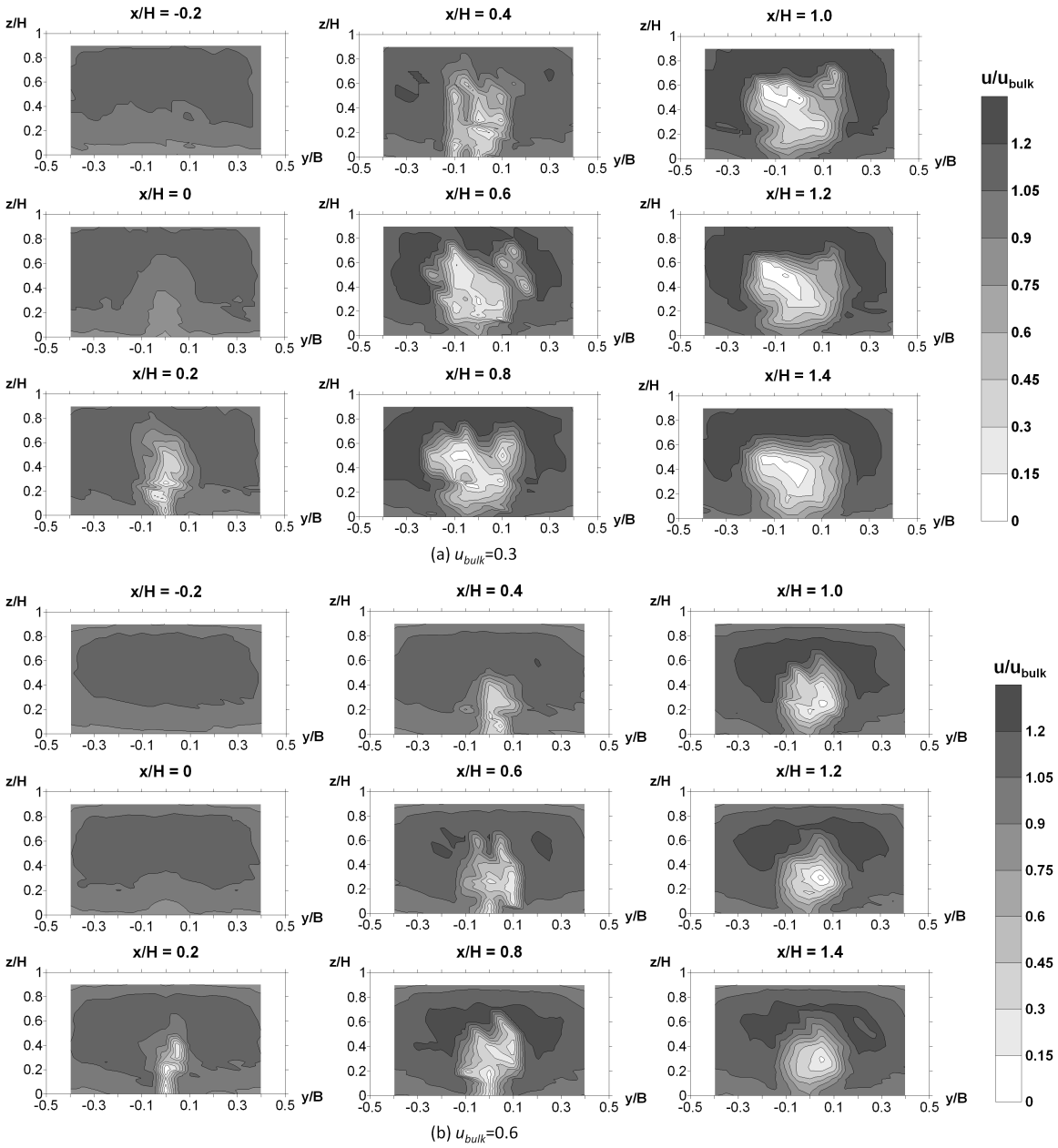

Figure 42: Contours of time-averaged velocity of the $u_{bulk} = 0.3$ m/s and $u_{bulk} = 0.6$ m/s with vegetation at selected cross-sections in the measurement

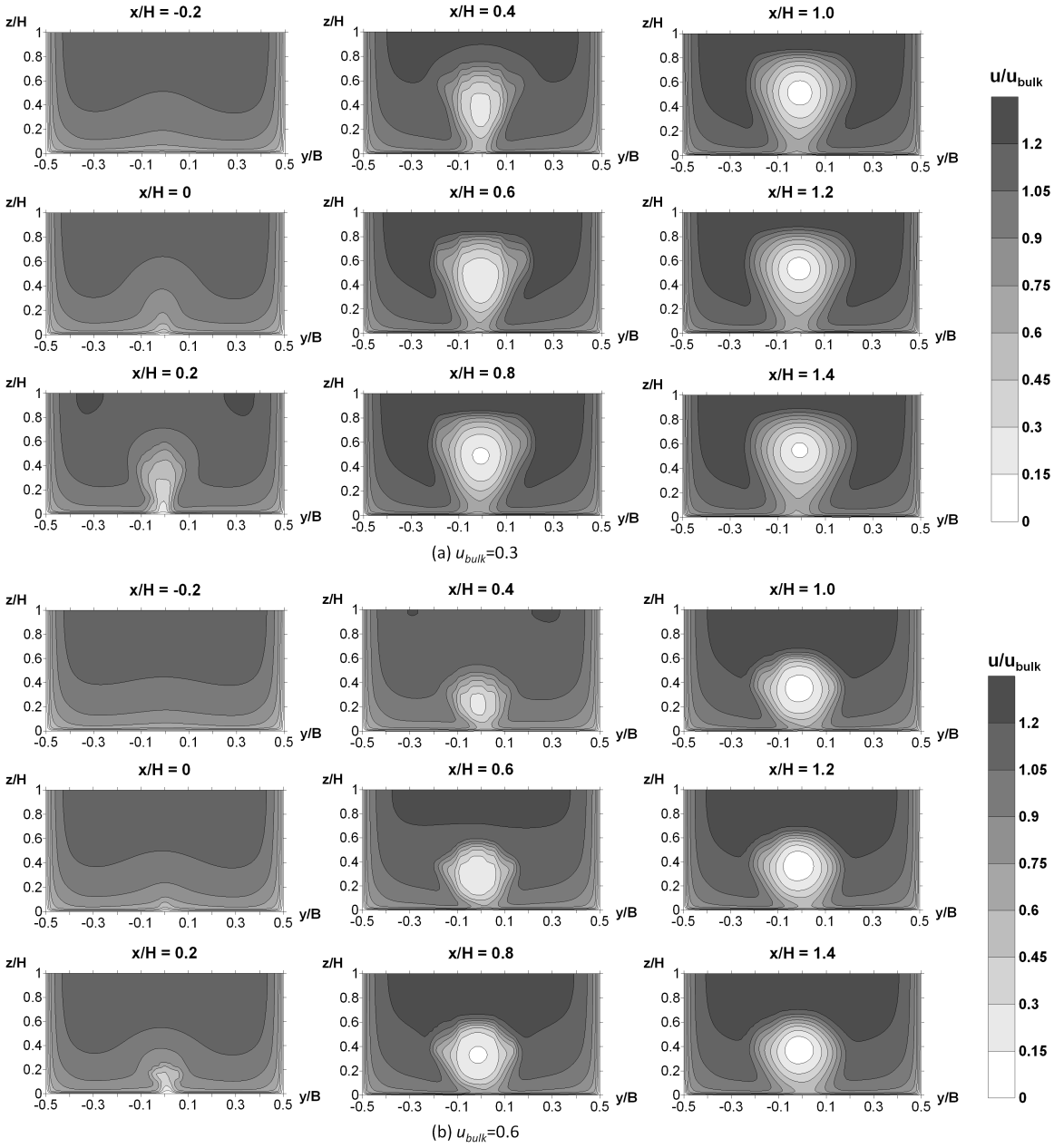

Figure 43: Contours of time-averaged velocity of the $u_{bulk} = 0.3$ m/s and $u_{bulk} = 0.6$ m/s with vegetation at selected cross-sections in the RANS simulations using a porosity model

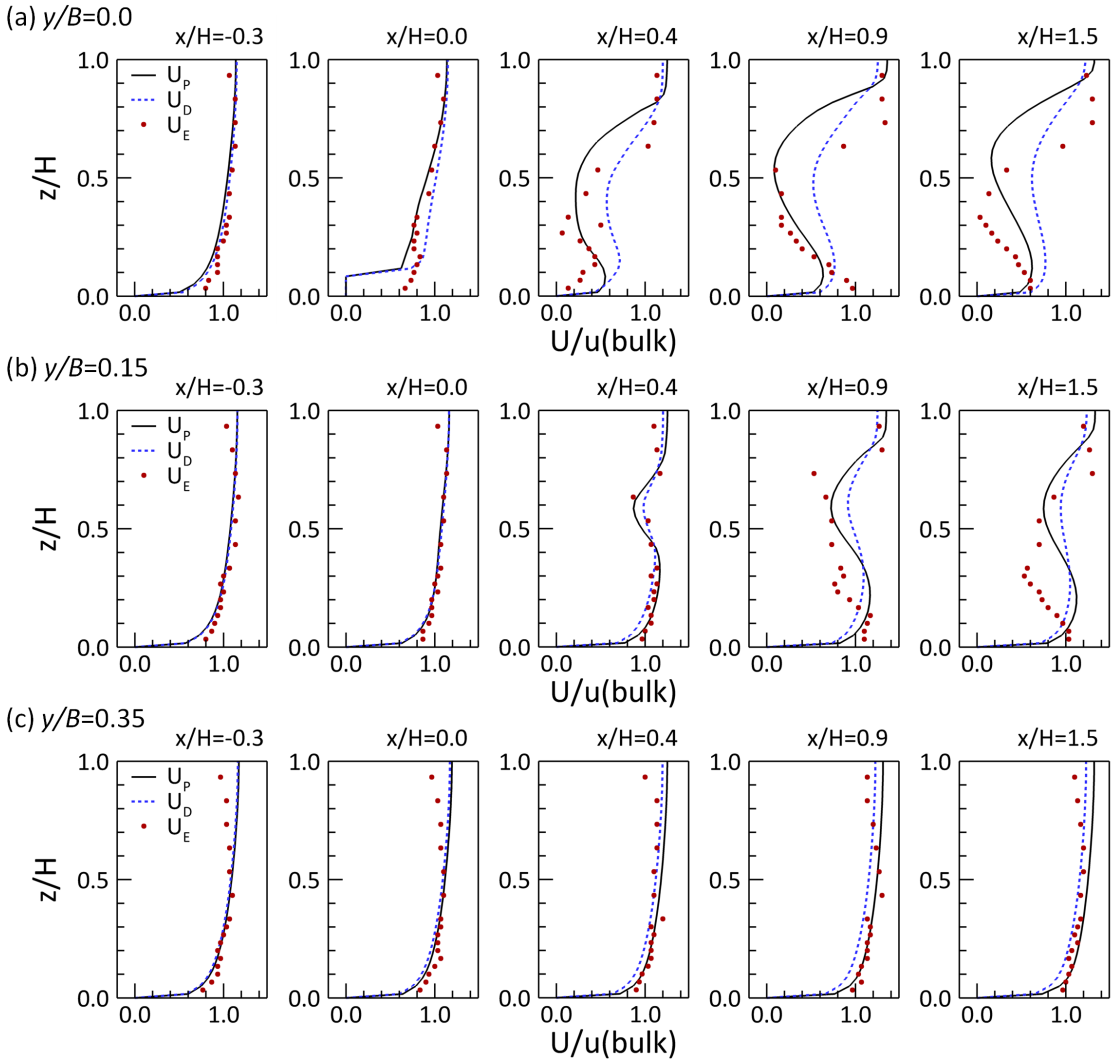

Figure 44: Profiles of time-averaged streamwise velocity from measurements and RANS simulations using porosity and drag models for $u_{bulk} = 0.3$ m/s with vegetation at $(a)\, y/B = 0.0, (b)\, y/B = 0.15$, and $(c)\, y/B = 0.35$ along streamwise direction

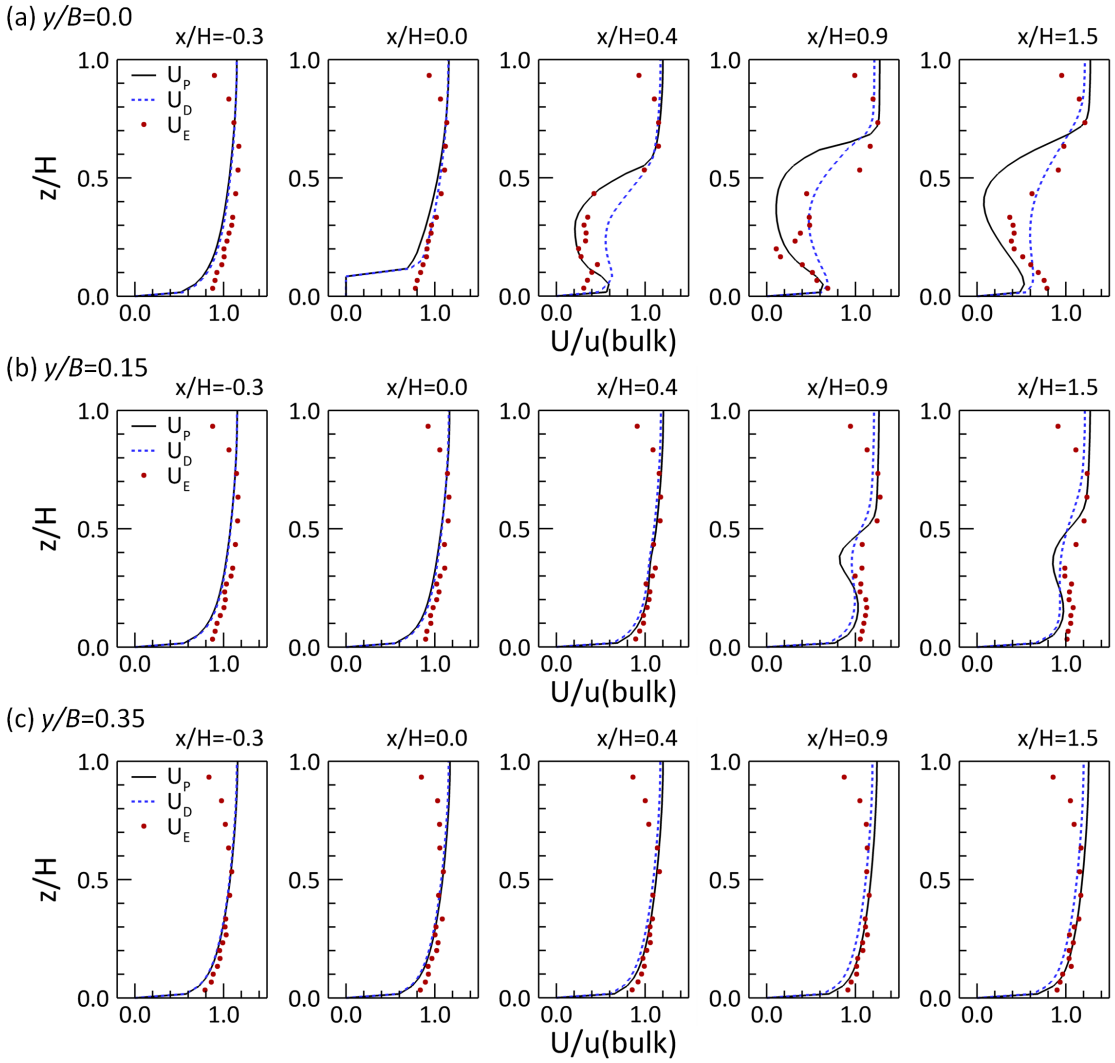

Figure 45: Profiles of time-averaged streamwise velocity from measurements and RANS simulations using porosity and drag models for $u_{bulk} = 0.6$ m/s with vegetation at $(a)\, y/B = 0.0, (b)\, y/B = 0.15$, and $(c)\, y/B = 0.35$ along streamwise direction

plant has less biomass at its upper part than at the main part of the plant. Thus for a better fitting more than four porosity values should be possible to define for vertical direction.

Until now flow resistance of vegetation generally has been simulated using the approach of drag force. Comparing the results of the measurements with the simulation with drag force approach it can be seen, that the simulation fits just for the less influenced parts of the flow. For the use of the drag force approach the plant is simulated like a group of cylindrical elements and it is required to define the drag coefficient C_D as well as the projected area of the cylinders A_p. Thus there are two unknown parameters, that influence the simulation. In addition the shape of shrub-like vegetation is not similar to a group of idealized cylinders, which complicates the definition of the cylinders projected area.

Comparing the second and third row of the figures a strong decrease of the plants influence on the flow with increasing distance from the plant can be observed. This can be an effect of the porous character of the plant which is flown through.

4.4.3 Bed Shear Stress

Bed shear stress around the willow of each case is calculated and plotted in Figure 46. As shown in Chapter 4.3 the wall law is applied to the calculation of the turbulence variables, so the bed shear stress is also quantified by following equation:

$$\tau_b = \rho \left(u\kappa\right)^2 \left(\ln \frac{30z}{k_s}\right)^{-2} \tag{14}$$

, in which, τ_b is the bed shear stress and κ is the von Karman's constant (=0.4187). Meanwhile, in one- or two- equation model calculations, following relation is normally used as boundary condition for k [39]:

$$\frac{k}{{U_*}^2} = \frac{1}{\sqrt{c_\mu}} \tag{15}$$

, in which, the value of c_μ is 0.09 and was chosen on basis of experiments in flows in which the production P and dissipation ϵ of the turbulence energy were in approximate balance [39]. Therefore, the bed shear stress is also evaluated by:

$$\tau_b = \rho {U_*}^2 = \rho \left(0.3k\right) \tag{16}$$

Hence, the bed shear stresses calculated by Equations 14 and 16 are indicated as τ_{b1} and τ_{b2} for simulation results in Figure 46, and are compared to the bed shear stress in measurement, τ_{b3} also calculated by Equation 14. All data are normalized by total shear stress of each case, $\tau_0 = dp/dx \times H$. The first plot shows the bed shear stress along the center-line in streamwise direction, and the others in spanwise direction at particular locations; x/H = -0.3, 0.0, 0.4, 0.9, and 1.5 along streamwise

direction. As a result, the porosity approach reproduces the flow on the bottom affected by the willow well (by comparing τ_{b1} and τ_{b3}), and τ_{b2} shows that high turbulent kinetic energy occurs in the middle of willow, especially at location $x/H = 0.4$ where the width of the willow is the largest.

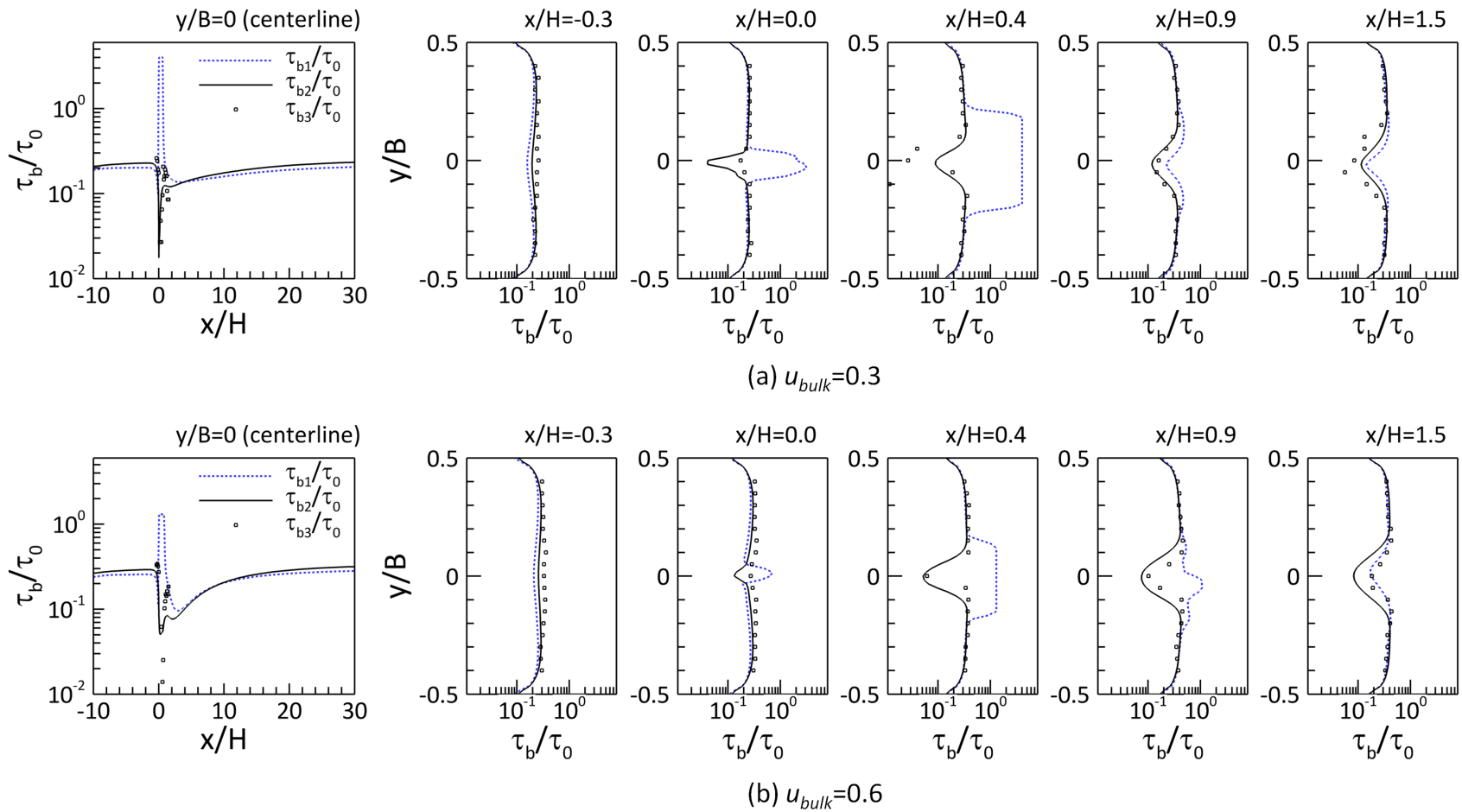

Figure 46: Profiles of bed shear stress from measurements and RANS simulations using porosity models for the (a) $u_{bulk} = 0.3$ m/s and (b) $u_{bulk} = 0.6$ m/s along streamwise direction

4.4.4 Evaluation of porosity approach

The qualitative ability of the porosity approach is assessed in this section.

Figure 47 presents contours of the time-averaged streamwise velocities and streamlines at 10 % and 50 % depths for two cases. Even though streamlines penetrate the center of the willow without clear wakes behind it, velocity gradients both in $x-$ and $y-$ directions exhibit. The distributions and streamlines of the flow also reveal the change of the shape of the willow due to approaching velocity of flow.

Time-averaged turbulent properties are shown in Figure 48. Firstly, a vorticity magnitude is reproduced as an isosurface with 10 % of the maximum value of each case. The isosurface of vorticity magnitude reconstructs the turbulent structures around the willow and also represents the change of the willow shape due to the flow. Then, time-averaged turbulent kinetic energy is plotted on the isosurface. The result shows the high turbulent kinetic energy occurs in the middle of the willow which is already shown in Figure 46. The turbulent kinetic energy which normalized by ${u_{bulk}}^2$ at the inlet and center of willow is almost five times larger than the value of the rest part of the domain.

Secondary currents on selected cross-sections are represented by vectors for both cases in Figure 49. The distribution of the time-averaged streamwise velocities in the figure makes it possible to predict the dimension of the willow, and the secondary currents develop differently in each case due to the final shape of it as described in Figure 46.

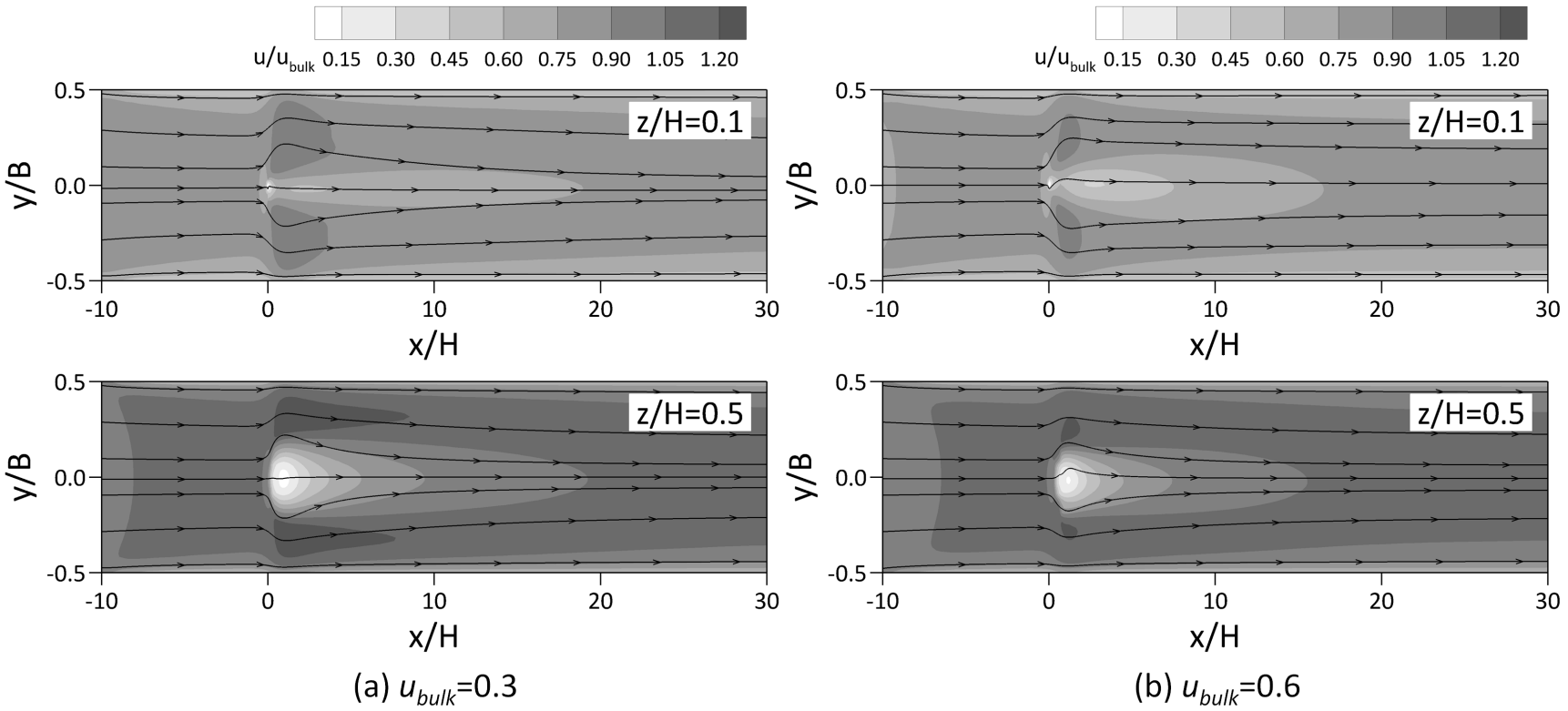

Figure 47: Distribution of time-averaged streamwise velocities in horizontal planes at different height with streamlines for the (a) $u_{bulk} = 0.3$ m/s and (b) $u_{bulk} = 0.6$ m/s cases

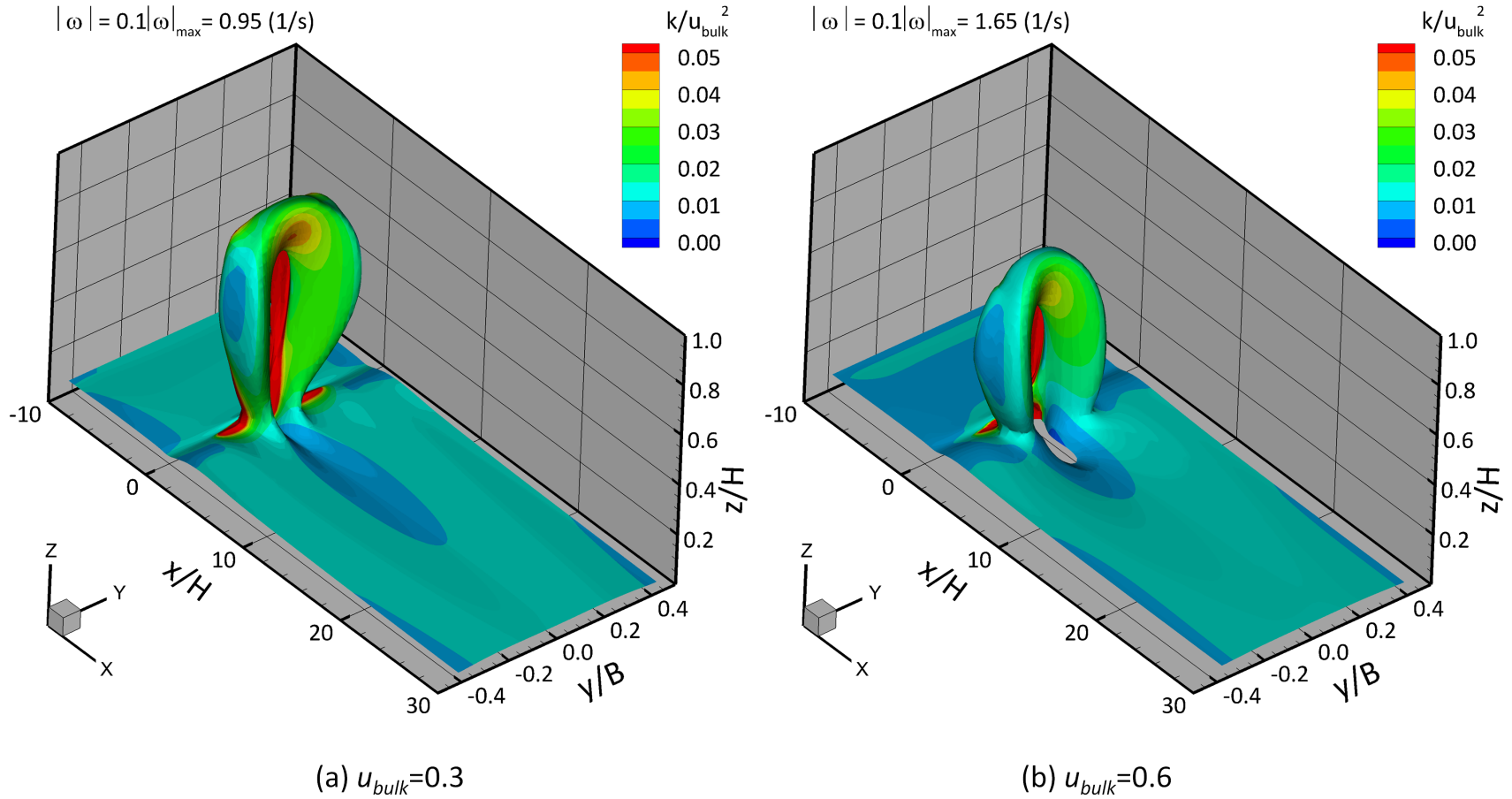

Figure 48: Contours of the time-averaged turbulent kinetic energy around the isosurface of a vorticity magnitude which is 10 % of the maximum value of the (a) $u_{bulk} = 0.3$ m/s and (b) $u_{bulk} = 0.6$ m/s cases

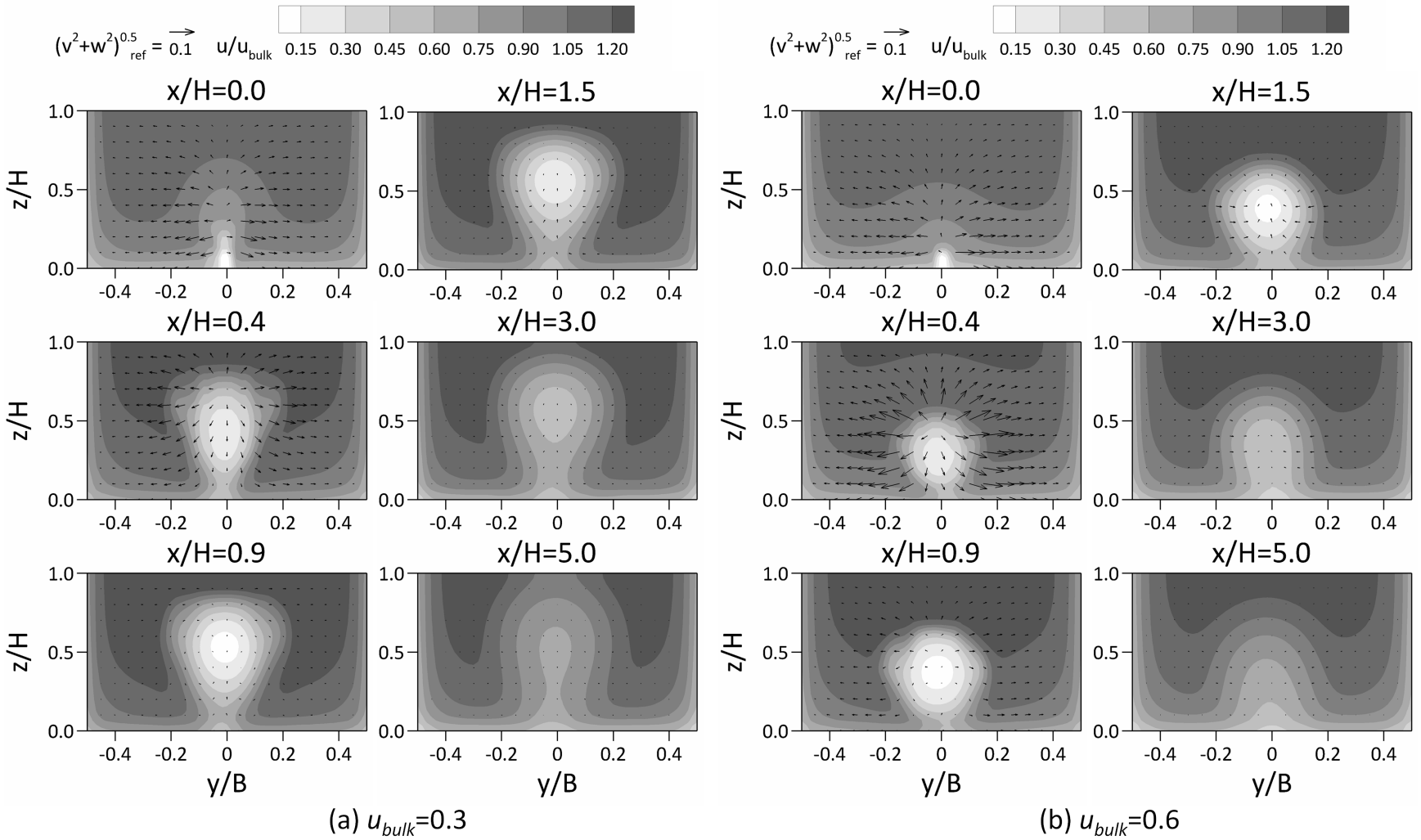

Figure 49: Distribution of time-averaged streamwise velocities and the vector of secondary currents on the selected cross-sections for the (a) $u_{bulk} = 0.3$ m/s and (b) $u_{bulk} = 0.6$ m/s cases

4.5 Conclusions

In the study, a new method that is based on a porosity approach is used to simulate flow through natural vegetation. The method is derived from the relationship between porosity and leave area index. In order to validate the method, data from laboratory experiments of flow through a submerged natural plant are used. The simulation results show that presence of the plant has a strong influence on the flow characteristics, especially in the center of channel where a deceleration of flow is clearly observed. The simulation performs fairly well in capturing the effect of porosity and bending. In addition, the qualitative ability of the porosity approach is assessed with the mean flow, turbulent structures, and secondary curruents. Overall, the study successfully shows the numerical modeling of the effect of real vegetation on the flow.

CHAPTER V

CONCLUSIONS AND DIRECTIONS FOR FUTURE RESEARCH

5.1 Conclusions

This thesis provides a better understanding of the hydrodynamics of flow through vegetation by employing high-resolution LES. Furthermore, new strategies were developed and validated to accurately and efficiently simulate turbulent flow through vegetation. The new methods were devised as alternatives to existing 3D numerical models such as RANS and LES, which have limitations in accuracy and efficiency, respectively, impeding the application of them in engineering practice.

In Chapter 2, flow structures and statistics in fully-vegetated channel flow were analyzed by employing high-resolution Large-Eddy Simulations to gain a full understanding of the vegetation-flow interaction. For a low vegetation density, experimental data with $\phi = 0.016$ at $Re_D = 1340$ was used to validate the high-resolution LES. The parameter range was extended with two more vegetation densities (i.e., $\phi = 0.063$ and 0.251) and three more cylinder Reynolds numbers (i.e., $Re_D = 125, 250$, and 500). In the validation, good agreement was found between measured and simulated data confirming the high accuracy of the LES method. In further simulations, it is confirmed that the vegetation density and cylinder Reynolds number are the most significant factors in determination of the mean flow, the turbulence statistics, flow resistance and instantaneous flow field. The extension of the simulation to varying vegetation density and very high cylinder Reynolds number is especially valuable in the study. At low vegetation density the flow behaves similar to the flow around an isolated cylinder, while there are significant structural differences at high cylinder density,

which is reflected in the turbulence statistics as well as in the flow resistance.

The specific conclusions of the high-resolution LES are as follows:

- The results from the high-resolution LES of flow through emergent vegetation and comparisons with measurements provided evidence of the high accuracy of LES and the suitability of the method to acquire a thorough physical understanding of the hydrodynamics of flow through vegetation.

- From the high-resolution LES data, normalized drag forces were obtained. The LES provided quantitative evidence that the drag coefficient, C_D decreases with increasing cylinder Reynolds number, Re_D, but increases with increasing vegetation density, ϕ. Moreover, the simulations confirmed the strong dependency of drag coefficient on vegetation density. Furthermore, the effect of Reynolds number disappears at low vegetation density, i.e., $\phi \leq 0.016$, and the flow behaves similar to the flow around an isolated cylinder with $C_D \approx 1$.

- From the detailed description of the instantaneous flow field that was provided by the high-resolution LES, it was found that vegetation density affects the mean flow and the turbulence. Increasing vegetation density leads to structural changes in the flow. Flow visualizations revealed that at low vegetation density ($\phi = 0.016$ and $\phi = 0.063$) regular von Karman vortex shedding occurs, while at high vegetation density ($\phi = 0.251$) shedding becomes irregular and vortices are less coherent. These changes were further quantified by turbulence statistics, velocity signal analysis, and the distributions of the drag and lift forces over time.

It was shown that high-resolution LES is one way of avoiding the C_D empiricism in numerical models of flow through vegetation by resolving the vegetation explicitly

through the numerical grid. However, even with the advantage of accuracy, the high-resolution LES remains a research tool that is limited to simple geometries due to its high computational cost.

In Chapter 3, two numerical strategies were introduced and evaluated for the flow through diverse arrays of cylinders; one is the RANS based model with a vegetation closure model, and another is a novel low-resolution LES. For the RANS based model, the importance of *a-priori* knowledge of drag coefficients was quantified. The low-resolution LES was developed in order to circumvent the dependency of numerical simulations of flow through vegetation on an empirical parameter. This is particularly attractive for more complex vegetation arrangements than the ones tested herein. Low-resolution LES has the prospect to compute vegetation drag for complex vegetation arrangements with considerably less computational effort than high-resolution LES and without empirical input. The method combines large eddy simulations with a first order immersed boundary method on relatively coarse Cartesian grids.

The most important findings in Chapter 3 are summarized below:

- The LES revealed that the bulk drag coefficient does not vary with the vegetation arrangement, i.e., staggered vs. random. At the same vegetation density ($\phi \approx 0.09$), the drag coefficients obtained from two sets of experiments, i.e., staggered and randomly-distributed cylinders, respectively, are equal.

- From numerical simulations using a RANS based model, it was found that the drag coefficient, an empirical parameter, is key to the accuracy of RANS simulations of flow through vegetation. Accurate predictions of flow resistance due to vegetation requires *a-priori* knowledge of drag coefficients in RANS models. If a wrong C_D is used, especially at high vegetation densities, flow resistance due to vegetation can be severely underestimated. For example, the

maximum error of flow resistance was found to be almost 78 % for the high vegetation density cases with $\phi = 0.251$ when C_D was simply estimated to have a value of 1.0.

- Low resolution LES is a good alternative to both high resolution LES and RANS due to the higher computational efficiency than the high-resolution LES and the higher accuracy than RANS. Validation of the low resolution LES showed that this approach is able to calculate quite accurately the drag coefficients for low and moderate vegetation densities (ϕ = 0.016, 0.022, 0.063, 0.087, 0.091, and 0.150). The method needs improvements for high vegetation densities (ϕ = 0.251).

Finally, in Chapter 4 a new strategy that is based on a porosity approach was devised as an alternative to the cylinder analogy to simulate flow through natural vegetation. Porosity values were determined from the leaf area index and the method was tested against laboratory experiments. This study is the first numerical simulation of flow through a natural plant that takes the physical properties of natural vegetation into account.

It is concluded that the porosity approach offers a more robust approach with the reason as follows:

- The new numerical strategy based on a porosity approach showed reasonable agreement in the comparisons of simulated velocities with experimentally acquired ones. The parameter of porosity was also yielded into a new parameter for the standard drag approach, and the prediction of the scheme also gave reasonable prediction for the mean flow around natural vegetation. In addition, the calculated bed shear stress through the plant provides a clue that the porosity approach is a novel method to predict flow resistance without *a-priori*

knowledge of drag coefficient.

- The porosity approach offered a more robust description of a strong effect of natural vegetation on the flow characteristics, especially showing a clear deceleration of flow in the center of channel. The visualization of the turbulent structures and secondary currents around and through the willow in the study showed the superior performance of the approach in capturing the effect of porosity and bending.

The main contributions of this study are:

i) Applied high-resolution LES to flow through emergent vegetation, resolved flow-vegetation interaction explicitly, and provided a better understanding of the turbulent flow characteristics

ii) Evaluated RANS modeling strategies and provided evidence of the importance of *a-priori* knowledge of C_D for RANS modeling

iii) Developed low-resolution LES approach for flow through vegetation which shows "higher efficiency than high resolution LES, higher accuracy than RANS"

iv) Developed and validated a new method porosity-based for RANS modeling of flow through natural vegetation

5.2 Directions for Future Research

Based on the findings in this thesis, further research is recommended in the following areas:

- **Water depth effect on flow through vegetation in shallow water.**

  This thesis investigated the flow through emergent vegetation in open channel flow, and therefore the characteristic length which represents the flow condition is the vegetation diameter, D. However, when the depth of flow becomes shallow, representative drag factors for the flow condition could be different. In shallow water, the contribution of bed friction on total drag and the turbulence structures may be affected by water depth more than by vegetation diameter. In particular, the percentage of bed friction on total drag should be reformulated as a function of water depth as well as vegetation density and cylinder Reynolds number. Moreover, it is obvious that the time-averaged streamwise velocity is not characterized as a constant over the vegetation height in shallow water anymore because of the role of the velocity bulge and bottom boundary layer. For example, the bottom boundary layer calculated in RANS for $10D$ case is $Z/D \approx 4$. Therefore, a relative water depth against vegetation diameter, h/D should be included into the main factors on vegetative effect in open-channel flow along with vegetation density and cylinder Reynolds number. Based on the already performed cases in the study, the shallowness effect would be assumed to occur in the range of $h/D < 10$. In addition, further simulations are needed to quantify the threshold.

- **Numerical study of flow through multiple natural plants and individual vegetation patch.**

  The study of flow through a natural plant in Chapter 4 should be extended to include cases with multiple plants. Numerical simulations of natural plants are particularly challenging because of the complexity of the shape of natural plants, which are difficult to parameterize for numerical models. The strategy to parameterize a natural plant as a porous medium should be achieved. The new strategy could play an active role in investigating turbulent flow through and around natural plants with leaves. Furthermore, in natural floodplains, vegetation is usually found in vegetation patches. The hydrodynamics of the flow inside the patch and between patches should be different from a uniform distribution of vegetation. The size and volume fraction of the patch become critical parameters as well as the diameter and density of individual plants. This needs further investigation.

- **Sediment transport and solute concentration in vegetated open-channels.**

  Sediment transport in flow through vegetation should be investigated, because vegetation plays an important role in sediment deposition in natural channels. Many numerical models have been used to determine the mean flow and turbulence structure of open-channels through and around vegetation to estimate sediment transport processes. However, the over-estimation of turbulent flow properties has been a significant issue of most models (see Section 3.1 and Table 3 for detailed information). Therefore, many numerical studies that investigated the effect of vegetation on sediment transport have been inconclusive. The three-dimensional numerical LES models developed in this thesis are expected to provide more accurate estimation of the shear stress and kinetic

energy. In addition, the LES models allow a detailed description of the instantaneous flow field, in particular the region behind cylinders and near bottom and further quantification of turbulence statistics. Hence, LES should be able to provide accurate predictions of flow-vegetation-sediment interactions, with which significant contributions can be made.

REFERENCES

[1] Bennett, S. J., Pirim, T., and Barkdoll, B. D., "Using simulated emergent vegetation to alter stream flow direction within a straight experimental channel," *Geomorphology*, vol. 44, no. 1-2, pp. 115–126, 2002.

[2] Choi, S. U. and Kang, H., "Reynolds stress modeling of vegetated open-channel flows," *Journal of Hydraulic Research*, vol. 42, no. 1, pp. 3–11, 2004.

[3] Cui, J. and Neary, V. S., "Large eddy simulation (LES) of fully developed flow through vegetation," in *Hydroinformatics 2002: Proceedings of the 5th International Conference on Hydroinformatics*, (Cardiff, U.K.), pp. 39–44, 2002.

[4] Defina, A. and Bixio, A. C., "Mean flow and turbulence in vegetated open channel flow," *Water Resources Research*, vol. 41, p. W07006, 2005.

[5] Dunn, C., Lopez, F., and Garcia, M. H., "Mean flow and turbulence in a laboratory channel with simulated vegatation," Tech. Rep. 51, University of Illinois at Urbana-Champaign, 1996.

[6] Engelund, F., "On the laminar and turbulent flows of ground water through homogeneous sand," *Transactions Danish Academy of Technical Sciences*, vol. 3, no. 4, p. 1, 1953.

[7] Fathi-Maghadam, M. and Kouwen, N., "Nonrigid, nonsubmerged, vegetative roughness on floodplains," *Journal of Hydraulic Engineering*, vol. 123, no. 1, pp. 51–57, 1997.

[8] Ferreira, R. M. L., Ricardo, A. M., and Franca, M. J., "Discussion of "Laboratory investigation of mean drag in a random array of rigid, emergent cylinders" by yukie tanino and heidi m. nepf," *Journal of Hydraulic Engineering*, vol. 135, no. 8, pp. 690–693, 2009.

[9] Fischer-Antze, T., Stoesser, T., Bates, P. B., and Olsen, N. R., "3D numerical modelling of open-channel flow with submerged vegetation," *Journal of Hydraulic Research*, vol. 39, no. 3, pp. 303–310, 2001.

[10] Germano, M., Piomelli, U., Moin, P., and Cabot, W. H., "A dynamic subgrid-scale eddy viscosity model," *Physics of Fluids A: Fluid Dynamics*, vol. 3, no. 7, pp. 1760–1765, 1991.

[11] Hanjalic, K. and Hadzic, I., "Third ERCOFTAC/IAHR workshop on refined flow modelling: turbulent flow and heat transfer in a subchannel of a staggered tube bundle," tech. rep., T. U. Delft, Delft, The Netherlands, 1998.

[12] Hunt, J. C. R., Wray, A. A., and Moin, P., "Eddies, streams, and convergence zones in turbulent flows," Tech. Rep. CTR-S88, Stanford University, Stanford, Calif, 1988.

[13] Ikeda, S., Ohta, K., and Hasegawa, H., "Instability-induced horizontal vortices in shallow open-channel flows with an inflection point in skewed velocity profile," *Journal of Hydroscience and Hydraulic Engineering Tech., Japan Society of Civil Engineers*, vol. 12, no. 2, pp. 69–84, 1994.

[14] Jaervelae, J., "Flow resistance of flexible and stiff vegetation: a flume study with natural plants," *Journal of Hydrology*, vol. 269, no. 1-2, pp. 44–54, 2002.

[15] Kevlahan, N. K. R., "Three-dimensional floquet stability analysis of the wake in cylinder arrays," *Journal of Fluid Mechanics*, vol. 592, pp. 79–88, 2007.

[16] Kim, S. J. and Stoesser, T., "Closure modeling and direct simulation of vegetation drag in flow through emergent vegetation," *Water Resources Research*, vol. 47, p. W10511, 2011.

[17] Kothyari, U. C., Hayashi, K., and Hashimoto, H., "Drag coefficient of unsubmerged rigid vegetation stems in open channel flows," *Journal of Hydraulic Research*, vol. 47, no. 6, pp. 691–699, 2009.

[18] Lam, K. and Lo, S. C., "A visualization study of cross-flow around four cylinders in a square configuration," *Journal of Fluids and Structures*, vol. 6, pp. 109–131, 1992.

[19] Lee, J. K., Roig, L. C., Jenter, H. L., and Visser, H. M., "Drag coefficients for modeling flow through emergent vegetation in the florida everglades," *Ecological Engineering*, vol. 22, no. 4-5, pp. 237–248, 2004.

[20] Liu, D., Diplas, P., Fairbanks, J. D., and Hodges, C. C., "An experimental study of flow through rigid vegetation," *Journal of Geophysical Research*, vol. 113, p. F04015, 2008.

[21] Liu, S. and Fu, S., "Regimes of vortex shedding from an in-line oscillating circular cylinder in the uniform flow," *Acta Mechanica Sinica*, vol. 19, no. 2, pp. 118–126, 2003.

[22] Lopez, F. and Garcia, M. H., "Mean flow and turbulence structure of open-channel flow through non-emergent vegetation," *Journal of Hydraulic Engineering*, vol. 127, no. 5, pp. 392–402, 2001.

[23] Luebcke, H., Schmidt, S., Rung, T., and Thiele, F., "Comparison of LES and RANS in bluff-body flows," *Journal of Wind Engineering and Industrial Aerodynamics*, vol. 89, pp. 1471–1485, 2001.

[24] Nadaoka, K. and Yagi, H., "Shallow-water turbulence modeling and horizontal large-eddy computation of river flow," *Journal of Hydraulic Engineering*, vol. 124, no. 5, pp. 493–500, 1998.

[25] Naot, D., Nezu, I., and Nakagawa, H., "Hydrodynamic behavior of partly vegetated open channels," *Journal of Hydraulic Engineering*, vol. 122, no. 11, pp. 625–633, 1996.

[26] Neary, V. S., "Numerical model for open-channel flow with vegetative resistance," in *IAHR's 4th International Conference on Hydroinformatics*, (Cedar Rapids, Iowa), pp. 23–27, July 2000.

[27] Neary, V. S., "Numerical solution of fully developed flow with vegetative resistance," *Journal of Engineering Mechanics*, vol. 129, no. 5, pp. 558–563, 2003.

[28] Nepf, H. M., "Drag, turbulence, and diffusion in flow through emergent vegetation," *Water Resources Research*, vol. 35, no. 2, pp. 479–489, 1999.

[29] Nicholas, A. P. and McLelland, S. J., "Computational fluid dynamics modelling of three-dimensional processes on natural river floodplains," *Journal of Hydraulic Research*, vol. 42, no. 2, pp. 131–143, 2004.

[30] Norberg, C., "Fluctuating lift on a circular cylinder: review and new measurements," *Journal of Fluids and Structures*, vol. 17, pp. 57–96, 2003.

[31] Olsen, N. R. B. and Stokseth, S., "Three-dimensional numerical modelling of water flow in a river with large bed roughness," *Journal of Hydraulic Research*, vol. 33, no. 4, pp. 571–581, 1995.

[32] Oplatka, M., *Stabilitt von Weidenverbauungen an Flussufern. Mitteilungen 156*. PhD thesis, Swiss Federal Institute of Technology, Zurich, 1998.

[33] Palau, G. P., Stoesser, T., Rummel, A., and Rodi, W., "Turbulent shallow flow through emergent vegetation," in *ICEH: International Conference on Ecohydraulics*, (Tempe, Arizona), 2007.

[34] Pasche, E. and Rouve, G., "Overbank flow with vegetatively roughened flood plains," *Journal of Hydraulic Engineering*, vol. 111, pp. 1262–1278, 1985.

[35] Patankar, S. V., *Numerical heat transfer and fluid flow*. New York: Hemisphere Pub, 1980.

[36] Petryk, S. and Bosmajian, G., "Analysis of flow through vegetation," *Journal of the Hydraulics Division*, vol. 101, no. 7, pp. 871–884, 1975.

[37] Pope, S. B., *Turbulent flows*. Cambridge, U.K.: Cambridge University Press, 2000.

[38] Press, W. H., Teukolsky, S. A., Vetterling, W. T., and Flannery, B. P., *Numerical Recipes in FORTRAN*. Cambridge, U.K.: Cambridge University Press, 1992.

[39] Rodi, W., *Turbulence models and their application in hydraulics: a state-of-the art review*. IAHR Monograph, Aa Balkema, 3rd ed ed., 1993.

[40] Rodi, W., "Comparison of LES and RANS calculations of the flow around bluff bodies," *Journal of Wind Engineering and Industrial Aerodynamics*, vol. 69-71, pp. 55–75, 1997.

[41] Rogallo, R. S. and Moin, P., "Numerical simulation of turbulent flows," *Annual Review of Fluid Mechanics*, vol. 16, pp. 99–137, 1984.

[42] Rollet-Miet, P., Laurence, D., and Ferziger, J., "LES and RANS of turbulent flow in tube bundles," *International journal of heat and fluid flow*, vol. 20, no. 3, pp. 241–254, 1999.

[43] Ross, J. and Ross, V., "Statistical description of the architecture of a fast growing willow coppice," *Agricultural and Forest Meteorology*, vol. 91, no. 1-2, pp. 23–37, 1998.

[44] Schlicting, H., *Boundary layer theory*. New York: McGraw-Hill, 4th ed ed., 1962.

[45] Schneider, S., *Widerstandsverhalten von holzigen Auenpflanzen: Konzept zur Etablierung von Weichholzauen an Fliegewssern*. PhD thesis, University of Karlsruhe, Karlsruhe, Germany, 2010.

[46] Shimizu, Y. and Tsujimoto, T., "Numerical analysis of turbulent open-channel flow over a vegetation layer using a k-ϵ turbulence model," *Journal of Hydroscience and Hydraulic Engineering*, vol. 11, no. 2, pp. 57–67, 1994.

[47] Smagorinsky, J., "General circulation experiments with the primitive equations," *Monthly Weather Review*, vol. 91, no. 3, pp. 99–164, 1963.

[48] Stoesser, T., *Development and validation of a CFD code for open-channel flows*. PhD thesis, Department of Civil Engineering, University of Bristol, Bristol, U.K., 2002.

[49] Stoesser, T., "Physically realistic roughness closure scheme to simulate turbulent channel flow over rough beds within the framework of LES," *Journal of Hydraulic Engineering*, vol. 136, no. 10, pp. 812–819, 2010.

[50] Stoesser, T., Kim, S. J., and Diplas, P., "Turbulent flow through idealized emergent vegetation," *Journal of Hydraulic Engineering*, vol. 136, no. 12, pp. 1003–1017, 2010.

[51] Stoesser, T., Liang, C., Rodi, W., and Jirka, G. H., "Large eddy simulation of fully-developed turbulent flow through submerged vegetation," in *River Flow*, 2006.

[52] Stoesser, T. and Nikora, V., "Flow structure over square bars at intermediate submergence: Large eddy simulation study of bar spacing effect," *Acta Geophysica*, vol. 56, no. 3, pp. 876–893, 2008.

[53] Stoesser, T., Palau-Salvador, G., Rodi, W., and Diplas, P., "Large eddy simulation of turbulent flow through submerged vegetation," *Transport in Porous Media*, vol. 78, no. 3, pp. 347–365, 2009.

[54] Stoesser, T., Wilson, C. A. M. E., Bates, P. D., and Dittrich, A., "Application of a 3D numerical model to a river with vegetated floodplains," *Journal of Hydroinformatics*, vol. 5, no. 2, pp. 99–112, 2003.

[55] Stone, B. M. and Shen, H. T., "Hydraulic resistance of flow in channels with cylindrical roughness," *Journal of Hydraulic Engineering*, vol. 128, no. 5, pp. 500–506, 2002.

[56] Stone, H. L., "Iterative solution of implicit approximations of multidimensional partial differential equations," *SIAM Journal on Numerical Analysis*, vol. 5, no. 3, pp. 530–558, 1968.

[57] Takemura, T. and Tanaka, N., "Flow structures and drag characteristics of a colony-type emergent roughness model mounted on a flat plate in uniform flow," *Fluid Dynamics Research*, vol. 39, no. 9-10, pp. 694–710, 2007.

[58] Tanino, Y. and Nepf, H. M., "Laboratory investigation of mean drag in a random array of rigid, emergent cylinders," *Journal of Hydraulic Engineering*, vol. 134, no. 1, p. 34, 2008.

[59] Tsihrintzis, V. A., "Discussion of wu et al., 1999," *Journal of Hydraulic Engineering*, vol. 127, no. 3, pp. 241–244, 2001.

[60] Tsujimoto, T. and Kitamura, T., "Velocity profile of flow in vegetated-bed channels," tech. rep., Kanazawa University, Kanazawa, Japan, 1990.

[61] Tsujimoto, T. and Kitamura, T., "Experimental study on open-channel flow with vegetated zone along side wall," Tech. Rep. 3, Kanazawa University, Kanazawa, Japan, 1992.

[62] Tsujimoto, T. and Shimizu, Y., "Flow and suspended sediment in a compound channel with vegetation," in *1st International Symposium on Habitat Hydraulics*, (Trontheim, Norway), pp. 357–370, 1994.

[63] Umeda, S. and Yang, W. J., "Interaction of von karman vortices and intersecting main streams in staggered tube bundles," *Experiments in Fluids*, vol. 26, no. 5, pp. 389–396, 1999.

[64] White, F. M., *Viscous fluid flow*. New York: McGraw-Hill, 2nd ed ed., 1991.

[65] Wilson, C., Stoesser, T., Bates, P. D., and Batemann Pinzen, A., "Open channel flow through different forms of submerged flexible vegetation," *Journal of Hydraulic Engineering*, vol. 129, pp. 847–853, 2003.

[66] Wu, F. C., Shen, H. W., and Chou, Y. J., "Variation of roughness coefficients for unsubmerged and submerged vegetation," *Journal of Hydraulic Engineering*, vol. 125, no. 9, pp. 934–942, 1999.

[67] Wu, W., Shields Jr, F. D., Bennett, S. J., and Wang, S. S. Y., "A depth-averaged two-dimensional model for flow, sediment transport, and bed topography in curved channels with riparian vegetation," *Water Resources Research*, vol. 41, p. W03015, 2005.

[68] Yagci, O. and Kabdasli, M. S., "The impact of single natural vegetation elements on flow characteristics," *Hydrological Processes*, vol. 22, pp. 4310–4321, 2008.

[69] Zhang, J. F. and Dalton, C., "Interaction of a steady approach flow and a circular cylinder undergoing forced oscillation," *Journal of fluids engineering*, vol. 119, pp. 802–813, 1997.

VITA

Su Jin Kim was born in Seoul, Republic of Korea on August 23rd, 1981. She received a Bachelor of Science in Civil Engineering from Hanyang University, Seoul, Korea in 2005. After she received a Master of Science in Civil Engineering in 2007 in the same university, she started her doctorate research at Georgia Institute of Technology. At Georgia Tech, she joined the Computational Fluid Dynamics group of Dr. Thorsten Stoesser and completed her Ph.D. degree in December 2011.